Measurement of the Astrophysical Factor S_{17} by the Coulomb Break-up of ^{8}B at 254 MeV/u

Grzegorz Surówka

Dissertation presented to the
Faculty of Mathematics and Physics
of the Jagiellonian University
for the degree of Doctor of Physics

Dissertation supervisor:
Professor Reinhard Kulessa

Kraków, October 2000

Measurement of the Astrophysical Factor S_{17} by the Coulomb Break-up of ^{8}B at 254 MeV/u

Grzegorz Surówka

Abstract

Differential cross section for the Coulomb break-up of ^{8}B into ^{7}Be and proton has been measured. With this reaction the astrophysical factor S_{17} for the production of ^{8}B – the source of high-energy solar neutrinos is determined. The electrodynamical break-up of ^{8}B at 254 MeV/u has been found to be a pure continuum dipole transition. The deduced S_{17}-factor yields $S_{17}(0) = (20.0 \pm 1.3)\,\mathrm{eV \cdot b}$ This result agrees with the extrapolations done in some direct-capture experiments and in the Coulomb-break-up study at 50 MeV/u.

Dissertation presented to the
Faculty of Mathematics and Physics
of the Jagiellonian University
for the degree of Doctor of Physics

Kraków, October 2000

Acknowledgments

I would like to thank my supervisor Professor Reinhard Kulessa and Professor Eckart Grosse for giving me the opportunity to work in the heavy-ion laboratory GSI in Darmstadt. I appreciate very much I could deal with this interesting subject that was in line with my astrophysical roots.

I want to thank Dr Peter Senger and Dr Klaus Sümmerer for their friendly help and support. I benefited greatly by their knowledge and experience.

From Dr Naohito Iwasa I learned most of the things. He introduced me in the experiment and gave me the necessary know-how. To him I owe bases of my simulation knowledge. I appreciate very much the assistance I got from Florian Uhlig. He was always willing to investigate the Geant engine. With Frédéric Boué who analyzed the data as well I had many fruitful discussions.

I am fully indebted to Dr Alicja Surowiec for her work with the online analysis and to Dr Piotr Koczoń for the data acquisition and electronics. I recall also nice lunch times and interesting talks.

It was a fruitful experience to work in the KaoS collaboration group with Andreas Förster, Prof. Berndt Kohlmeyer, Dr Frank Laue, Prof. Helmut Oeschler, Erwin Schwab, Dr Yang-Hwan Shin, Dr Jürgen Speer, Christian Sturm and Dr Andreas Wagner.

I am grateful to my colleagues at the Jagiellonian University: Dr Mariusz Dębowski, Dr Edward Lubkiewicz, Jacek Otwinowski, Dr Piotr Salabura, Dr Eugeniusz Wajda, and Professor Władysław Waluś and Professor Andrzej Bałanda for a friendly approach they gave me. I owe a fresh look at some crucial existential questions to Eng. Wawrzyniec Prokopowicz.

With my friends: Witold Przygoda and Leszek Kidoń I could always discuss all aspects of life.

I am very grateful to my parents Lucyna and Zenon† Surówka for giving me their love and support. All my education and this graduation I owe to them. It is to my parents I dedicate this work.

Above all I would like to express my deep fascination of the Act of Creation. I can hardly comprehend the harmony and beauty of Nature I admire.

Contents

List of Figures

List of Tables

Chapter 1

Physical problem

Since it became clear that the fusion of light nuclei into heavier elements is the source of the energy radiated from the main sequence stars, nucleosynthesis has begun to play a key role in understanding stellar evolution. Moreover, an explanation of the origin and abundances of elements in the Universe is an important consequence of this hypothesis (see e.g. [Arn90, Fow84]).
Our nearest star, the Sun, gives us an opportunity to study the concept of nuclear energy generation. Among all the particles involved in the nucleosynthesis, the liberated neutrinos are the only direct probe of the solar interior. Due to their property to interact with matter only in weak processes, neutrinos can leave the solar interior unscattered thus currying information about the respective thermonuclear reaction rates. It seems now that by investigating solar neutrinos we face a manifestation of new physics.

Here I give a compact introduction to what has been called for almost thirty years the 'solar neutrino problem'. Then I formulate a motivation which became basis of my work and this thesis. The next chapter gives mathematical tools necessary to describe the physics my research deals with. Then I introduce an experiment of the Coulomb dissociation of ^{8}B and my analysis leading to obtain the differential cross-section for the electrodynamical break-up of ^{8}B. This experiment allows me to measure the astrophysical factor S_{17} in an alternative way. In the last chapter I discuss an extrapolation method to obtain the S-factor at zero energy. Finally, I draw conclusions and give an outlook.

1.1 Introduction

Energy generation through thermonuclear reactions appears to be very successful in explaining the luminosity of the Sun. 98% of the solar energy is produced in a chain of reactions through which four protons are converted to one helium nucleus. This is called the pp-cycle and is shown in Fig. 1.1. There are four

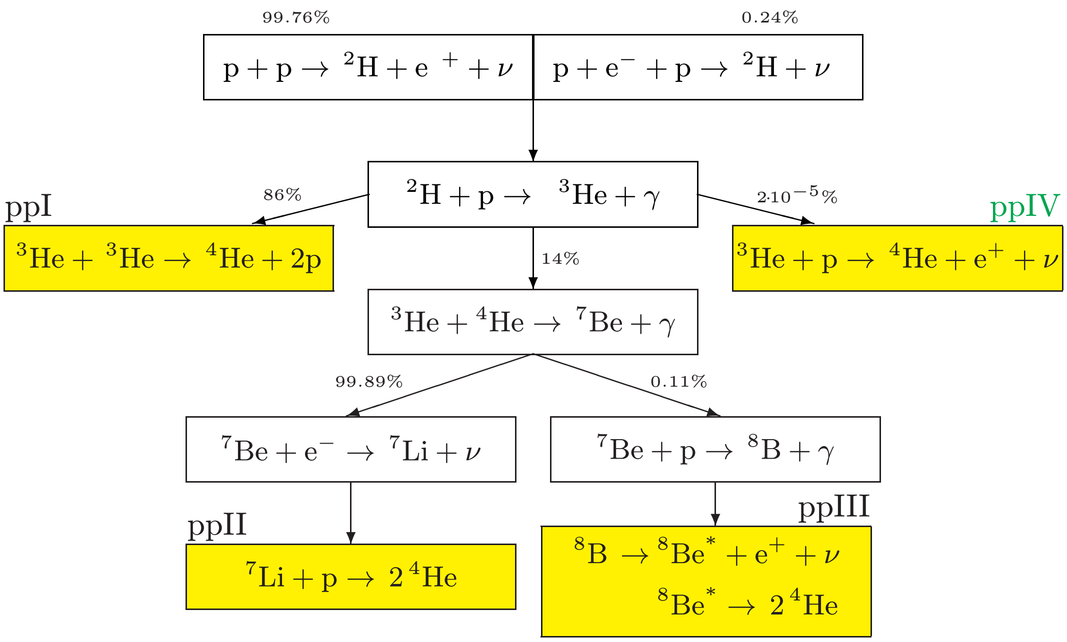

Figure 1.1: *pp-chain in the Sun. The numbers show relative contributions of the branches [Hax95].*

paths contributing to the helium production, ppI-ppIV. The majority of all cases proceeds through fusion of two protons resulting in a deuteron and a neutrino. Through an intermediate step producing ^{3}He, the ppI branch terminates with a ^{3}He-^{3}He reaction (86%). The remaining part goes through the channel ^{3}He-^{4}He and terminates either as ^{7}Li-p (ppII - 14%) or as the decay of an excited ^{8}Be from ^{8}B β-decay (ppIII - 0.1%). The last branching occurs due to an electron or possibly a proton capture of ^{7}Be.
All the four pp-branches have the same summary form, namely

$$4p \to {}^4He + 2\,e^+ + 2\,\nu_e \tag{1.1}$$

and, depending on the respective branch, release an average energy amount of about 26 MeV. Helium can be also synthesized in the CNO-cycle. However, in case of the Sun whose central temperature, 1.5×10^7K, is relatively low, CNO participates by not more than 2% in the whole energy production [Hax95, Ade98]. To the same extent it influences the flux of solar neutrinos.

In Fig. 1.2 energy spectra of the neutrinos coming from all the thermonuclear reactions and β-decays in the Sun are shown. The main process of the pp-cycle produces a continuous spectrum of low-energy neutrinos from $p + p \to {}^2H + e^+ + \nu$ and, 2-3 orders of magnitude lower in intensity, a discrete neutrino line at 1.44 MeV from $p + e^- + p \to {}^2H + \nu$. The electron capture $^7Be + e^-$

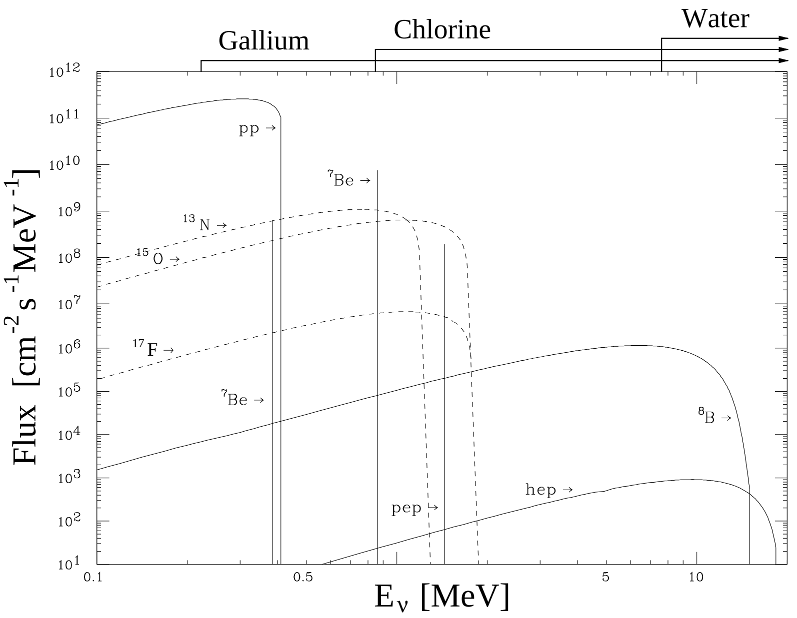

Figure 1.2: *Energy spectra of the solar neutrinos in a standard model of the Sun [Bah95] (discrete lines are in [cm^{-2}s^{-1}]). The thresholds of the solar neutrino detectors are shown at the top.*

produces mono-energetic neutrinos of 0.86 MeV (90%) and 0.38 MeV (10%) corresponding to feeding the ground and the first excited state in ^{7}Li. The three-body decay of ^{8}B produces neutrinos of the highest energy (^{3}He + p neutrinos are negligible). The CNO-cycle is the source of β-decay neutrinos coming from ^{13}N, ^{15}O, and ^{17}F. All the neutrino-emitting reactions are summarized in Table 1.1.

source	E_ν [MeV]	integrated Flux [cm^{-2} s^{-1}]
$\mathbf{p + p \rightarrow {}^2H + e^+ + \nu}$	≤ 0.42	$5.94 \cdot 10^{10}$
$\mathrm{p + e^- + p \rightarrow {}^2H + \nu}$	1.44	$1.39 \cdot 10^{8}$
$\mathrm{{}^3He + p \rightarrow {}^4He + e^+ + \nu}$	18.77	$2.10 \cdot 10^3$
$\mathbf{{}^7Be + e^- \rightarrow {}^7Li + \nu}$	0.86 (90%)	$4.80 \cdot 10^9$
	0.38 (10%)	
$\mathbf{{}^8B \rightarrow {}^8Be + e^+ + \nu}$	≤ 14.06	$5.15 \cdot 10^6$
$\mathrm{{}^{13}N \rightarrow {}^{13}C + e^+ + \nu}$	≤ 1.20	$6.05 \cdot 10^8$
$\mathrm{{}^{15}O \rightarrow {}^{15}N + e^+ + \nu}$	≤ 1.73	$5.32 \cdot 10^8$
$\mathrm{{}^{17}F \rightarrow {}^{17}F + e^+ + \nu}$	≤ 1.74	$6.33 \cdot 10^6$

Table 1.1: *Sources of solar neutrinos, both from pp (upper part), and from the CNO-cycle (bottom) [Bah98a].*

What we can see in Fig. 1.2 are the predictions of one solar model ([Bah98a]). A solar model is a set of four state quantities: opacity κ, nuclear energy generation ϵ_{nucl}, adiabatic exponent γ, and mean molecular weight μ, all being functions of density, temperature and hydrogen X, helium Y, and metallicity composition Z. They describe the physics of the star and are input parameters to solve five equations for five unknown variables: temperature, luminosity, radius, pressure, and density. The most convenient way to investigate the above-mentioned observables is to choose mass as an independent variable. It is rather easy to find all conditions (i.e. equations) at which a ball of ionized gas, radiating energy, remains in hydrodynamical equilibrium (see e.g. [Rol88, Cla83]). A crucial point is that any solar model must reproduce all astronomical observables which constrain the input parameters. In case of the Sun, the following observables have been measured very precisely: its luminosity i.e. energy flux at the surface of the Earth ($L_{\odot} = (3.846 \pm 0.004) \cdot 10^{33}$ erg s^{-1}), the surface temperature resulting in the solar spectral properties ($T_{\odot}$=5770 K), the radius ($R_{\odot} = (6.9599 \pm 0.0002) \cdot 10^{10}$ cm), and the mass ($M_{\odot} = (1.9891 \pm 0.0004) \cdot 10^{33}$ g) [Bru98]. Solar models of any kind must satisfy these constraints.

Several models have been developed and been improving continuously their inputs. A main group of them are standard solar models (SSM): the one by Bahcall and Ulrich [Bah88] and its updates [Bah92, Bah95, Bah98a], the SSM by Turck-Chièze and coworkers [Tur88, Tur93, Bru98], by Dar and Shaviv [Dar96a], and two others [Sie90, Sac90]. They use the favored, best known values of nuclear input parameters [Ade98] and treat the solar structure in a classic, stellar-evolution evident way. SSM obey also principles of the standard electroweak theory treating neutrinos as massless particles whose flavor is conserved. Even the best known and widely referenced SSM ([Bah98a, Tur93, Dar96a]) predict different solar neutrino fluxes. It is not the case for the p + p-reaction neutrinos which are known very precisely (to 1%) for the solar-luminosity constraint, yet the ^{7}Be and ^{8}B-neutrino fluxes can vary to about 10% among the models. It is due to the fact that, though these SSM reproduce well all the observed features of the Sun, still two degrees of freedom are present – physics of the convecting zone, and the initial helium abundance. This and uncertainties of the nuclear inputs (mainly cross-section of $^7\mathrm{Be}(\mathrm{p}, \gamma)^8\mathrm{B}$) are the reasons of the discrepancies. Since the thermonuclear reactions are sources of neutrinos, the neutrino energy distribution and their flux observed on the Earth could give a feedback improving solar models.

1.1.1 Measurements of solar neutrino fluxes

Thirty years ago, in 1967, a terrestrial measurement of solar neutrino fluxes was proposed [Dav68]. It was originally argued that such a measurement could provide a unique information about the physical conditions and the nuclear reaction chains taking place in the core of the Sun. Due to their properties of massless particles, interacting in weak processes, neutrinos were supposed to keep a precise record of the solar interior. Soon it was realized that these investigations could provide also information about the intrinsic properties of neutrinos. In the following the running solar-neutrino detectors are introduced and it is described how the solar neutrino problem turned up.

Experiments to detect solar neutrinos are very difficult. Very low cross-sections of neutrino interaction together with low fluxes demand large detectors. Energies of the neutrino spectrum of the order of a few MeV are in the range of natural and cosmic-ray-induced activities so elimination of background is needed. Three types of detectors observe solar neutrinos. Homestake and GALLEX/SAGE are radiochemical experiments where solar neutrinos induce activity in a large mass of target material. These experiments measure time-integrated neutrino fluxes. On the contrary, KAMIOKANDE is a real-time experiment, where neutrinos are detected 'on-line', without any exposure time needed (a review on operating and next-generation detectors can be found in [Bah89a]).

- Homestake (chlorine)
  Neutrinos are detected in a reaction $\nu_e + {}^{37}\mathrm{Cl} \rightarrow e^- + {}^{37}\mathrm{Ar}$. A radioactive ${}^{37}\mathrm{Ar}$ decays back to ${}^{37}\mathrm{Cl}$ with $T_{1/2} = 35$d by K-electron capture (probability 90%). Auger electrons which are then emitted ($E^{total} = 2.8$ keV) make the detection possible [Dav68]. The threshold energy is 814 keV and the experiment is sensitive to ${}^{7}\mathrm{Be}$ and ${}^{8}\mathrm{B}$ neutrinos (the latter contribute by about 75%). The detector consists of a tank with 615 tons of liquid perchloroethylene C_2Cl_4 [Dav94] and is located in the Homestake Gold Mine in Lead, South Dakota, USA, at a depth of 1400 m below ground. It has been operating since 1968. The observed reaction rate [Cle98]: 2.56±0.23 SNU (SNU - Solar Neutrino Unit=10^{-36} captures/1 sec/1 target atom).

- GALLEX/SAGE (gallium)
  Principally the same method is used by the GALLium EXperiment in Gran Sasso, Italy. ${}^{71}\mathrm{Ge}$ produced by $\nu_e + {}^{71}\mathrm{Ga} \rightarrow e^- + {}^{71}\mathrm{Ge}$ decays ($T_{1/2} = 11.4$d) by electron capture knocking out Auger electrons from the K-shell (10.4 keV) and L-shell (1.2 keV) [Ham96]. A relatively low threshold energy, 233 keV, makes it possible to measure p+p neutrinos which are expected to contribute by 56% to the total rate. The experiment is performed at a depth corresponding to 3500 m of water equivalent (mwe). The target is 30.3 tons of $GaCl_3$ in an aqueous solution of HCl. The observed reaction

rate [Cri99]: 76.4±8 SNU.
SAGE, the Russian-American Gallium solar neutrino Experiment , uses 55 tons of metallic ^{71}Ga [Abd94]. The Baksan Neutrino Observatory is an underground laboratory at a depth of 4700 mwe. The observed reaction rate, 74±12 SNU, is an update of [Abd96].
Both GALLEX ([Ber96b] and references therein) and SAGE [Ell96a] take into account efficiency of the gallium detector measured with a ^{51}Cr neutrino source.

- KAMIOKANDE II/III (water)
  The KAMIOKA Nucleon Decay Experiment in Japan was originally built to search for proton decays. It is a 3-kiloton water Cherenkov detector (1000 m underground) to detect light emitted by the recoil electrons $\nu + \mathrm{e} \rightarrow \nu + \mathrm{e}$ in water [Hir91, Tot96]. This scattering reaction is sensitive to neutrinos of any flavor, though electron neutrinos dominate ($\sigma(\nu_{\mathrm{e}})/\sigma(\nu_{\mu}) \sim 7$). A big effort to reduce the radon contamination in the water succeeded in setting the electron energy threshold at about 7.5 MeV. The experiment is sensitive solely to the ^{8}B solar neutrinos, and additionally to atmospheric neutrinos of sub-GeV energies (atmospheric neutrinos are products of hadronic jets induced by cosmic rays in the atmosphere at an altitude of the order of 10 km). By recording neutrinos arrival times it is possible to correlate them with the position of the Sun (the 'day-night' effect).
  KAMIOKANDE provides also the energy spectrum of the incident solar neutrinos for it measures the energies of the individual scattered electrons. The observed solar neutrino flux (II/III combined) [Fuk96] of $2.80 \pm 0.19^{\mathrm{stat}} \pm 0.33^{\mathrm{syst}}\, 10^{6}\mathrm{cm}^{-2}\mathrm{s}^{-1}$ assumes pure ν_{e} from undistorted ^{8}B β-decay.
  SUPER-KAMIOKANDE is a 50-kiloton water detector located near its predecessor in the same Mozumi mine [Ino99]. It is a newly designed and improved version of KAMIOKANDE with an energy threshold of about 6.5 MeV. The observed neutrino flux amounts to $2.42 \pm 0.06^{\mathrm{stat}}\ {}^{+0.10}_{-0.07}{}^{\mathrm{syst}}$ $10^{6}\mathrm{cm}^{-2}\mathrm{s}^{-1}$ [Fuk98] with the same assumptions as above.

1.1.2 Solar neutrino problems

Comparing the (SUPER-)KAMIOKANDE results to those listed in Table 1.1 convinces us directly that these detectors measure fewer neutrinos than predicted in SSM. To analyze the radiochemical experiments, which measure the product of a neutrino flux times a neutrino-capture cross-section, a recalculation of the model predictions to the respective experimental rates in SNU is needed. All results of the neutrino flux measurements are gathered in Fig. 1.3 for a comparison with the theoretical calculations of [Bah98a]. We conclude that discrepancies exist between the measured and expected rates of the solar neutrino fluxes (from 27% to 60% roughly). A thorough look reveals more serious difficulties. The three solar neutrino problems (SNP) are summarized below ([Bah96]):

1. Discrepancy in calculated *vs.* observed absolute rate.
   This problem was first defined in the chlorine experiment as a factor of three deficit of the measured solar neutrinos compared to SSM. Approximately a factor of two less neutrinos were found in KAMIOKANDE. This problem was attributed to deficiencies of SSM and/or an incorrect neutrino capture cross-section in ^{37}Cl.

2. Cl – H_2O incompatibility.
   Solar physics does not change the shape of the ^{8}B-neutrino energy spectrum so, by assuming it is not changed by new neutrino physics, it is possible to calculate the rate in the chlorine experiment which is produced solely ($E_{\mathrm{threshold}} > 7.5$ MeV) by the ^{8}B neutrinos observed in KAMIOKANDE

$$\begin{array}{lcccrl} H_2O(\nu_{^8B}) & \xrightarrow{\text{calc.}} & Cl(\nu_{^8B}) & = & 3.20\pm0.45 & \text{SNU} \\ & & Cl^{\mathrm{exp}} & = & 2.56\pm0.25 & \text{SNU} \\ \hline & & & & -0.66\pm0.52 & \text{SNU} \end{array}$$

   → The ^{8}B neutrinos alone detected in KAMIOKANDE exceed the total measured rate in the chlorine experiment, $\Phi_{\mathrm{Cl}}(^7\mathrm{Be} + {}^8\mathrm{B}) < \Phi_{\mathrm{H_2O}}(^8\mathrm{B})$.
   → Nothing remains for the p+e+p, ^{7}Be, and CNO neutrinos (predicted total yield: 1.9 SNU).

3. No room for the ^{7}Be, ^{8}B neutrinos in GALLEX/SAGE.
   This is an independent problem since the p+p neutrinos are not observed in the other experiments. The p+p neutrino flux is approximately model-independent and is known to 1% from the solar luminosity. Results of both experiments practically exhaust the p+p and p+e+p theoretical prediction

ν	observed	predicted
pp,pep	70.5±7	72.4 SNU
^{8}B	7	12.4 SNU
^{7}Be		34.4 SNU

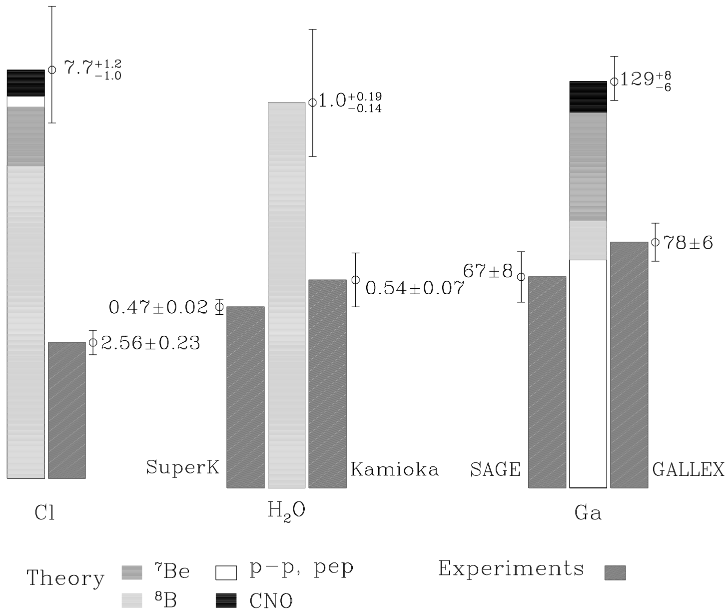

Figure 1.3: *Measured and predicted solar neutrino fluxes in the chlorine, water and gallium detectors according to [Bah96] (revised in [Bah98a]). The radio-chemical experiments are presented in SNU while the result for KAMIOKANDE is given as the ratio of the observed and theoretical fluxes, the latter normalized to unity.*

> Everything but p+p neutrinos are excluded. The gallium detector leaves no room for the ^{7}Be or ^{8}B neutrinos whose signals, on the other hand, are present in the Homestake and KAMIOKANDE experiments.

Let us recall which assumptions underlie the solar neutrino problems:

1. The accuracy of the solar neutrino experiments is not overestimated; no unknown systematic errors enter the measurements.

2. Standard solar models provide a sufficiently accurate description of the solar interior and the neutrino-producing reactions.

3. Neutrino properties do not go beyond the standard electro-weak theory (massless, flavor-conserved particles).

Dar and Shaviv [Dar96b] investigated solutions for which these assumptions are not fulfilled and termed them as terrestrial, astrophysical, and new particle-physics solutions, respectively.

1) Measurements of the solar neutrino fluxes were subject to careful investigations (see [Cas97, Cas94] and all references to the solar-neutrino experiments in this section). In 1995 the GALLEX chromium-source experiment was performed. Anselmann and coworkers [Ans95] exposed the gallium detector to a known 746 keV neutrino flux from a ^{51}Cr source. Its known activity provided an overall check of GALLEX. The authors have concluded that there are no significant experimental artifacts or unknown errors which could cause the 40% deficit in the observed solar neutrino signal. In addition, due to close similarity in neutrino-energy spectra from ^{51}Cr and the solar ^{7}Be, they have demonstrated that the gallium detector is sensitive to the ^{7}Be neutrinos without any reduction in efficiency. The same conclusions have been drawn in SAGE [Ell96a]. The chromium source experiment has greatly reduced chances of any terrestrial solutions to be responsible for the solar neutrino problem.

2) For an astrophysical solution of the solar neutrino problems SSM were investigated. Some authors (e.g. [Dar96b]) pointed out that SSM provide only an approximate description of the real Sun. They have found that the knowledge of dense-plasma effects, nuclear reaction rates, and energy transport in the Sun,

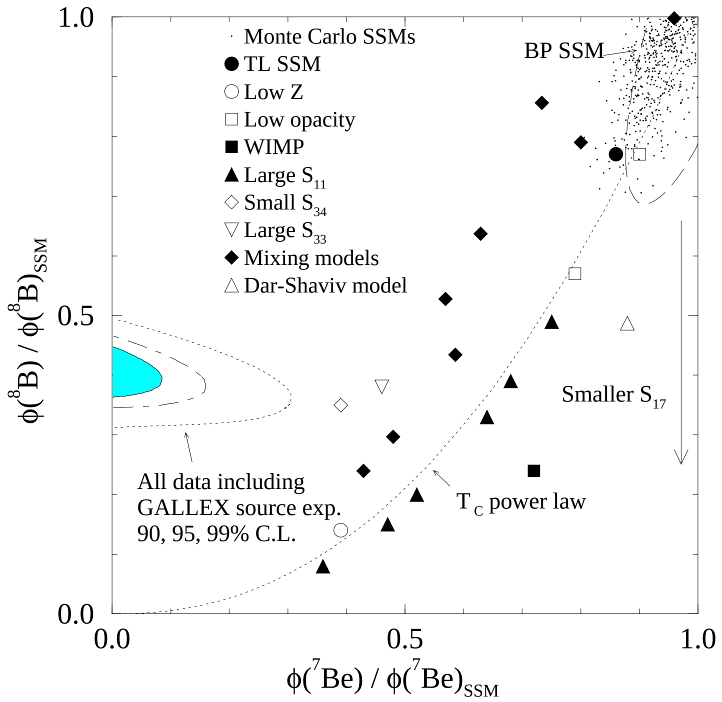

Figure 1.4: *^{8}B solar-neutrino flux as a function of that of ^{7}Be (both quantities are given relative to the SSM predictions [Bah98a]). Various solar models are shown and data for the ^{37}Cl, KAMIOKANDE II/III, GALLEX/SAGE and the GALLEX chromium-source experiments [Hat95].*

was insufficient to draw conclusions about the observed solar neutrino flux.
On the contrary, systematic helioseismic investigations cast a new light on the solar structure and are supposed to test SSM more efficiently than the solar neutrinos. The most important helioseismic observables are frequencies of acoustic solar oscillations [Chr96]. They are measured with instruments both on the Earth and on the SOHO satellite (for references see [Cas99]). It is also possible to determine the depth of the solar convective zone and the present-day surface abundance of helium. Results of five precise helioseismic measurements are compared with the newest SSM of Bahcall in [Bah98a]. The excellent agreement between the calculated and measured speeds of sound for $R/R_\odot = 0.05 \div 0.95$ is far under a 'safe' discrepancy level which still does not influence in a visible way the solar neutrino flux. One notes, however, the criticism presented in [Tur96] about experimental deficiencies in penetrating the most inner part of the Sun ($R/R_\odot < 0.3$). It was argued that the effects of the sound speed in the very center have negligible influence on the observed features of the Sun, they may influence, however, the neutrino predictions. It is clear that further investigations in this field are needed. Nowadays helioseismology seems to prove its usefulness and confirms in a satisfactory way all predictions of SSM by Bahcall *et al.* [Bah98a].
Under this assumption, to still find an astrophysical solution, modifications of SSM were investigated. Bahcall and Ulrich [Bah89b] simulated Monte Carlo solar models by randomly varying all input parameters within their quoted error bars. Hata and Haxton [Hat95, Hax96] have presented these results plus all non-standard solar models (assuming modifications in the solar structure, see a review by Castellani *et al.* [Cas97]) compared with the experimental data. It is shown in Fig. 1.4 as the ^{7}Be *vs.* ^{8}B-neutrino fluxes normalized to the SSM predictions of Bahcall (right upper corner). The combined results of the solar neutrino experiments have allowed the authors to draw only one conclusion: neither standard nor non-standard solar models can solve the solar neutrino problem.
A further analysis was done by Berezinsky and coworkers [Ber96a]. They treated the astrophysical factors (i.e. cross-sections) for the solar reactions, as free parameters within standard astrophysical scaling laws. The values they have found, though very restrictive and highly improbable, can save only two of the three solar neutrino experiments. They have called it 'no hope' for an astrophysical solution of SNP.

3) Since no solar model can explain the solar neutrino experiments, some particle-physics explanations are being investigated. In fact solutions of this kind may have important implications on other not yet solved problems in astrophysics like e.g. quest for the dark matter [Ell96b], or the anomaly of atmospheric neutrinos (see SUPER-KAMIOKANDE measurements [Fuk98]). A most favored assumption suited to solve a broad spectrum of problems is that the neutrino has a mass.

In the standard electroweak theory there are three lepton families plus their corresponding antiparticles. The three kinds of neutrino flavors (electron, muon, tau) are all massless and cannot interfere with each other. If, however, no degeneracy in neutrino-mass eigenstates exists, the neutrino flavors observed in weak interactions are superpositions of these mass eigenstates, or we say, they oscillate. These oscillations are neutrino-energy dependent and are described with some parameters: the mass differences of the neutrino flavors, and the mixing angles (for a simplification sometimes only two neutrino types, ν_{e}, ν_{μ}, are considered). Propagating neutrinos of a given flavor change their intensities since a given mixture varies in time. The composition of a neutrino flux is thus a function of time and distance from the source. Due to this model of vacuum oscillations [Smi99], electron neutrinos produced in the thermonuclear reactions in the Sun could reach the Earth partially as muon or tau-flavor ones. Since the radiochemical experiments (the only ones for the p+p, ^{7}Be neutrinos) are not sensitive to these signals, a part of the flux is not detected and an apparent neutrino deficit is observed. The length of the oscillation path between the Sun and the Earth, about 10^{8} km, should result in a very small mass difference of the order of $\Delta \mathrm{m}^2 = 10^{-10}$ eV^2.

The Mikheyev-Smirnov-Wolfenstein (MSW) effect [Wol78, Mik85] postulates that flavor oscillations are enhanced in (solar) matter. This would lead to a shorter oscillation path thus corresponding to a larger neutrino-mass difference of $\Delta \mathrm{m}^2 = 10^{-5}$ eV^2. The MSW model assumes that an interaction between leptons and their corresponding neutrinos could create an effective mass of each neutrino flavor depending on the matter density. Interaction of electron neutrinos with electrons is one order of magnitude more probable than with other leptons. At a critical electron density, a resonant conversion $\nu_{\mathrm{e}} \rightarrow \nu_{\mu}$ would occur even for very small mixing angles. The deficit of electron neutrinos would then be an effect of conversions in one direction only, towards muon neutrinos. This mechanism would explain the observed deficiencies of the neutrino fluxes and due to its energy dependence, a selective suppression of p+p, ^{7}Be, or ^{8}B neutrino fluxes would provide sufficient fits to the data. The ^{8}B neutrino flux is the only one to provide information on its energy distribution (KAMIOKANDE). That is why it is so important to have both its precise measurement and a reliable prediction of a solar model. On the other hand, the cross-section of $^{7}\mathrm{Be}(\mathrm{p},\gamma)^{8}\mathrm{B}$, the source reaction of the ^{8}B neutrinos, is the worst known input to solar models. To constrain the parameters for neutrino oscillations it is of key importance to fix this nuclear input.

Determination of the neutrino oscillation parameters from the solar neutrino experiments are reviewed in [Bah98b, Fio94]. Other possible particle-physics solutions are discussed in [Bah89a].

1.2 Motivation

As we have seen, the presently most likely interpretation of the solar neutrino problem involved new neutrino properties, beyond standard electroweak theory. To test quantitatively the hypothesis of neutrino oscillations one must both measure and predict very precisely the solar neutrino fluxes. The flux of the ^{8}B neutrinos is negligible (0.01%) compared to the flux of the p+p neutrinos. However, it dominates the signal of the chlorine detector (about 75%), and is the only component detected by KAMIOKANDE. For this reason, the high-energy ^{8}B neutrinos play a crucial role in the solar neutrino problem. Unfortunately, the cross-section for the ^{8}B-production reaction, $^7\mathrm{Be}(\mathrm{p},\gamma)^8\mathrm{B}$, is the worst known nuclear input to SSM, with an accuracy of -11% +21% [Ade98].

It is the goal of this work to remeasure the $\mathrm{p} + {}^7\mathrm{Be}$ cross-section (conventionally given by the astrophysical factor S_{17}, see Chapter 2) in an inverse approach – the Coulomb dissociation (CD) of ^{8}B. Before the method and the pioneering experiment in the field, performed in RIKEN, Japan, is presented, the direct measurements of S_{17} are reviewed.

1.2.1 Direct measurements

At energies relevant to the solar production of ^{8}B (see Chapter 2 for a concept of the Gamov peak), about 18 keV, the rate of the $^7\mathrm{Be}(\mathrm{p},\gamma)^8\mathrm{B}$ process is extremely small due to repulsion of the Coulomb barrier. The (p,γ) cross-section of the order of pikobarns cannot be measured directly with the present experimental technique. Therefore conclusions about its rate at the solar temperature must be drawn by extrapolations from higher energies. The extrapolation methods, however, require theoretical models. The measurements by themselves are very difficult. The ^{7}Be target decays with a half-life of 53.29 days so, in order to collect enough statistics, sophisticated methods of normalizing the target thickness must be performed. Additionally, the target activity is a serious experimental drawback, and a reduction of background is crucial.

Seven experiments reported results for the $^7\mathrm{Be}(\mathrm{p},\gamma)^8\mathrm{B}$ reaction. First, the β^+ activity of ^{8}B was observed [Kav60]. An improved measurement by Parker *et al.* [Par66] detected the β^+-decay ($\tau_{1/2}$ = 770 ms [Ajz88]) in coincidence with the α (see Fig. 1.5). This approach which reduces substantially the background, has become a principle of all subsequent $^7\mathrm{Be}(\mathrm{p},\gamma)^8\mathrm{B}$ experiments [Kav69, Vau70, Wie77]. A very comprehensive experiment was reported by Filippone *et al.* [Fil83], who measured the cross-section at the lowest (117 keV) relative energy ever (it was possible with a H_2^+ molecular beam instead of protons). The most recent measurement was performed by Hammache *et al.* [Ham98].

All direct measurements use a radioactive ^{7}Be target produced by a proton bombardment of stable ^{7}Li. Afterwards, ^{7}Be is chemically separated, purified and deposited onto a platinum backing. To remove volatile contaminants, the target is flamed red-hot to BeO (see [Fil83]). Since ^{7}Be decays back to ^{7}Li (Fig. 1.5) with the half-life of 53.29±0.07 days [Ajz88], to determine the absolute $^7\mathrm{Be}(\mathrm{p},\gamma)^8\mathrm{B}$ cross-section one must measure its effective thickness. It can be done by one of the two methods

- by scanning the γ-ray activity of the target. The decaying ^{7}Be emits the 478 keV photons whose detected yield is a function of the relative position: target - detector. The observed target area must be larger than the beam and collimator diameter to provide only the active target spot [Wie77, Fil83, Ham98].

- by bombarding the target with a deuteron beam and determining the ^{7}Li build-up from the ^{7}Be decay by the yield of α-particles coming from $^7\mathrm{Li}(\mathrm{d},\mathrm{p})^8\mathrm{Li}$. The excitation function of ^{8}Li has a 200 keV-wide resonance at the deuteron energy 780 keV. Its magnitude gives an absolute calibration of the target thickness assumed the total $^7\mathrm{Li}(\mathrm{d},\mathrm{p})^8\mathrm{Li}$ cross-section is known [Kav60, Kav69, Par66, Vau70, Fil83, Ham98].

The first method is direct but the second one has the advantage to measure the beta-delayed ^{8}Li-alphas with the same efficiency as the alphas of ^{8}Be. Therefore the detection-efficiency uncertainties mostly cancel out. A problem which remains is the absolute cross-section for $^7\mathrm{Li}(\mathrm{d},\mathrm{p})$ reported from various experiments, not consistent with each other (see [Str96] for a complete list). The Solar Fusion Rates Conference 1997 [Ade98] (the INT Workshop) has been organized to review all the estimates for the solar reactions. In the case of the (d,p) cross-section a value $\sigma_{\mathrm{dp}} = 147 \pm 11$ mb has been recommended.

In Fig. 1.6 we can see all the direct measurements of the S_{17} astrophysical factor. They are normalized to the same, recommended value of the $^7\mathrm{Li}(\mathrm{d},\mathrm{p})^8\mathrm{Li}$ cross-section. As we can see, the results are not consistent. Even if we do not adopt the single point of Wiezorek *et al.* [Wie77], and the early results of Kavanagh *et al.* [Kav60], still five well documented direct-capture experiments

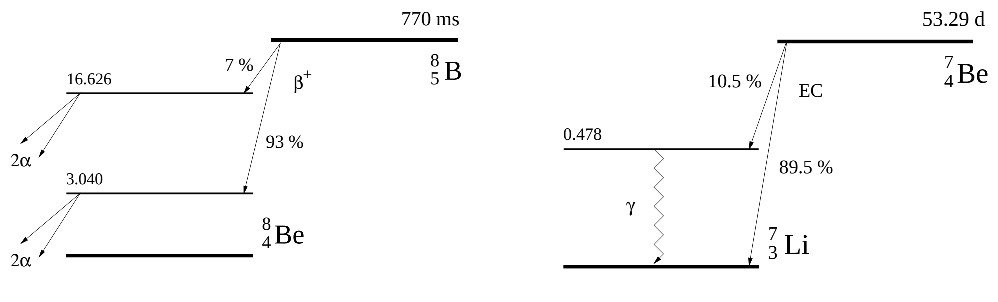

Figure 1.5: *Spectroscopy of the ^{8}B β-decay and the unstable ^{7}Be target [Ajz88].*

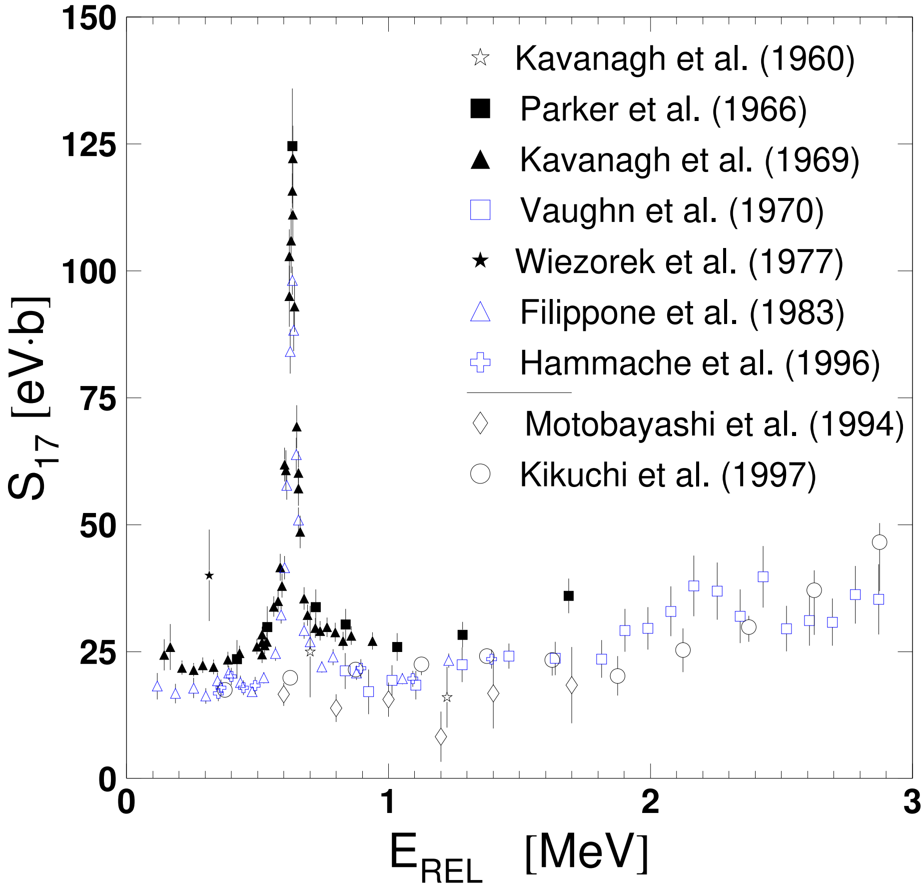

Figure 1.6: *Existing data on S_{17} from direct-capture measurements. These results are normalized to the ^{7}Li$(p,d)^8$Li cross-section of 147±11 [Ade98]. The Coulomb dissociation data of Motobayashi [Mot94] and Kikuchi [Kik98a] from the RIKEN CD-experiment are also presented.*

present values of the (p,γ) cross-section that fall into two groups agreeing in the energy dependence but disagreeing in the absolute cross-section by about 30%. Recently Weissman and coworkers [Wei98] from the Weizmann Institute, and the Bochum group [Str96] remeasured the $^7\mathrm{Li(d,p)}^8\mathrm{Li}$ cross-section. They found a value of 155±8 mb (Weissman) and 153±6 mb or 146±5 mb when some values from the data set were removed (Strieder). The most important message of their reports, however, was the observation of the loss of ^{8}Li recoil nuclei due to back-scattering from the target backing. These results confirmed their systematic calculations with the code TRIM [Str98], that the losses are large for the combination of thin targets and heavy backings and increase with decreasing deuteron energy. They predicted a similar effect for the $^7\mathrm{Be}(\mathrm{p},\gamma)^8\mathrm{B}$ reaction since targets in all the (p,γ) experiments were deposited on a platinum disk. To

		detection
target production	${}^{7}_{3}\mathrm{Li}(\mathrm{p,n})^{7}_{4}\mathrm{Be}$	
reaction studied	${}^{7}_{4}\mathrm{Be}(\mathrm{p},\gamma)^{8}_{5}\mathrm{B} \xrightarrow{\beta^+} {}^{8}_{4}\mathrm{Be}^* \rightarrow 2\,\alpha$	α coinc. e^+
decaying target	${}^{7}_{4}\mathrm{Be} \xrightarrow{\mathrm{EC}} {}^{7}_{3}\mathrm{Li} + \gamma + \nu_\mathrm{e}$	γ
normalization	${}^{7}_{3}\mathrm{Li}(\mathrm{d,p})^{8}_{3}\mathrm{Li} \xrightarrow{\beta^-} {}^{8}_{4}\mathrm{Be}^* \rightarrow 2\,\alpha$	α coinc. e^-

Table 1.2: *Reactions involved in the direct-capture measurements.*

evaluate whether losses of ^{8}B and ^{8}Li nuclei in the direct measurements of S_{17} are compensated one should know precisely the chemical composition of the target. Unfortunately, except for the experiments of Filippone *et al.* [Fil83] and Hammache *et al.* [Ham98], no details on target preparations are known. This limits possible corrections on results of the previous experiments in the normalization of the S_{17}-factor. The authors suggested only to attribute 15% larger error bars to the low-energy data points which are subject the most to the back-scattering effect.

One can conclude that it is not clear now how this discovery affects the existent data. Filippone *et al.* and Hammache *et al.* who used both methods to determine the target thickness, have reported an agreement between them. It is still an open question why there are two groups of data inconsistent by about 30% in the absolute cross-section. Uncertainties due to the back-scattering effect cannot explicitly eliminate the upper data sets (Kavanagh'69 [Kav69],Parker [Par66]); in fact the lower group of results seems to be favored (Filippone [Fil83] + Hammache [Ham98], Vaughn [Vau70]) due to available details of their experimental procedures.

Provided the normalization of the experimental data is done properly, still one complication is attributed to the (p,γ) measurements, namely the cross-section for $^7\mathrm{Be}(\mathrm{p},\gamma)^8\mathrm{B}$ at the Gamov peak, about 18 keV, is too small to be measured directly. An extrapolation from existing data to the relevant astrophysical energies is needed. There are two issues that must be considered: the theoretical energy-dependence, which in turn depends on models, and an overall normalization of a given model, that is, a fit to the experimental data.

Two main approaches have been proposed for a nuclear model of ^{8}B. The cluster-model microscopic calculations [Joh92, Des94, Cso95] assume a $^7\mathrm{Be} + \mathrm{p}$ structure where ^{7}Be is described as a $^4\mathrm{He} + {}^3\mathrm{He}$ two-cluster subsystem. It was claimed by Barker [Bar95] that since cluster models predict the absolute magnitude as well as the energy dependence, they contain no adjustable parameters, and are not in agreement with the experimental values for the mirror system ^{7}Li. This deficiency was assumed to lead to higher values of $S_{17}(E_{\mathrm{REL}} = 0)$. Indeed,

the cluster model calculations present results $S_{17}(0) \geq 24\,\mathrm{eV{\cdot}b}$ (Descouvemont & Baye'94 [Des94]), and $S_{17}(20\,\mathrm{keV}) = 24.6 \div 26.1\,\mathrm{eV \cdot b}$ (Csòtò [Cso95]).
Potential models use a single-particle description of ^{8}B. It is validated by calculations of the overlap integrals of the ^{7}Be and ^{8}B ground states (see [Bro96] and [Nun97] for a review) to be close to unity (see also Section 2.1.2). A mean-field approach is very successful regarding the halo properties of ^{8}B [Neg96]. Results of the potential models preferring a high value of $S_{17}(0)$ [Kim87, Kra93] were criticized by Barker [Bar88]. The same author deduced $S_{17}(0) = 17 \pm 3\,\mathrm{eV{\cdot}b}$ from an R-matrix approach. A recent coupled-channels study of Bertulani [Ber96c] for indirect break-up experiments also prefers a 'lower' value of $S_{17}(0)$, about 20 eV·b.

To minimize the influence of a given model, one must limit the extrapolation only to the low-energy ($E_{REL} < 400$ keV) region where nuclear distortion plays no role, due to the low binding energy in the system ^{7}Be + p, 137 keV. The ^{7}Be(p, γ)^{8}B reaction at low energies is almost entirely a peripheral process sensitive mainly to the asymptotic normalization of the bound-state wave-functions of ^{8}B (Whittaker functions in the two-body channel ^{7}Be + p). Its energy dependence is dominated by an E1 s-wave capture (characteristic upturn of S_{17} towards low energies), and an admixture of a d-wave (disappearing at zero energy) [Ade98]. This approach has a double advantage: one avoids application of theoretical calculations above 400 keV, and does not need to subtract the res-

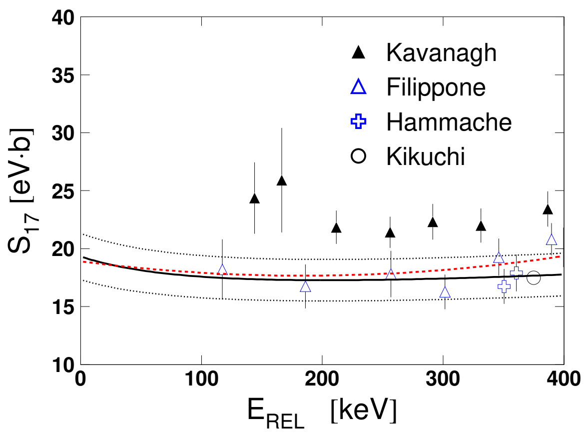

Figure 1.7: *Extrapolations of S_{17} to the astrophysical energies, conventionally zero, from the lower-value data sets. The dashed line represents a microscopic calculation of Johnson et al. [Joh92], as recommended by the Solar Fusion Rates Conference '97 [Ade98], fitted to the data of Filippone (within $E_{REL} < 0.4$ MeV). The solid line with an error band shows a rational approximation following the concept of the pole and the hard-sphere repulsion by Jennings et al. [Jen98] fitted to the data of Filippone [Fil83] and Hammache [Ham98] in the same low-energy range.*

onance at $E_{REL} = 632$ keV (see Fig. 1.6), which, though existent in the (p,γ) data, has absolutely no meaning at the Gamov peak.
There are three motivated approaches to extrapolations towards low energies

- Due to the peripheral nature of $^7Be(p,\gamma)^8B$ at very low energies, an overall normalization of S_{17} can be determined from the asymptotic normalization coefficient (ANC), or the nuclear vertex constant (NVC), by studying the overlap integral of the ^8B and ^7Be ground states. This method was developed by the Tashkent group and at the Texas A&M University. It was found $S_{17}(0) = 17.6$ eV·b [Xu94]. The authors suggested determination of $S_{17}(0)$ from analysis of the $^7Be(^3He,d)^8B$ reaction [Muk95]. The $^{10}B(^7Be,^8B)^9Be$ reaction at 84 MeV/u was used to find $S_{17}(0) = 17.8 \pm 2.8$ eV·b [Azh99].

- Jennings *et al.* [Jen98] developed a description for the astrophysical S_{17}-factor from two concepts: the pole in S_{17} at the binding energy 137 keV, where the photon energy vanishes, and an effective hard-sphere radius as a model for the nuclear distortion. These concepts lead to a rational approximation for the energy dependence of S_{17}. They obtained the radius of the hard sphere by a comparison with (mainly) potential models. A fit to the data determines the asymptotic strength (the pole residue) which is a built-in free parameter. The developed extrapolation formula reads (energy in MeV)

$$S_{17}(E) = S_{17}(0)\left[\left(\frac{0.0408}{0.1375 + E} + 0.7033\right) + 0.343\,E\right] \tag{1.2}$$

- In the low-energy regime the semiclassical WKB approximation is valid. The function S(E) is slowly varying and can be well approximated by a quadratic energy-dependence describing s-wave tunneling through the Coulomb barrier of two point-like nuclei. Such parameterization was first studied by Williams & Koonin [Wil81], adopted by Johnson *et al.* [Joh92], and then used by the Solar Fusion Rates Conference'97 [Ade98] to fit the Filippone data up to 300 keV. For the formula

$$S_{17}(E) = S_{17}(0) + S'_{17}(0)\,E + \frac{1}{2}S''_{17}(0)\,E^2 \tag{1.3}$$

  they found $S'_{17}(0)/S_{17}(0) = -0.71 \pm 0.2$ MeV^{-1}, $S''_{17}(0)/2S_{17}(0) = 1.93 \pm 0.3$ MeV^{-2}, and $S_{17}(0) = 19^{+4}_{-2}$ eV·b

After this compact review one concludes that the direct-capture approach has the following drawbacks

- Experimental procedure is very difficult (preparation of the ^{7}Be target and evaluation its effective thickness, measurements with radioactivity).
- The overall normalization of S_{17} is uncertain about 30% (the two groups of data).
- One must use extrapolations to reach the Gamov peak from the measured data (rapid drop of σ_{17} towards low energies).

A very interesting indirect method was reported by Liu and coworkers [Liu96] who analyzed angular distributions for the transfer reaction ^{7}Be(d, n)^{8}B at E_{CM} = 5.8 MeV. By the ANC method, they derived the astrophysical factor at zero energy for ^{7}Be(p, γ)^{8}B to be 27.4 ± 4.4 eV·b. An attempt of the Bochum group to measure the (p, γ) cross-section in the setup of a ^{7}Be beam and a hydrogen target (see [Rol88] for all details) is also noticeable. First results from this experiment have been published recently [Gia00].

1.2.2 CD-measurements

The electromagnetic excitation to continuum states, Coulomb dissociation (breakup), is proposed as an alternative method to study radiative capture reactions, especially of astrophysical interest (see [Bau94, Bau96]). In absence of sources the matrix elements of the Coulomb excitation, within the restriction of a first-order process, are exactly the same as for a reaction with real photons i.e. a photonuclear reaction (see Chapter 2 for a study). We take advantage of this by studying the inverse of the ^{7}Be(p, γ)^{8}B reaction (see Fig. 1.8) and applying the detailed balance theorem to obtain the direct-capture cross-section. In addition to the phase-space effect, virtual photon fluxes, induced during the Coulomb excitation, enhance considerably the cross-section [Ber88]. To gain a coherent Coulomb field acting on a fast projectile, a high-Z target must be used (usually lead). Depending on the beam energy, the (p, γ) cross-section is enhanced by about three orders of magnitude in the Coulomb dissociation (at E_{LAB} = 254 MeV/u). Because the target is stable (^{208}Pb), its thickness is limited only by resolution; there are no disadvantages of production, use, and normalization of the radioactive ^{7}Be. In fact, the thickness of the Coulomb dissociation target is a compromise between two factors: within a few days of the experiment one wants to collect a reliable statistics (intensity of the secondary ^{8}B beam is usually some orders of magnitude lower than that of primary beams so one must compensate it with a thicker target), on the other hand the small-angle scattering must be

Figure 1.8: *Principle of the direct-capture and the Coulomb-dissociation approach.*

minimized (resolution). Fortunately, the detection efficiency is high, since in the Coulomb dissociation (CD), high-energy charged particles are measured.
In CD we deal with bare ^{8}B ions, therefore the cross-section measured with this method is free from laboratory screening of the bound electrons which are not present in the Sun due to its full ionization. It is worth mentioning even though the laboratory screening is dominated by the stellar plasma screening of free electrons (more than 80%) [Ade98].
Finally, a theoretical study of the Coulomb dissociation process profits from a very good validity of the semiclassical description (see Chapter 2).

The drawbacks of the Coulomb dissociation are as follows.
The process $^8\mathrm{B} \rightarrow ^7\mathrm{Be} + \mathrm{p}$ is dominated by the dipole excitation E1. The M1-resonance at E_{REL} = 632 keV (see Fig. 1.6) corresponds to a transition to the first excited state in ^{8}B with E_γ = 769 keV [Ajz88]. At the Gamov peak of about 18 keV this resonance has a negligible contribution. This is no longer true in the Coulomb dissociation due to a high flux of M1 equivalent photons. In CD a discrimination of the resonance data from the cross-section is crucial to extract the S_{17}-factor. Also an influence of the E2 transitions to the main dipole excitation must be investigated. The strength of the E2 multipolarity depends strongly on models of ^{8}B used as input to CD calculations [Gai95]. There is no clear situation in this respect; in different studies E2 varies by a factor of 4 (see [Kim87, Typ97] and [Shy96] for further references). Experimentally it is possible to disentangle the admixture of E2 to the CD cross-section by its strong manifestation in the angular distributions (at large angles) and possible interference effects with E1, producing asymmetries in the longitudal momentum distributions of the break-up partners [Esb96]. In fact, to interpret measurements by theoretical predictions, experimental angular accuracy and resolution must be necessarily high (about the E2 problem see later in this section).

Since a nuclear break-up may influence the pure electrodynamical effect, it is important to study with CD only weakly bound systems. It is the case for ^{8}B where the proton separation-energy amounts to only 137 keV. However even here the contribution of the nuclear break-up is not negligible if extremely low laboratory energies of ^{8}B are applied. Independent of energy, above the grazing angle (small impact parameters) one can always expect a nuclear contribution; pure Coulomb break-up events can be principally studied only in forward kinematics (see e.g. [Nun98]).

Effects of postacceleration may influence kinematic observables of the Coulomb break-up process as well. In a classical description higher-order effects induce different acceleration of the fragments due to different ratios of Z/A of the fragments and their different trajectories in the inhomogeneous Coulomb field. In a quantum description this is equivalent to multiple absorption of virtual photons. As a consequence, the final state is distorted and does not correspond to a clean Coulomb break-up. It is relevant if the relative momentum of the two partners is of the same order of magnitude as the additional momenta of the fragments due to reacceleration. It has been shown [Ber93a, Esb95] that a correct approach to the problem of the higher order effects is solving the time-dependent Schrödinger equation in a non-perturbative formalism. Since reacceleration is an effect of deformation of the relative motion of the fragments after the break-up, it does not depend on the magnitude of probability for the break-up (which can be small), and therefore it cannot be treated as an expansion in a perturbative way.

The above effects: the multipolarity composition, the nuclear break-up, and the higher-order effects depend on energy of the incident ^{8}B. One can control their effect on the pure Coulomb dipole break-up by performing experiments at different energies.

Another disadvantage of the CD of ^{8}B is a break-up to the first excited state in ^{7}Be, 429 keV, instead of feeding only its ground state. The CD data must be corrected for this effect before extracting the astrophysical S_{17}-factor. One can determine experimentally the ratio between feeding the two states by measuring the emitted γ-rays as a function of the relative energy p-Be (see discussion in Chapter 4).

The pilot study of the CD approach was the Karlsruhe experiment with a 156 MeV ^{6}Li beam [Kie91] (see also [Bau96]) studying the break-up of ^{6}Li into α and deuteron.

The first experiment of the Coulomb dissociation of ^{8}B was performed in RIKEN, Japan. There exist two data sets, one of the original setup [Mot94, Iwa96] (RIKEN-I) and the improved one [Kik97, Kik98a] (RIKEN-II). A sketch of the experiment is shown in Fig. 1.9. This first measurement of the $^7\mathrm{Be}(\mathrm{p},\gamma)^8\mathrm{B}$ cross-section with the Coulomb dissociation method ($\mathrm{E_{LAB}}(^8\mathrm{B}) \approx 50$ MeV/u) was a motivation for the GSI experiment. Therefore, it will be briefly discussed.

The radioactive ^{8}B-beam was produced through projectile fragmentation of the primary ^{12}C in the fragment separator RIPS. Its intensity was about $2 \cdot 10^4$ ions

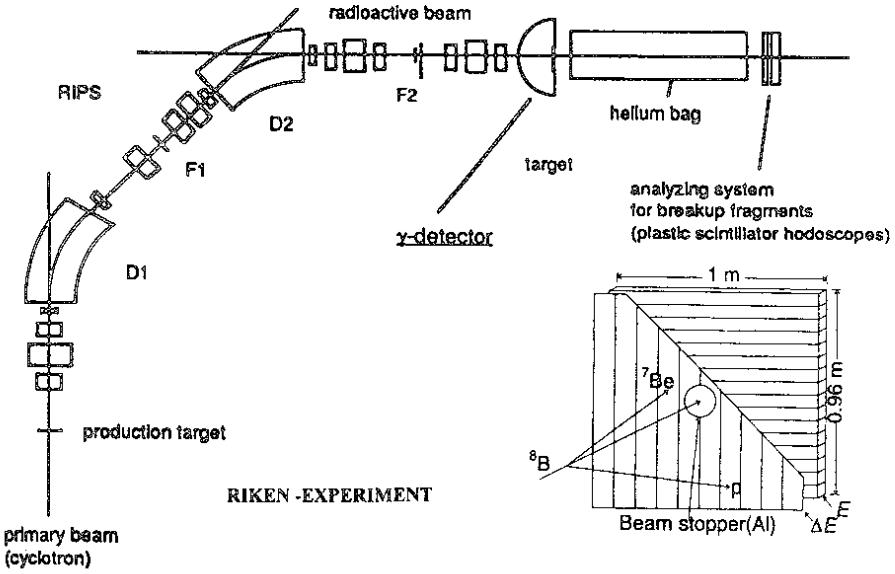

Figure 1.9: *Setup of the RIKEN Coulomb-dissociation experiment [Iwa96].*

per spill. The secondary beam bombarded the 50 mg/cm^2-thick lead target. The γ-ray activity coming from feeding the first excited state ^{7}Be*, 429 keV, was measured with a matrix of scintillators around the target. It was done in coincidence with the detected proton and ^{7}Be with efficiency of about 20%. The break-up products themselves hit a plastic-scintillator hodoscope with an active area of 1.0×0.96 m^2 divided into $6{\times}10$ cm^2 segments (in RIKEN-II the width of the central segments was reduced to increase the resolution at small angles) measuring both the energy loss and the total energy of the particle. A helium bag between the target and the hodoscope was placed to reduce the multiple Coulomb scattering and secondary reactions. In spite of it, the background reactions were dominant and the relative-energy spectrum had to be obtained by a subtraction of the with- and without-target yields. This limited the accuracy thus influencing the lowest relative energy that could be measured. The positions of the break-up partners on the hodoscope were used not only to measure the relative energy p-Be, but also to determine the angle of the excited ^{8}B relative to the beam spread. Because it was the aim of RIKEN-II to cover larger angular space (to focus on the E2 strength), the hodoscope was placed closer to the target which results in slightly worse resolution in RIKEN-II, compared to the original setup. Differences between the both experiments are listed in Tab.1.3.

To interpret the RIKEN data, the authors simulated their experimental setup. They found that no E2 component was observed [Kik97] and extracted the astrophysical factor S_{17} under the assumption that the break-up to continuum was of

pure dipole nature. They applied theoretical energy-dependence [Bar86, Des94] to obtain $S_{17}(0) = 18.9 \pm 1.8$ eV·b. The RIKEN data at low relative energy agree with the direct-capture results of Filippone [Fil83] and Hammache [Ham98].
Some details about their experimental procedures are not available from the RIKEN publications e.g. the application of the correction for feeding the first excited state in ^{7}Be from the measured γ-rays. Taking into account the subtraction of the background the error-bars seem to be underestimated especially at low E_{REL}.
It is no doubt, however, that this was a pioneering and successful experiment in the field.

Here, the E2 amplitude is worth further mentioning. The authors of the RIKEN experiment concluded that no E2 was observed. The same was reported from the sub-Coulomb experiment at 26 MeV (3.3 MeV/u) at the Notre Dame University [Sch96] where the E2 component is expected to be even more enhanced because the ratio E2/E1 increases with decreasing bombarding energy [Shy97, Nun98]. It is controversial in view of the experiment of Kelley *et al.* at 41 MeV/u [Kel96] who found a characteristic signal of the E1-E2 interference in the longitudal ^{7}Be-momentum distributions. Davids *et al.* [Dav98] performed an improved experiment at 81 MeV/u and determined $S_{E2}/S_{E1} = 6.7^{+2.7}_{-1.9} \times 10^{-4}$ at $E_{REL} = 0.63$ MeV using the model of Esbensen and Bertsch [Esb96]. It seems, although it is not clear if the RIKEN and Notre Dame data do not suffer from effects of background and/or experimental accuracy, that more theoretical studies are necessary to investigate the role of the E2 amplitude. Especially interference effects between the Coulomb waves and between the Coulomb and nuclear force still need careful investigations. Esbensen and Bertsch [Esb96] pointed out that higher-order dynamical effects may reduce the interference pattern E1-E2 and also the effect of the E2 transitions compared to predictions of the first-order process. This would explain why, although there is an E2 strength present, the CD data show its effect only partially, much smaller than what could be obtained by a simple sum of the E1 and E2 components. Therefore it seems that E2 may not affect the extraction of S_{17}.

	$E_{LAB}(^{8}B)$ [MeV/u]	E_{REL} [MeV]	σ_{EREL}/E_{REL} [keV]/[MeV]	T-Hod. [m]	θ_8^{max}	θ_8^{min}	γ-det
RIKEN-I	46.5	0.6-1.7	100/0.6, 130/1.7	5.0	6^0	0.80^0	$66\times BaF_2$
RIKEN-II	51.9	0.4-3.0	120/0.5, 150/1.5	3.1	10^0	1.29^0	$54\times$NaI(Tl)

Table 1.3: *Details of the two RIKEN setups.*

We have recognized the solar neutrino problem and the importance of the high-energy-neutrino producing-reaction in the Sun, ^{7}Be(p, γ)^{8}B, and we have reviewed the direct-capture and the Coulomb dissociation approach in measurements of the astrophysical factor S_{17}. Let me now summarize all the motivations for the GSI Coulomb dissociation experiment ^{208}Pb(^{8}B, ^{7}Be + p)^{208}Pb at 254 MeV/u [Sum94]:

- The solar neutrino problem cannot be solved by a manipulation of the astrophysical factor S_{17}. However, it is the most inaccurate nuclear input to solar models and it is desirable to fix it in a quantitative way.

- The working hypothesis is that the Coulomb dissociation method is an alternative approach to measure the direct-capture ^{7}Be(p, γ)^{8}B cross-section;

  - at the bombarding energy 254 MeV/u the nuclear break-up is roughly three orders of magnitude lower than the Coulomb break-up. It has been shown in calculations based on a potential model [Ber98], and in the DWBA formalism [Shy96, Shy99].
  - the relativistic energy of 254 MeV/u suppresses higher-order effects fully. In [Typ97] corrections to the first-order semiclassical description were studied at the projectile energies of 50 MeV/u (RIKEN) and 254 MeV/u (GSI). The negligible modification of the final relative-motion energy is shown clearly in Fig.11 of [Ber95].
  - multipolarities in CD at the GSI energy:
    a relative ratio E2/E1 is twice smaller than at 50 MeV/u. Since at RIKEN no E2 component has been found [Kik97], consequently it is an additional strong indication to neglect E2 in the extraction of S_{17}; the M1-resonance is, in turn, enhanced by a factor of about 1.5 at GSI in comparison with RIKEN.
  - feeding the first excited state in ^{7}Be [Ajz88] is corrected for using the branching ratio measured in the RIKEN experiment [Kik98b]. The RIKEN results are discussed in [Men98] in connection with the respective spectroscopic factors.

- A Coulomb dissociation experiment at a higher beam energy allows us using the high-acceptance spectrometer KaoS [Sen93] to identify in coincidence the break-up products. Therefore their relative energy can be measured event-by-event, without subtracting background reactions. This assures better accuracy than in RIKEN thus giving possibility to reach lower relative energies. In order to improve the resolution, the angular and energy straggling is reduced by filling the spectrometer with helium (instead of air).

1.3 Experimental goal

The goal is to study the cross-section for the Coulomb dissociation process $^{208}\mathrm{Pb}(^{8}\mathrm{B}, {}^{7}\mathrm{Be} + \mathrm{p})^{208}\mathrm{Pb}$ in a kinematically complete measurement. An exclusive experiment where all particles in the output channel are detected and their momentum vectors are measured gives us the possibility to reproduce the invariant mass of the system.

We identify the break-up products, ^{7}Be and proton, in coincidence, measure their absolute momenta $\vec{\mathbf{p}}_{\mathbf{Be}}$, $\vec{\mathbf{p}}_{\mathbf{p}}$ in the double-focusing kaon spectrometer KaoS, and determine the opening angle $\theta_{\mathbf{17}}$ between the fragments by reconstructing the reaction vertex.

From these observables the invariant mass is deduced

$$\mathrm{m}_{\mathrm{B}}^{*} = \sqrt{(\mathrm{E}_{\mathrm{Be}} + \mathrm{E}_{\mathrm{p}})^2 - (\vec{\mathrm{p}}_{\mathrm{Be}} + \vec{\mathrm{p}}_{\mathrm{p}})^2} = \mathrm{f}\,(\vec{\mathrm{p}}_{\mathrm{Be}}, \vec{\mathrm{p}}_{\mathrm{p}}, \cos(\theta_{17})) \tag{1.4}$$

or equivalently, the relative energy of the break-up partners

$$\mathrm{E}_{\mathrm{REL}} = \mathrm{m}_{\mathrm{B}}^{*} - (\mathrm{m}_{\mathrm{Be}} + \mathrm{m}_{\mathrm{p}}) \tag{1.5}$$

By cumulating events due to their $\mathbf{E_{REL}}$ we measure the differential cross-section $\mathrm{d}\sigma/\mathrm{dE}_{\mathrm{REL}}$.
The angular distribution of the excited ^{8}B, $\mathrm{d}\sigma/\mathrm{d}\Omega_8$, is measured by determining the scattering angle $\theta_{\mathbf{8}}$, which is the angle between the incident $\vec{\mathbf{p}}_{\mathbf{B}}$ and the transferred momentum $\vec{\mathrm{p}}_{\mathrm{Be}} + \vec{\mathrm{p}}_{\mathrm{p}}$.

So, in the experiment the double-differential cross-section $\mathbf{d^2}\sigma_{\mathbf{CD}}/\mathbf{d}\Omega_{\mathbf{8}}\,\mathbf{dE_{REL}}$ for the Coulomb dissociation $^{8}\mathrm{B} \rightarrow {}^{7}\mathrm{Be} + \mathrm{p}$ can be measured.

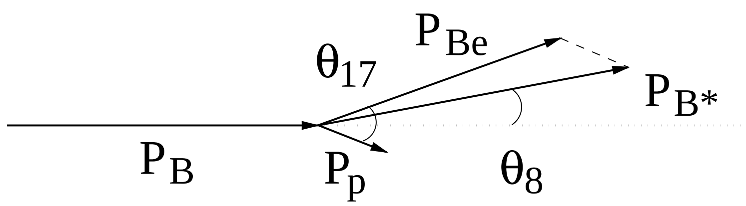

Figure 1.10: *Definition of the opening angle θ_{17} and the scattering angle θ_8.*

Chapter 2

Methods

The aim of this chapter is to introduce a formalism necessary to study the problems this work treats with. First, a compact description of the reaction kinematics, $^7\mathrm{Be}(\mathrm{p},\gamma)^8\mathrm{B}$, in the solar interior is given. The excitation function of this process is dominated at the solar temperature by the direct-capture mechanism. This and the case of a capture on tails of a resonance is discussed. Then the concept of the Coulomb dissociation is introduced and related to the direct approach cross-section in a quantitative way. Because the Coulomb dissociation $^{208}\mathrm{Pb}(^8\mathrm{B},{}^7\mathrm{Be}+\mathrm{p})^{208}\mathrm{Pb}$ can be treated as a photonuclear reaction studied with equivalent photon fluxes, i.e. as the inverse process to $^7\mathrm{Be}(\mathrm{p},\gamma)$, it is shown how to measure the astrophysical factor S_{17} with this indirect method. In the third section electromagnetic excitation is described. The concept of equivalent photon fluxes is of key importance for this study therefore it was the intention of the author to give a compact but possibly comprehensive description starting from a scratch. The calculations, though conceptually well understood and therefore always skipped in reviews, are not quantitatively trivial. It is very educative then to derive here the theory of the Coulomb excitation in a way relevant to the kinematics of the experiment of the Coulomb break-up of $^8\mathrm{B}$ at 254 MeV/u.

2.1 Astrophysical reaction rates. Process $^7\mathrm{Be}(\mathrm{p},\gamma)^8\mathrm{B}$

2.1.1 Direct capture

The science of the thermonuclear reactions producing energy in the Sun is very well understood [Cla83, Rol88]. The key concept necessary to study stellar evolution is the energy production $\varepsilon\ \left[\frac{\mathrm{erg}}{\mathrm{g\cdot s}}\right]$ i.e. efficiency of the nuclear fuel. For a collision process between two nuclei $\mathrm{a}\to\mathrm{b}$ one puts

$$\varepsilon_{\mathrm{ab}}=\varepsilon_{\mathrm{ab}}(\rho,\mathrm{T},\mathrm{X},\mathrm{Y},\mathrm{Z})=\frac{\eta_{\mathrm{ab}}}{\rho}\mathrm{Q}_{\mathrm{ab}} \qquad (2.1)$$

where η_{ab} $\left[\frac{1}{cm^3 \cdot s}\right]$ denotes the reaction rate, ρ is the density of the stellar matter and, for the energy amount produced, one can use in a very good approximation a Q-value of the reaction.
The reaction rate

$$\eta_{ab} = n_a\, n_b \frac{1}{1+\delta_{ab}} <\sigma\, v> \tag{2.2}$$

depends on concentrations of the substrates n $\left[\frac{1}{cm^3}\right]$, the Kronecker delta prevents from double counting of identical particles, and the specific (for one pair) reaction rate $\left[\frac{cm^3}{s}\right]$ is

$$<\sigma\, v> = \int \frac{d^3 p_a}{h^3} \int \frac{d^3 p_b}{h^3} f_a(\mathbf{p_a}) f_b(\mathbf{p_b})\, v_{ab}\, \sigma_{ab} \tag{2.3}$$

where $\mathbf{v_{ab}} = \mathbf{v_b} - \mathbf{v_a}$ is the relative velocity of the partners and

$$f(\mathbf{p}) = \left(\frac{h^2}{2\pi mkT}\right)^{\frac{3}{2}} \exp\left(\frac{-p^2}{2mkT}\right) \qquad \int \frac{d^3 p}{h^3} f(\mathbf{p}) = 1 \tag{2.4}$$

is a normalized Maxwell-Boltzmann distribution. Let us transform Eq. 2.3 to the center-of-mass coordinates

$$\begin{pmatrix} \mathbf{P} \\ \mathbf{p} \end{pmatrix} = \begin{pmatrix} 1 & 1 \\ \frac{-\mu}{m_a} & \frac{\mu}{m_b} \end{pmatrix} \begin{pmatrix} \mathbf{p_a} \\ \mathbf{p_b} \end{pmatrix} \tag{2.5}$$

where $\mu = \frac{m_a m_b}{m_a + m_b}$ is the reduced mass, $M = m_a + m_b$, and the Jacobian $\frac{\partial(\mathbf{p_a}, \mathbf{p_b})}{\partial(\mathbf{P}, \mathbf{p})} = 1$. Now $<\sigma\, v>$ may be written as a product of two integrals. The integral over the momentum of the center of mass $\mathbf{P}$ is of the form of Eq. 2.4 and can be done at once yielding unity. Thus the reaction rate per particle pair is reduced to

$$<\sigma\, v> = \sqrt{\frac{8}{\pi\mu}} \left(\frac{1}{kT}\right)^{3/2} \int_0^\infty \sigma(E)\, E\, \exp\left(-\frac{E}{kT}\right) dE \tag{2.6}$$

where the integrand is now expressed in terms of energy. Eq. 2.6 can be calculated explicitly when the energy dependence of the cross-section is known. Considering the Coulomb barrier between two charged particles one has

$$V(r) = \frac{Z_a Z_b\, e^2}{r} = \frac{1.44\, Z_a Z_b}{r\,[fm]} \;[MeV] \tag{2.7}$$

whereas the kinetic energy of the particles corresponding to the temperature T is

$$kT = 8.62 \times 10^{-8} T \;\; keV \tag{2.8}$$

In case of the solar central temperature T = 15×10^6 K, the kinetic energy of the relative motion amounts to 1.293 keV. It is three orders of magnitude lower than the Coulomb barrier for any reaction of the pp-cycle. Particles which can penetrate the Coulomb barrier are these which have relatively high energy in the Maxwell-Boltzmann distribution, however, as we can see in Eq. 2.4, the number of particle pairs with the energy higher than kT decreases exponentially. Therefore the cross-section for a thermonuclear reaction in the core of the star must depend on the quantum effect of the tunneling through the Coulomb barrier. In order to obtain the penetration factor P, the Schrödinger equation with the Coulomb field must be solved [Sch68]. An exact solution of the problem is known, however it requires tabulated values of the Coulomb waves for any combination of the input parameters. Since the bombarding energies in the solar core are much smaller than the repulsive potential, one can use approximate but still more instructive expressions for the penetration factors, based on the WKB method [Cla83]. For the potential from Eq. 2.7, the transmission coefficients can be calculated without details regarding the shape of the nuclear potential and the one-dimensional WKB approximation gives [Sch68]

$$\mathrm{P} = \exp\left(-2\int_{\mathrm{R_n}}^{\mathrm{b}} \kappa(\mathrm{r})\,\mathrm{dr}\right) \tag{2.9}$$

$$\kappa(\mathrm{r}) = +\frac{1}{\hbar}\left(2\mu\left[\mathrm{V(r)} + \frac{\hbar^2\,\mathrm{l(l+1)}}{2\mu\,\mathrm{r}^2} - \mathrm{E}\right]\right)^{1/2}$$

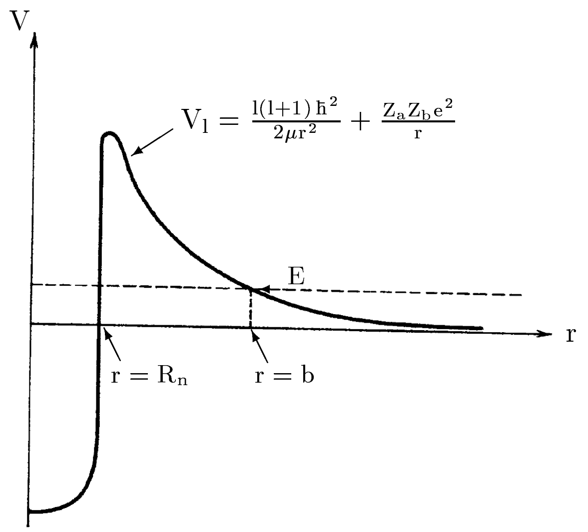

Figure 2.1: *Scheme of the Coulomb plus centrifugal barrier preventing from penetration to the nuclear potential. Projectile incident with energy E has a non-zero probability for the tunneling through the barrier to form a compound nucleus.*

The dominant interaction at low energies is scattering of the spherical wave s, therefore one considers the wave function of spin l=0 only. When point charges are assumed ($R_n \rightarrow 0$), and the upper limit of the integral as the classical turning point, determined from the energy of the incident particle (see Fig. 2.1)

$$E = \frac{Z_a Z_b e^2}{b} \tag{2.10}$$

one gets

$$\int_{R_n \rightarrow 0}^{\frac{Z_a Z_b e^2}{E}} \kappa(r)\, dr = \sqrt{\frac{2\mu}{\hbar^2}} \int_0^{\frac{Z_a Z_b e^2}{E}} \left(\frac{Z_a Z_b\, e^2}{r} - E\right)^{1/2} dr = \frac{\pi Z_a Z_b\, e^2}{\hbar\, v} \tag{2.11}$$

and

$$P = \exp\left(\frac{-2\pi Z_a Z_b\, e^2}{\hbar v}\right) = \exp\left(-2\,\pi\eta\right) \tag{2.12}$$

where $\eta = \frac{Z_a Z_b\, e^2}{\hbar v}$ is the Sommerfeld parameter.

The one-dimensional WKB approximation being satisfying enough in astrophysical considerations, the transmission coefficients one takes in the form of Eq. 2.12.

Apart from the latter energy dependence of the cross-section, the interaction between two particles follows the rules of the quantum mechanics and is proportional to the square of the de Broglie wavelength i.e. inversely proportional to the relative energy [Cla83]

$$\sigma(E) \propto \pi \lambda\!\!\!^{-2} \propto \frac{1}{E} \tag{2.13}$$

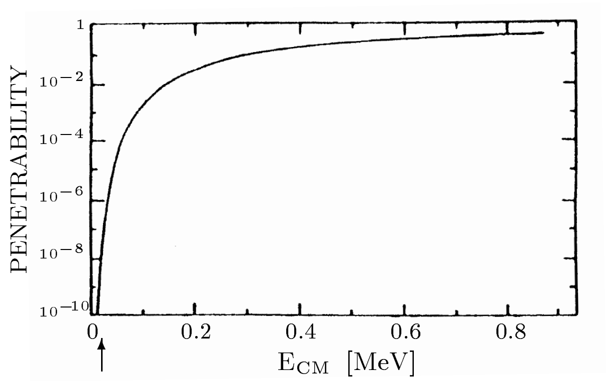

Figure 2.2: *Penetrability of the Coulomb barrier (Eq. 2.12) in the case of the p+p reaction. For the process $^7Be + p$ the curve is shifted to the right as the repulsion is stronger.*

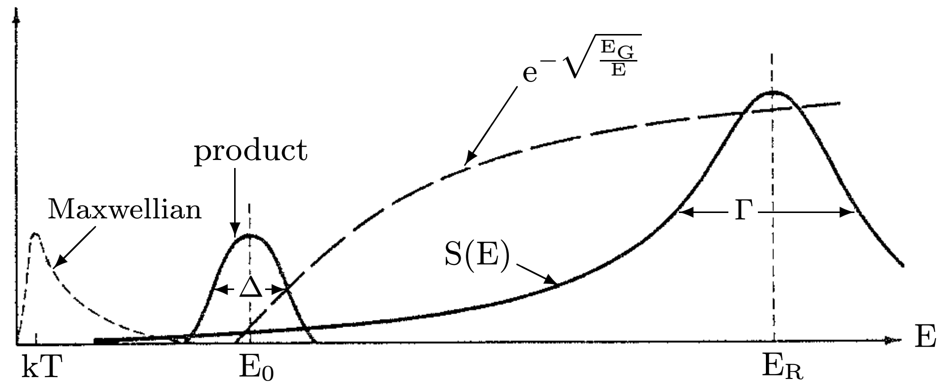

Figure 2.3: *Energy-dependent functions governing a nuclear reaction between charged particles: the thermal energy-distribution and the quantum-mechanical effect of the tunneling through the Coulomb barrier. As a product, the most effective energy for the reaction rate is shown. The astrophysical factor S(E) is a slowly varying function of energy, unless influenced by a resonance in the scheme of nuclear levels [Cla83].*

Finally, an astrophysical factor S(E) – a residual function of energy which remains after factoring out the two strong energy dependences of the cross-section is defined. The astrophysical factor, unlike the two effects above, contains intrinsic nuclear part of the interaction and, assumed there are no resonances in the scheme of nuclear levels, is supposed to be constant or a smoothly varying function of energy. Studying the S-factor and not the rapidly varying cross-section is of great advantage for extrapolation of experimental results to astrophysical energies (compare Fig. 2.2 and Fig. 2.3).
So the cross-section is expressed now in the form

$$\sigma(\mathrm{E}) = \frac{1}{\mathrm{E}} \exp\left(-2\pi\eta\right) \times \mathrm{S}(\mathrm{E}) \tag{2.14}$$

Substituting Eq. 2.14 to Eq. 2.6 one gets

$$<\sigma\,\mathrm{v}> = \sqrt{\frac{8}{\pi\mu}} \left(\frac{1}{\mathrm{kT}}\right)^{3/2} \int_0^\infty \mathrm{dE}\,\mathrm{S}\exp\left(\frac{-\mathrm{E}}{\mathrm{kT}} - \frac{\mathrm{c}}{\sqrt{\mathrm{E}}}\right) \tag{2.15}$$

where parameter c is given by the formula

$$\mathrm{c} = \frac{2\pi \mathrm{Z_a Z_b e^2}}{\hbar}\sqrt{\frac{\mu}{2}} \tag{2.16}$$

Its square is called the Gamov energy

$$\mathrm{E_G} = \mathrm{c}^2 \tag{2.17}$$

Fig. 2.3 shows the product of the contradictory exponents under the integral 2.15: a decreasing probability to interact at lower energies by the Coulomb barrier, and the increasing (with decreasing energy) number of particles due to the Maxwell-Boltzmann distribution. Since the main contribution to the integral 2.15 comes from the narrow peak being the product of both exponents, the integral can be evaluated well enough with the method of steepest descent (see e.g. [Cla83, Rol88]). In this method one replaces a peaked product of two exponents by a Gaussian. Its maximum lies in the maximum of the integrand which is

$$\mathrm{E_0} = \left[\frac{\mathrm{E_G} \times (\mathrm{kT})^2}{4}\right]^{1/3} \tag{2.18}$$

This is the most effective energy for the reaction rate (instead of 2.17 $\mathrm{E_0}$ is usually referred to as the Gamov energy; since now it is also the case in this work unless otherwise stated). It depends upon reaction partners and temperature.

One gets the (full) width of the Gaussian

$$\Delta = \frac{4}{\sqrt{3}}\sqrt{\mathrm{E_0 kT}} \tag{2.19}$$

Finally the reaction rate per particle pair reads

$$<\sigma\,\mathrm{v}> = \sqrt{\frac{2}{\mu}}\left(\frac{1}{\mathrm{kT}}\right)^{3/2} \mathrm{S(E_0)}\ \exp\left(\frac{-3\mathrm{E_0}}{\mathrm{kT}}\right)\Delta \tag{2.20}$$

As an example Fig. 2.2 shows probability of tunneling through the Coulomb barrier for the relative motion p+p with l=0. The arrow shows the relevant astrophysical temperature range of the hydrogen core. In case of the process ^{7}Be + p Eq. 2.18, 2.19 give $\mathrm{E_0} = 17.93$ keV and the width of the peak $\Delta = 11.12$ keV. The above effect of the relative energy shifting $\mathrm{kT} = 1.293 \rightarrow \mathrm{E_0} = 17.93$ keV, at which the highest reaction rate is reached, increases the cross-section several orders of magnitude ($\sigma(\mathrm{E_0})/\sigma(\mathrm{kT}) \approx 10^{31}$), but even at these energies, cross-section of this weak process of radiative capture is too low to be measured directly with the present experimental technique. The state-of-the-art of the direct-capture measurements was reviewed in Chapter 1.

2.1.2 Resonant capture

Resonances are quasistationary states in the compound nucleus. It is known from quantum mechanics that the resonant cross-section has a Lorentzian energy-dependence. For the case of $^7\mathrm{Be}(\mathrm{p},\gamma)^8\mathrm{B}$ one can write

$$\sigma_\mathrm{R}(\mathrm{E}) = \pi\lambda\!\!\!^{-2}\,\omega\,\frac{\Gamma_\mathrm{p}(\mathrm{E})\,\Gamma_\gamma(\mathrm{E})}{(\mathrm{E}-\mathrm{E_R})^2 + (\Gamma_\mathrm{TOT}(\mathrm{E})/2)^2} \tag{2.21}$$

where $\Gamma_\mathrm{TOT} = \Gamma_\mathrm{p} + \Gamma_\gamma$ and, following the formalism as given in [Dec93], the γ-width and the proton-width are functions of energy

$$\Gamma_\gamma(\mathrm{E}) = \frac{\Gamma_\gamma(\mathrm{E_R})\;(\mathrm{Q}+\mathrm{E})^{2\lambda+1}}{(\mathrm{Q}+\mathrm{E_R})^{2\lambda+1}} \tag{2.22}$$

$$\Gamma_\mathrm{p}(\mathrm{E}) = \frac{\Gamma_\mathrm{p}(\mathrm{E_R})\;\exp[-(\mathrm{E_G}/\mathrm{E})^{1/2}]}{\exp[-(\mathrm{E_G}/\mathrm{E_R})^{1/2}]} \tag{2.23}$$

The variables denote: $\mathrm{E_R}$-energy of the resonance, Q = 137 keV-the Q-value of the reaction, $\mathrm{E_G}$-the Gamov energy (Eq. 2.17) and λ-the multipolarity of the gamma transition. The statistical factor ω is equal to $(2\mathrm{J_{RES}}+1)/(2\mathrm{j_{Be}}+1)(2\mathrm{j_p}+1)$. The De Broglie wave-length can be numerically expressed as

$$\pi\lambda\!\!\!^{-2} = \frac{656.6}{\mathrm{A}\cdot\mathrm{E}\,[\mathrm{keV}]}\;\;[\mathrm{barn}] \tag{2.24}$$

for $\mathrm{A} = \frac{\mathrm{A_{Be}A_p}}{\mathrm{A_{Be}+A_p}}$. The latter factor makes the resonant cross-section globally 1/E-dependent.
A possible resonant mode in the capture reaction $^7\mathrm{Be}+\mathrm{p}$ one finds by analyzing the $^8\mathrm{B}$ wave function

$$\Psi_\mathrm{TOTAL} = \sum_{\text{one-particle states}} (\mathrm{I_{core}} = \mathrm{j_{Be}}) \otimes \mathrm{p}\,(\mathrm{j}\;[\mathrm{l},\mathrm{s}]) \tag{2.25}$$

It is assumed (see [Ber98] for references) that the 2^+ ground state of $^8\mathrm{B}$ can be described as a $\mathrm{j_p} = \mathrm{p}_{3/2}$ proton coupled to the $\mathrm{I_{core}} = \mathrm{j_{Be}} = 3/2^-$ ground state of $^7\mathrm{Be}$ with the spectroscopic factor of this configuration taken as unity (for more recent studies see [Sme99])

$$^8\mathrm{B_{g.s.}}(2^+) = 1\cdot{}^7\mathrm{Be_{g.s.}}(3/2^-)\otimes\mathrm{p}\,(3/2^+\;[\mathrm{l}=1,\mathrm{s}=1/2^+]) \tag{2.26}$$

The angular-momentum conservation exhibits two resonant states in $^8\mathrm{B}$

$$\mathrm{J_{RES}} = \mathrm{j_{Be}} + \mathrm{j_p} = \mathrm{j_{Be}} + \mathrm{s} + \mathrm{l} = \frac{3}{2} + \frac{1}{2} \pm 1 = 2 \pm 1 = \;1\;,\;3 \tag{2.27}$$

The parity-conservation rule for the transition with multipolarity $\lambda = 1$ coupling the ground state and these excited states give

$$\pi(\mathrm{J_{RES}}) = (-)^{\lambda}\, \pi(\mathrm{j_{Be}})\, \pi(\mathrm{j_p}) = - \cdot - \cdot + = + \tag{2.28}$$

Indeed there is a sharp resonance $\mathrm{J}^{\pi}_{\mathrm{RES}} = 1^+$ at $\mathrm{E}_{\gamma} = 769 \pm 10$ keV ($\mathrm{E_{REL}} = 632 \pm 10$ keV) [Fil83] and a broad one $\mathrm{J}^{\pi}_{\mathrm{RES}} = 3^+$ at $\mathrm{E}_{\gamma} = 2.34 \pm 0.04$ MeV ($\mathrm{E_{REL}} = 2.20$ MeV) [Bru68] ($\mathrm{E}_{\gamma} = 2.389 \pm 0.072$ MeV is reported in [Vau70]). Gamma rays with $\lambda = 1$ coupling states with the same parity are of M1 type

$$\pi_{\mathrm{M1}} = (-)^{\lambda+1}\, \pi^{^8\mathrm{B}}_{\mathrm{g.s.}} = (-)^2\, \pi^{^8\mathrm{B}}_{\mathrm{g.s.}} = \pi^{^8\mathrm{B}}_{\mathrm{g.s.}} \tag{2.29}$$

The $\mathrm{J}^{\pi}_{\mathrm{RES}} = 1^+$ state has a very narrow width $\Gamma_{\mathrm{p}} = 37 \pm 5$ keV measured by Filippone [Fil83] being in agreement with Eq. 2.23 which yields $\Gamma_{\mathrm{p}} = 37.55$ keV. The γ-width was determined to be $\Gamma_{\gamma} = 25 \pm 4$ meV [Fil83] well compared to $\Gamma_{\gamma} = 25$ meV from Eq. 2.22. Different but consistent with one another values were reported [Bar86] in data of Parker $\Gamma_{\gamma} = 37 \pm 19$ meV and Kavanagh $\Gamma_{\gamma} = 38 \pm 3$ meV for the higher-value $\mathrm{S_{17}}$-factor measurements. A peak resonant cross-section calculated from Eq. 2.21 yields $\sigma_{\mathrm{R}} = 1.2\ \mu$b and was measured to be $\sigma_{\mathrm{R}} = 1.18 \pm 0.12\ \mu$b [Fil83] whereas in [Par66] $\sigma_{\mathrm{R}} = 1.59 \pm 0.16\ \mu$b.

For the second excited state in ^{8}B, $\mathrm{J}^{\pi}_{\mathrm{res}} = 3^+$, one can deduce from Eq. 2.23 $\Gamma_{\mathrm{p}} = 347.5$ keV which is in accordance with a measurement of $\Gamma_{\mathrm{p}} = 390 \pm 40$ keV [McG67]. One can find also a much different value $\Gamma_{\mathrm{p}} = 1280 \pm 440$ keV in [Vau70].

Both resonances are irrelevant for the astrophysical energy range ($\mathrm{E_R} \gg \mathrm{E_0}$) and do not affect $\mathrm{S_{17}(E_0)}$. The reaction rate should be then determined fully by the non-resonant mechanism (Eq. 2.20). The same is not true for the $^8\mathrm{B} + \gamma \rightarrow {}^7\mathrm{Be} + \mathrm{p}$ Coulomb dissociation (see Section 2.3) as an enhancement of the cross-section through M1 equivalent photons plays a role. The latter case needs an extraction of the M1 resonance at $\mathrm{E_{REL}} = 632$ keV from the CD data.

Now we can search for all other transitions coupling the ground state $^8\mathrm{B_{g.s.}}$ and the 1^+, 3^+ excited states and continuum

$$|\mathrm{j_p} - \lambda| \leq \mathrm{j} \leq \mathrm{j_p} + \lambda \tag{2.30}$$

For electric dipole excitations, $\lambda = 1$, one finds contributions from $\mathrm{s_{1/2}}$, $\mathrm{d_{3/2}}$ and $\mathrm{d_{5/2}}$-waves. They are all E1 $2^+ \rightarrow$ continuum transitions.
Condition 2.30 gives us electric quadrupole, E2, $\mathrm{p_{3/2}}$-wave, resonant at 1^+ and 3^+ states, and $\mathrm{p_{1/2}}$, $\mathrm{f_{5/2}}$ and $\mathrm{f_{7/2}}$-waves coupling $2^+ \rightarrow$ continuum. The energy-levels scheme with possible gamma transitions is shown in Fig. 2.4. It is an interpretation of the respective cross-sections. Plots of angular and energetic spectra of all the derived amplitudes and details concerning the respective two-body potentials can be found in [Ber98].

As it has been already pointed out in Chapter 1, for the astrophysical energy range only E1 is relevant (4 orders of magnitude larger than E2). The E1 s-wave dominates $S_{17}(0)$. The M1 resonance at $E_{REL} = 632$ keV must be taken into account in CD as its influence should be extracted from the data for the purpose of extrapolation towards $E_{REL} = 0$.

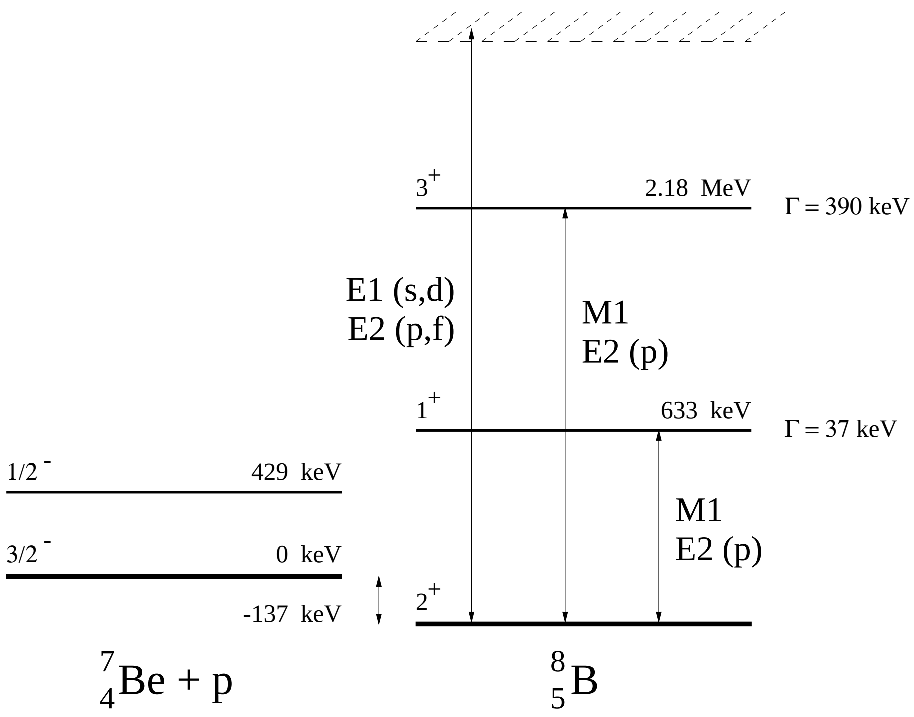

Figure 2.4: *Energy structure in ^{8}B and in the system $^{7}Be + p$ (see text for references). Relevant gamma transitions are sketched: E1 (s and d-waves), M1, and E2 (p, p-resonant $(1^{+}, 3^{+})$ and f-waves). The continuum of states is shown schematically at the top.*

2.2 Inverse reaction $^8\mathrm{B} \rightarrow ^7\mathrm{Be} + \mathrm{p}$

In Section 2.1.1 the cross-section for the collision of two charged particles at energies under Coulomb threshold has been introduced. Let us write it down for the radiative capture process $^7\mathrm{Be} + \mathrm{p} \rightarrow {}^8\mathrm{B} + \gamma$ explicitly

$$\begin{aligned}\sigma_{\mathrm{capt}}(\mathrm{E_{REL}}) =& \frac{1}{\mathrm{E_{REL}}} \exp\left(-2\pi\eta\right) \mathrm{S_{17}}(\mathrm{E_{REL}}) \\ =& \frac{1}{\mathrm{E_{REL}}} \exp\left(-\frac{\mathrm{c}}{\sqrt{\mathrm{E_{REL}}}}\right) \mathrm{S_{17}}(\mathrm{E_{REL}}) \end{aligned} \tag{2.31}$$

where the constant c is given by Eq. 2.16 and is numerically c=117.469 [keV$^{1/2}$]. One wants to study now an inverse reaction: the nuclear photoabsorption $^8\mathrm{B} + \gamma \rightarrow {}^7\mathrm{Be} + \mathrm{p}$. One knows from the detailed balance theorem that the two cross-sections are coupled by pure geometrical factors: the phase-space available and the density of final states i.e. the number of projections of angular momentum vectors

$$\sigma_\gamma = \sigma_{\mathrm{capt}} \frac{(2\mathrm{I_{Be}}+1)(2\mathrm{I_p}+1)}{2\,(2\mathrm{I_B}+1)} \frac{\mathrm{k}^2}{\mathrm{k}_\gamma^2} \tag{2.32}$$

The spin part yields 8/10 ($\mathrm{I_{Be}} = \frac{3}{2}$, $\mathrm{I_p} = \frac{1}{2}$, $\mathrm{I_B} = 2$) and the size of the phase-space is, respectively

$$\begin{aligned}\mathrm{k}^2 &= \frac{2\,\mu_{\mathrm{pBe}}\,\mathrm{E_{REL}}}{\hbar^2} \\ \mathrm{k}_\gamma^2 &= \left(\frac{\mathrm{E}_\gamma}{\hbar \mathrm{c}}\right)^2 = \frac{(\mathrm{E_{REL}}+\mathrm{Q})^2}{(\hbar \mathrm{c})^2}\end{aligned} \tag{2.33}$$

The Q-value of the capture process is 137 keV, and the reduced mass μ_{pBe}=820474.85 keV. From Eq. 2.32 we see clearly that the inverse process is amplified by a factor of about 10^3.
Finally

$$\sigma_\gamma = \sigma_{\mathrm{capt}} \frac{8}{5} \frac{\mu_{\mathrm{pBe}}\,\mathrm{E_{REL}}}{(\mathrm{E_{REL}}+\mathrm{Q})^2} = \frac{8}{5} \frac{\mu_{\mathrm{pBe}}}{(\mathrm{E_{REL}}+\mathrm{Q})^2}\, \mathrm{S_{17}}\, \mathrm{e}^{-\frac{\mathrm{c}}{\sqrt{\mathrm{E_{REL}}}}} \tag{2.34}$$

A photonuclear reaction with real photons would not be, however, experimentally feasible. The Coulomb field of a large-Z target is a very efficient source of equivalent (virtual) photons produced when a fast projectile passes by. Therefore the Coulomb dissociation method works very well for studying photo-disintegration processes which has been already demonstrated (Ref.[11],[12] in [Ber95]). A nuclear transition induced electromagnetically by a passage of a charged particle requires however additional attention. Since a Coulomb-scattered projectile is peaked mostly in the forward direction, the process must be peripheral and the fields generating the transition are source-free (see Section 2.3 in this chapter). The resulting transition matrix elements, in the first-order perturbation theory, are then the same as for the photoabsorption. Thus, the Coulomb dissociation cross-section is the photoprocess cross-section folded with spectra of virtual photons of various multipolarities [Ber95]. This acts as the second amplification of the cross-section (after the phase-space factor) in comparison with the radiative capture reaction $^7\mathrm{Be} + \mathrm{p} \rightarrow {}^8\mathrm{B}$. Therefore

$$\sigma_{\mathrm{CD}} = \sum_{\pi \mathrm{l}} \sigma_{\gamma}^{\pi \mathrm{l}} \times \mathrm{n}_{\pi \mathrm{l}} \tag{2.35}$$

In the experiment a number of break-up events in a given energy and angular interval i.e. the double differential cross-section is measured [Ber85]

$$\begin{aligned}\frac{\mathrm{d}^2\sigma_{\mathrm{CD}}}{\mathrm{d}\Omega \mathrm{d}\mathrm{E}_\gamma} &= \sum_{\pi \mathrm{l}} \sigma_{\gamma}^{\pi \mathrm{l}}(\mathrm{E}_\gamma) \frac{1}{\mathrm{E}_\gamma} \frac{\mathrm{d}\mathrm{n}_{\pi \mathrm{l}}}{\mathrm{d}\Omega}(\mathrm{E}_\gamma) \\ &= \frac{8}{5} \frac{\mu_{\mathrm{pBe}}}{(\mathrm{E}_{\mathrm{REL}} + \mathrm{Q})^3}\, \mathrm{e}^{-\frac{\mathrm{c}}{\sqrt{\mathrm{E}_{\mathrm{REL}}}}} \sum_{\pi \mathrm{l}} \frac{\mathrm{n}_{\pi \mathrm{l}}}{\mathrm{d}\Omega}(\mathrm{E}_{\mathrm{REL}}+\mathrm{Q})\ \mathrm{S}_{17}^{\pi \mathrm{l}}(\mathrm{E}_{\mathrm{REL}})\end{aligned} \tag{2.36}$$

In the next section a quantitative information on the equivalent photon fluxes of a given multipolarity is given. For the dominant dipole E1, resonant M1 (at $\mathrm{E}_{\mathrm{REL}} = 632$ keV), and weak E2 excitations these functions are derived explicitly. According to Eq. 2.36 the Coulomb dissociation of ^{8}B can be simulated. As the input one assumes energy dependences of the S-factors for the relevant transitions.

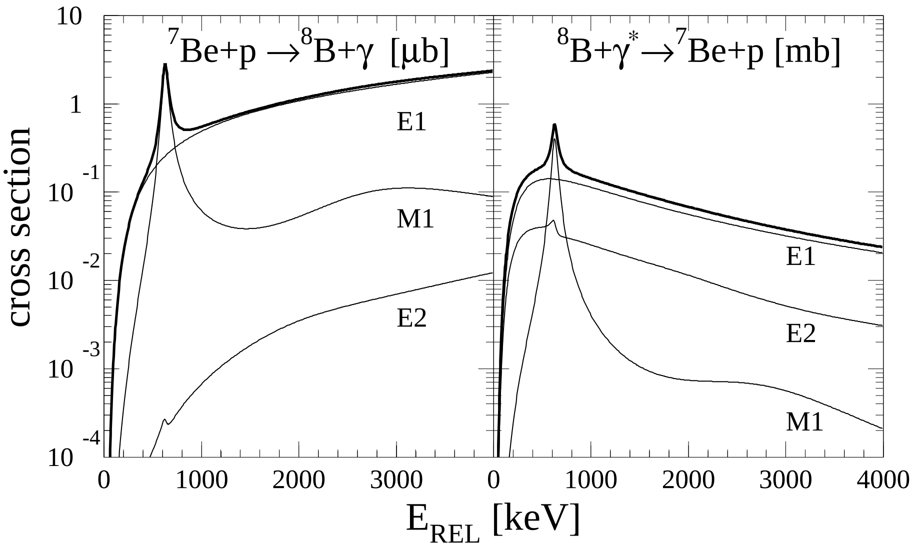

Figure 2.5: *Contribution of the relevant transitions to the direct-capture and the Coulomb-dissociation cross-section. Note the magnitude of the inverse processes.*

2.3 Coulomb break-up

2.3.1 Classification of the motion in the Coulomb field

Electromagnetic interaction between two charged nuclei is a useful tool, especially in collisions of heavy ions, for the excitation of one or both of the partners. To see how the nucleus responds to the interaction, one constructs the adiabaticity parameter [Ale89] which compares the transition time between the initial and the excited state in the nucleus $t_{fi} = \hbar/(E_f - E_i) = \hbar/E_\gamma$, and the collision time which is of the order of $R/(\gamma v)$ where: R-the sum of the nuclear radii, v-projectile velocity and γ-the Lorentz factor (account on the relativistic contraction)

$$\xi = \frac{E_\gamma R}{\hbar \gamma v} \tag{2.37}$$

Eq. 2.37 in case of the $^8B + ^{208}Pb$ collision at $E_{LAB} = 254$ MeV/u yields $\xi = 0.06 < 1$. This means that the ^8B nucleus does not respond adiabatically to the interaction but can be easily excited in the Coulomb field of lead.
In Eq. 2.12 the Sommerfeld parameter for the system $^7Be + p$ is defined. Now it is used to measure the strength of the Coulomb field in modifying the trajectory of ^8B

$$\eta = \frac{Z_{Pb} Z_B e^2}{\hbar v} \tag{2.38}$$

Eq. 2.38 can be expressed in terms of half the distance of closest approach in a head-on collision a and the wavelength of the relative motion $\lambdabar$

$$a = \frac{Z_{Pb} Z_B e^2}{\gamma \mu v^2} \qquad \lambdabar = \frac{\hbar}{\mu v} \tag{2.39}$$

where $\mu = \frac{m_B m_{Pb}}{m_B + m_{Pb}}$ is the reduced mass.
One has now a qualitative picture of the interaction strength

$$\eta = \frac{a\gamma}{\lambdabar} \tag{2.40}$$

Substituting the numerical values one gets $\eta \approx 4.8$. This result of $\eta \gg 1$ is a typical situation of sufficiently strong repulsive Coulomb force to keep the projectile off the range of the nuclear interaction [Ald75]. The projectile may be thus considered to move along a classical (not quantal) trajectory. This simplifies the problem considerably because the Coulomb excitation can be described as a classical Kepler problem for a repulsive Coulomb force. The electromagnetic field which determines this trajectory may be treated as a small perturbation that excites the ^8B nucleus and causes its break-up. Thus the first-order time-dependent perturbation theory can be used to obtain the respective nuclear transitions.

Moreover, the projectile energy 254 MeV/u ($\beta = 0.62$) in the system of heavy ions is large enough to treat trajectory of this motion with a very high accuracy as a straight line. Description of such relativistic Coulomb excitation goes beyond the classical Weizsäker-Williams method [Jac75] but the qualitative idea is principally the same, extended now to various multipolarities.

With the above conclusions the strategy to describe the Coulomb excitation under circumstances relevant to our break-up reaction is as follows: the basic theory is formulated in the straight-line approximation analytically, then a small correction due to a Kepler trajectory is given; at the end a correction accounting on influence of the nuclear force is applied. Only such picture is ready to account for all the effects: retardation due to the relativistic motion, Coulomb recoil, and strong absorption of the nuclear potential.

2.3.2 Straight-line approximation

Let us consider a break-up reaction

$$\mathrm{c} + \mathrm{X} \longrightarrow \mathrm{a} + \mathrm{b} + \mathrm{X} \tag{2.41}$$

where a fast projectile $^{8}\mathrm{B}$ (c) is dissociated in the Coulomb field of a heavy target $^{208}\mathrm{Pb}$ (X) into $^{7}\mathrm{Be}$ and proton (a, b) (excitation of lead is roughly $5^2/82^2$ less probable). The double differential cross-section of this process

$$\frac{\mathrm{d}^2\sigma_{\mathrm{i}\to\mathrm{f}}}{\mathrm{dE}\,\mathrm{d}\Omega} = \left(\frac{\mathrm{d}\sigma}{\mathrm{d}\Omega}\right)_{\mathrm{R}} \mathrm{P}_{\mathrm{fi}} \tag{2.42}$$

can be factorized in the semiclassical theory into the Rutherford elastic scattering cross-section

$$\left(\frac{\mathrm{d}\sigma}{\mathrm{d}\Omega}\right)_{\mathrm{R}} = \frac{\mathrm{a}^2}{4}\left(\sin\frac{\vartheta}{2}\right)^{-4} \tag{2.43}$$

where a is given by Eq. 2.39 and is related to the collision parameter $\mathrm{b} = \mathrm{a}\cot\frac{\vartheta}{2}$ through the deflection angle ϑ,
and

$$\mathrm{P}_{\mathrm{fi}} = |\mathrm{a}_{\mathrm{fi}}|^2 \tag{2.44}$$

the probability for exciting a nuclear state from an initial state.
In the first-order perturbation theory the transition amplitude is

$$\mathrm{a}^1_{\mathrm{fi}} = \frac{1}{\mathrm{i}\hbar}\int_{-\infty}^{+\infty} \mathrm{dt}\, \mathrm{e}^{\mathrm{i}(\mathrm{E_f}-\mathrm{E_i})\mathrm{t}/\hbar}\, \langle \mathrm{I_f M_f} \mid \mathrm{V}[\mathrm{r(t)}] \mid \mathrm{I_i M_i}\rangle \tag{2.45}$$

where the Hamiltonian of the interaction is

$$\mathrm{V}[\mathbf{r}(\mathrm{t})] = \frac{1}{\mathrm{c}} \int \mathrm{d}^3\mathrm{r}\ \mathrm{A}_\mu[\mathrm{r}(\mathrm{t})]\ \mathrm{j}_\mu(\mathrm{r}) \tag{2.46}$$

Here the following notation for the four-current is used (vectors are in bold face)

$$\mathrm{j}_\mu \equiv \left(\rho(\mathbf{r}), \frac{\mathbf{j}(\mathbf{r})}{\mathrm{c}}\right) \tag{2.47}$$

$$\rho \equiv \rho_{\mathrm{fi}} = \phi_{\mathrm{i}}\phi_{\mathrm{f}}^* \qquad \mathbf{j} \equiv \mathbf{j}_{\mathrm{fi}} = \frac{\hbar}{2\mathrm{im}}[\phi_{\mathrm{i}}^*\nabla\phi_{\mathrm{f}} - \phi_{\mathrm{f}}\nabla\phi_{\mathrm{i}}^*]$$

(ϕ denotes the respective wave function)
and the four-potential

$$\mathrm{A}_\mu \equiv (\Phi(\mathbf{r},\mathrm{t}), \mathbf{A}(\mathbf{r},\mathrm{t})) = (1, \boldsymbol{\beta})\ \Phi(\mathbf{r},\mathrm{t}) \tag{2.48}$$

In a non-relativistic case (Fig. 2.6) the potential $\Phi(\mathbf{r},\mathrm{t})$ can be expressed

$$\Phi(\mathbf{r},\mathrm{t}) = \frac{\mathrm{Z_X e}}{|\mathbf{r} - \mathbf{R}(\mathrm{t})|} = \frac{\mathrm{Z_X e}}{\sqrt{(\mathrm{x}-\mathrm{b})^2 + \mathrm{y}^2 + (\mathrm{z} - \mathrm{vt})^2}} \tag{2.49}$$

Relativistic motion causes retardation effects and the Lienard-Wiechert potential must be applied

$$\Phi(\mathbf{r},\mathrm{t}) = \left.\frac{\mathrm{Z_X e}}{(1 - \boldsymbol{\beta}\cdot\hat{\mathrm{n}})\mathrm{R}}\right|_{\mathrm{ret}} \tag{2.50}$$

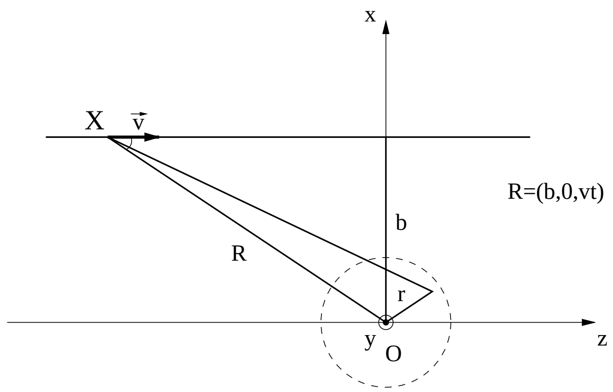

Figure 2.6: *Straight-line approximation. In the coordinate system chosen the heavier ion (lead) flies relativistically along the z-axis past the lighter one (^8B), which is at rest, and excites it.*

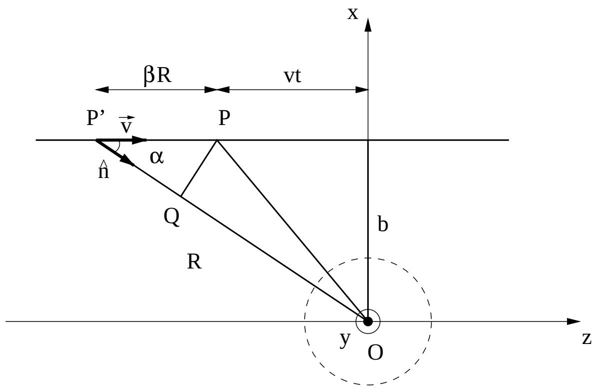

Figure 2.7: *Relativistic motion reveals delay in propagation of the interaction. P (P') is the present (retarded) point.*

where (see Fig. 2.7)

$$\boldsymbol{\beta} = \frac{\dot{\mathbf{R}}(\mathrm{t}')}{\mathrm{c}} \qquad \hat{\mathrm{n}} = \frac{\mathbf{R}}{\mathrm{R}} \qquad \mathrm{t}' = \mathrm{t} - \frac{|\mathrm{OP} - \mathrm{R}(\mathrm{t})|}{\mathrm{c}} \tag{2.51}$$

Simple geometry ($\mathrm{P'Q} = \beta \mathrm{R}\cos\alpha = \boldsymbol{\beta}\cdot\hat{\mathrm{n}}\mathrm{R}$, $\mathrm{OQ} = (1-\boldsymbol{\beta}\cdot\hat{\mathrm{n}})\mathrm{R}$, $\mathrm{b} = \mathrm{R}\sin\alpha$) yields

$$\begin{aligned}[(1-\boldsymbol{\beta}\hat{\mathrm{n}})\mathrm{R}]^2 = \mathrm{OP}^2 - \mathrm{PQ}^2 &= \mathrm{OP}^2 - \beta^2\mathrm{R}^2\sin^2\alpha = \mathrm{OP}^2 - \beta^2\mathrm{b}^2 \\ &= \mathrm{b}^2 + \mathrm{v}^2\mathrm{t}^2 - \beta^2\mathrm{b}^2 = \frac{\mathrm{b}^2}{\gamma^2} + \mathrm{v}^2\mathrm{t}^2 \end{aligned} \tag{2.52}$$

Finally, at a given point $\mathbf{r}$

$$\Phi(\mathbf{r},\mathrm{t}) = \frac{\mathrm{Z_X e}\gamma}{[(\mathrm{x}-\mathrm{b})^2 + \mathrm{y}^2 + \gamma^2(\mathrm{z}-\mathrm{vt})^2]^{1/2}} \tag{2.53}$$

and to calculate is

$$\mathrm{V}(\omega) = \int \mathrm{d}^3\mathrm{r}\left[\rho(\mathbf{r}) - \frac{1}{\mathrm{c}}\boldsymbol{\beta}\mathbf{j}(\mathbf{r})\right]\int \mathrm{dt}\, \mathrm{e}^{\mathrm{i}\omega\mathrm{t}}\Phi(\mathbf{r},\mathrm{t}) \tag{2.54}$$

Assuming the internal coordinate $\mathbf{r}$ to be much smaller in magnitude than $\mathbf{R}(\mathrm{t})$ this problem has been solved by Bertulani (in e.g. [Ber96d]) by approximating $\phi(\mathbf{r},\mathrm{t})$ in lower orders of $|\mathbf{r}|/\mathbf{R}(\mathrm{t})$ (dipole, quadrupole excitation). Here is followed the pioneering idea of Winther and Alder [Win79] who evaluated the excitation amplitude in the first order time-dependent perturbation theory for all multipolarities. Their article marks only main stages of calculation, therefore a detailed evaluation presented here has a didactic purpose.

Since time-dependence occurs only in $\Phi(\mathbf{r},t)$ one introduces the potential in the frequency domain. Through the Fourier transform

$$f(y) = \int_{-\infty}^{+\infty} e^{ixy}\, F(x)\, dx$$
$$F(x) = \frac{1}{(x^2+q^2)^{r+\frac{1}{2}}} \qquad f(y) = 2\left(\frac{|y|}{2q}\right)^r \frac{\Gamma(\frac{1}{2})}{\Gamma(r+\frac{1}{2})}\, K_r(q|y|) \tag{2.55}$$

one gets

$$\int dt\, e^{i\omega t}\Phi(\mathbf{r},t) = \frac{2Z_X e}{v}\, e^{i\omega\frac{z}{v}}\, K_0\left(\frac{\omega}{\gamma v}\sqrt{(x-b)^2+y^2}\right) \tag{2.56}$$

Using the Graf summation theorem for the Bessel functions (Eq.9.1.79 in [Abr72]) the latter can be expressed in the coordinates of Fig. 2.8

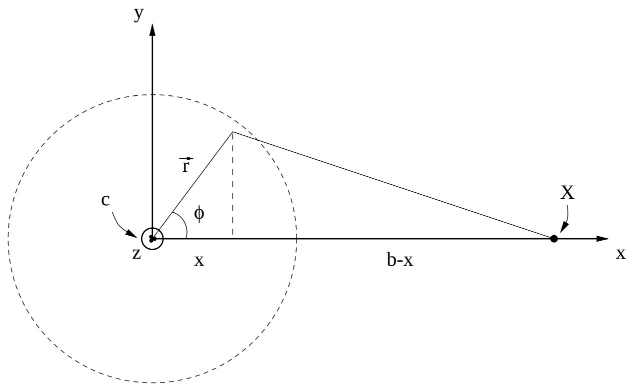

Figure 2.8: *Graf summation theorem for the Bessel functions of integer order.*

$$K_0\left(\frac{\omega}{\gamma v}\sqrt{(x-b)^2+y^2}\right) = \sum_{n=-\infty}^{+\infty} e^{in\phi}\, K_n\left(\frac{\omega b}{\gamma v}\right) I_n\left(\frac{\omega}{\gamma v}\sqrt{r^2-z^2}\right) \tag{2.57}$$

where I_n are the Bessel functions of order n.
Since a solution of the problem in a representation using the multipole moments is expected one puts

$$\Phi(\mathbf{r},\omega) = \sum_{l,m} W_{lm}(r,\omega)\, Y^*_{lm}(\hat{r}) \tag{2.58}$$

where

$$\begin{aligned}
W_{lm}(r,\omega) &= \int d\Omega\, \Phi(\mathbf{r},\omega)\, Y_{lm}(\hat{r}) = \frac{2Z_X e}{v} \sum_{n=-\infty}^{+\infty} K_n\left(\frac{\omega b}{\gamma v}\right) \\
&\times \int_0^\pi \sin\theta d\theta\, e^{i\frac{\omega}{v} r\cos\theta}\, Y_{lm}(\theta,0)\, I_n\left(\frac{\omega r}{\gamma v}\sin\theta\right) \underbrace{\int_0^{2\pi} d\phi\, e^{i(m+n)\phi}}_{\neq 0 \to n=-m} \\
&= \frac{4\pi Z_X e}{v} K_m\left(\frac{\omega b}{\gamma v}\right) \int_0^\pi \sin\theta d\theta\, e^{i\frac{\omega}{v} r\cos\theta}\, Y_{lm}(\theta,0)\, I_m\left(\frac{\omega r}{\gamma v}\sin\theta\right) \qquad (2.59)
\end{aligned}$$

Integration over ϕ is performed using the fact that $K_{-m}(x) = K_m(x)$ and $I_{-m}(x) = I_m(x)$. The integral over θ can be solved by introducing the Gegenbauer polynomials $C_m^n(x)$

$$\begin{aligned}
Y_{lm}(\theta,0) &= (-)^m \sqrt{\frac{2l+1}{4\pi}} \left(\frac{(l-m)!}{(l+m)!}\right)^{1/2} P_{lm}(\cos\theta) \\
P_{lm}(x) &= (2m-1)!!\, (1-x^2)^{m/2}\, C_{l-m}^{m+1/2}(x) \qquad (2.60)
\end{aligned}$$

In terms of the cylindrical Bessel functions $i^{-m} J_m(ix) = I_m(x)$ one gets

$$\begin{aligned}
W_{lm}(r,\omega) &= \frac{4\pi Z_X e}{v} K_m\left(\frac{\omega b}{\gamma v}\right) \sqrt{\frac{2l+1}{4\pi}} \left(\frac{(l-m)!}{(l+m)!}\right)^{1/2} i^m\, (2m-1)!! \\
&\times \int_0^\pi \sin^{m+1}\theta\, d\theta\, e^{i\frac{\omega}{v} r\cos\theta} C_{l-m}^{m+1/2}(\cos\theta)\, J_m\left(\frac{i\omega r}{\gamma v}\sin\theta\right) \qquad (2.61)
\end{aligned}$$

But the above integral is known as the Gegenbauer integral (Eq.7.333 in [Gra88]) and it reads

$$\begin{aligned}
\int_0^\pi \sin^{m+1}\theta\, d\theta\, e^{i\frac{\omega}{v} r\cos\theta} C_{l-m}^{m+1/2}(\cos\theta)\, J_m\left(\frac{i\omega r}{\gamma v}\sin\theta\right) &= \\
= i^{l-m}\left(\frac{ic}{\gamma v}\right)^m C_{l-m}^{m+1/2}\left(\frac{c}{v}\right) j_l\left(\frac{\omega r}{c}\right) & \qquad (2.62)
\end{aligned}$$

where the spherical Bessel functions $j_n(x) = \sqrt{\frac{\pi}{2x}} J_{n+1/2}(x)$ are introduced. Finally

$$\begin{aligned}
W_{lm}(r,\omega) &= \sqrt{16\pi(2l+1)}\, \frac{Z_X e}{v} \sqrt{\frac{(l-m)!}{(l+m)!}}\, (2m-1)!!\, i^{l+m} \left(\frac{c}{\gamma v}\right)^m \\
&\times\ K_m\left(\frac{\omega b}{\gamma v}\right) C_{l-m}^{m+1/2}\left(\frac{c}{v}\right) j_l\left(\frac{\omega r}{c}\right) \qquad m \geq 0 \quad (2.63) \\
W_{l,-m}(r,\omega) &= (-)^m W_{lm}(r,\omega) \qquad m < 0
\end{aligned}$$

Now let us pay attention to the four-current under the integral 2.54. Using the time evolution of the Schrödinger equation $\rho(\mathrm{r},\mathrm{t}) = \rho(\mathrm{r},0)\mathrm{e}^{\mathrm{i}\omega\mathrm{t}}$ one calculates the continuity relation

$$0 = \frac{\partial \mathrm{j}_\mu}{\partial \mathrm{x}_\mu} \equiv \boldsymbol{\nabla}\mathbf{j} + \frac{\partial}{\partial \mathrm{t}}\rho = \boldsymbol{\nabla}\mathbf{j} + \mathrm{i}\omega\rho \tag{2.64}$$

Integration by parts yields

$$\int \mathrm{d}^3\mathrm{r}\, \frac{\boldsymbol{\nabla}\mathbf{j}}{-\mathrm{i}\omega} = \underbrace{\frac{\mathbf{j}}{-i\omega}\bigg|_\tau}_{=0} - \int \mathrm{d}^3\mathrm{r}\, \frac{\mathbf{j}\boldsymbol{\nabla}}{-\mathrm{i}\omega} = \int \mathrm{d}^3\mathrm{r}\, \frac{\mathbf{j}\boldsymbol{\nabla}}{\mathrm{i}\omega} \tag{2.65}$$

So finally

$$\mathrm{V}(\omega) = \sum_{\mathrm{l,m}} \int \mathrm{d}^3\mathrm{r}\, \mathbf{j}(\mathbf{r}) \underbrace{\left[\frac{\boldsymbol{\nabla}}{\mathrm{i}\omega} - \frac{\mathbf{v}}{\mathrm{c}^2}\right] \mathrm{W}_{\mathrm{lm}}(\mathrm{r},\omega)\, \mathrm{Y}^*_{\mathrm{lm}}(\hat{\mathrm{r}})}_{\mathbf{A}(\mathbf{r},\omega)} \tag{2.66}$$

The potential is now in the frequency domain and one can take advantage of the nature of the electromagnetic field in the absence of sources (see e.g. [Eis70]). In the transverse gauge one has $\boldsymbol{\nabla}\cdot\mathbf{A}(\mathbf{r},\mathrm{t}) = 0$ where $\mathbf{A}(\mathbf{r},t)$ is the vector potential. It means, that its Fourier transform obeys the Helmholtz equation

$$(\boldsymbol{\nabla}^2 + \mathrm{k}^2)\mathbf{A}_{\mathrm{l}\lambda\mathrm{m}}(\mathbf{r},\omega) = 0 \tag{2.67}$$

In problems having spherical symmetry its basic solution has the form

$$\mathbf{A}_{\mathrm{l}\lambda\mathrm{m}}(\mathbf{r},\omega) = \mathrm{j}_\lambda(\mathrm{kr})\mathbf{Y}_{\mathrm{l}\lambda\mathrm{m}}(\hat{\mathrm{r}}) \qquad \mathrm{k} = \frac{\omega}{\mathrm{c}} \tag{2.68}$$
$$|l-1| \leq \lambda \leq l+1$$

where the spherical polynomials can be transformed to the spherical harmonics using the Clebsch-Gordan coefficients

$$\mathbf{Y}_{\mathrm{l}\lambda\mathrm{m}}(\hat{\mathbf{r}}) = \sum_{\mathrm{m}\mu} < \lambda\mathrm{m}1\mu|\mathrm{lm} > \mathrm{Y}_{\lambda\mathrm{m}}(\hat{\mathrm{r}})\epsilon_\mu \tag{2.69}$$
$$\epsilon_{\pm1} = \mp\frac{1}{\sqrt{2}}(\mathrm{e_x} \pm \mathrm{ie_y}) \qquad \epsilon_0 = \mathrm{e_z}$$

For a given l these solutions form irreducible tensors of rank l. From the condition of triangle in Eq. 2.68, the case $\mathrm{l} = 0 \rightarrow \lambda{=}1$ is not interesting since this does not satisfy the transverse gauge (it will be seen explicitly in the proceeding formulae).

In constructing a solution for the remaining cases $\lambda = \mathrm{l}-1$, $\lambda = \mathrm{l}$, $\lambda = \mathrm{l}+1$ one must take into account that a given solution should have a definite parity as the potentials carry definite angular momentum (strong interaction is invariant under an inversion of all three spatial axes). Due to the spherical polynomials the solutions of $\lambda = \mathrm{l} \pm 1$ have the same parity, opposite to the parity of $\lambda = \mathrm{l}$, therefore the solutions are constructed in the form

$$\begin{aligned} \mathbf{A}^{\mathcal{M}}_{\mathrm{lm}}(\mathbf{r}) &= \mathrm{j_l(kr)}\mathbf{Y}_{\mathrm{llm}}(\hat{\mathrm{r}}) \\ \mathbf{A}^{\mathcal{E}}_{\mathrm{lm}}(\mathbf{r}) &= \mathrm{c_{l-1}j_{l-1}(kr)}\mathbf{Y}_{\mathrm{l,l-1,m}}(\hat{\mathrm{r}}) + \mathrm{c_{l+1}j_{l+1}(kr)}\mathbf{Y}_{\mathrm{l,l+1,m}}(\hat{\mathrm{r}}) \end{aligned} \tag{2.70}$$

where the potential $\mathbf{A}^{\mathcal{M}}_{\mathrm{lm}}$ has parity $(-)^{\mathrm{l}}$ and the potential $\mathbf{A}^{\mathcal{E}}_{\mathrm{lm}}$ has parity $(-)^{\mathrm{l}+1}$. The constants $\mathrm{c_{l\pm1}}$ are to be determined from the gauge condition.
Using the symmetry and orthogonality relations for the Clebsch-Gordan coefficients, one obtains [Eis70]

$$\begin{aligned} \boldsymbol{\nabla}\cdot\mathbf{A}^{\mathcal{M}}_{\mathrm{lm}}(\mathbf{r}) &= \boldsymbol{\nabla}\cdot(\mathrm{j}_\lambda(\mathrm{kr})\mathbf{Y}_{\mathrm{l\lambda m}}(\hat{\mathrm{r}})) \\ &= -\mathrm{kj_l(kr)Y_{lm}}(\hat{\mathrm{r}})\left[\left(\frac{\mathrm{l}+1}{2\mathrm{l}+1}\right)^{1/2}\delta_{\lambda-1,\mathrm{l}} + \left(\frac{\mathrm{l}}{2\mathrm{l}+1}\right)^{1/2}\delta_{\lambda+1,\mathrm{l}}\right] \end{aligned} \tag{2.71}$$

$$\boldsymbol{\nabla}\cdot\mathbf{A}^{\mathcal{E}}_{\mathrm{lm}}(\mathbf{r}) = -\mathrm{kj_l(kr)Y_{lm}}(\hat{\mathrm{r}})\left[\left(\frac{\mathrm{l}+1}{2\mathrm{l}+1}\right)^{1/2}\mathrm{c_{l+1}} + \left(\frac{\mathrm{l}}{2\mathrm{l}+1}\right)^{1/2}\mathrm{c_{l-1}}\right] \tag{2.72}$$

In case of $\mathbf{A}^{\mathcal{M}}_{\mathrm{lm}}$ one has $\lambda = \mathrm{l}$ and the right-hand side of Eq. 2.71 vanishes. For the $\mathbf{A}^{\mathcal{E}}_{\mathrm{lm}}$ one gets a transverse potential if

$$\mathrm{c_{l-1}} = \left(\frac{\mathrm{l}+1}{2\mathrm{l}+1}\right)^{1/2} \qquad \mathrm{c_{l+1}} = -\left(\frac{\mathrm{l}}{2\mathrm{l}+1}\right)^{1/2} \tag{2.73}$$

Hence

$$\mathbf{A}^{\mathcal{E}}_{\mathrm{lm}}(\mathbf{r}) = \left(\frac{\mathrm{l}+1}{2\mathrm{l}+1}\right)^{1/2}\mathrm{j_{l-1}(kr)}\mathbf{Y}_{\mathrm{l,l-1,m}}(\hat{\mathrm{r}}) - \left(\frac{\mathrm{l}}{2\mathrm{l}+1}\right)^{1/2}\mathrm{j_{l+1}(kr)}\mathbf{Y}_{\mathrm{l,l+1,m}}(\hat{\mathrm{r}}) \tag{2.74}$$

Expression 2.74 can be rewritten in terms of the orbital angular momentum operator $\mathbf{L} = -\mathrm{i}\mathbf{r}\times\boldsymbol{\nabla} = \mathrm{i}\boldsymbol{\nabla}\cdot\mathbf{r}\times$ acting on a function. Since

$$\mathbf{Y}_{\mathrm{l\lambda m}}(\hat{\mathrm{r}}) = \begin{cases} \frac{-\mathrm{i}}{\sqrt{\mathrm{l(l+1)}}}(\mathbf{r}\times\boldsymbol{\nabla})\mathrm{Y_{lm}} & \lambda = \mathrm{l} \\ \frac{1}{\sqrt{\mathrm{l(2l+1)}}}(\mathbf{r}\cdot\boldsymbol{\nabla} + \mathrm{l}\hat{\mathbf{r}})\mathrm{Y_{lm}} & \lambda = \mathrm{l}-1 \\ \frac{1}{\sqrt{\mathrm{(l+1)(2l+1)}}}(\mathbf{r}\cdot\boldsymbol{\nabla} - (\mathrm{l}+1)\hat{\mathbf{r}})\mathrm{Y_{lm}} & \lambda = \mathrm{l}+1 \end{cases} \tag{2.75}$$

the well known standard form can be achieved

$$\mathbf{A}^{\mathcal{M}}_{\mathrm{lm}}(\mathbf{r}) = \frac{1}{\sqrt{\mathrm{l}(\mathrm{l}+1)}}\mathbf{L}\mathrm{j_l}(\mathrm{kr})\mathrm{Y_{lm}}(\hat{\mathrm{r}}) \tag{2.76}$$

$$\mathbf{A}^{\mathcal{E}}_{\mathrm{lm}}(\mathbf{r}) = \frac{-\mathrm{i}}{\mathrm{k}\sqrt{\mathrm{l}(\mathrm{l}+1)}}\boldsymbol{\nabla}\times(\mathbf{L}\mathrm{j_l}(\mathrm{kr})\mathrm{Y_{lm}}(\hat{\mathrm{r}})) \tag{2.77}$$

In case of the electric potential one should use the functions with indices $\mathrm{l}\pm 1$ so it is convenient to rewrite the Gegenbauer polynomials using the following recursion formula (Eq.8.933 in [Gra88])

$$\begin{aligned}\mathrm{C}^{\mathrm{m}+1/2}_{\mathrm{l-m}}(\mathrm{x}) &= \frac{\mathrm{l}+\mathrm{m}}{(2\mathrm{l}+1)\mathrm{x}}\mathrm{C}^{\mathrm{m}+1/2}_{\mathrm{l-m-1}}(\mathrm{x}) + \frac{\mathrm{l}-\mathrm{m}+1}{(2\mathrm{l}+1)\mathrm{x}}\mathrm{C}^{\mathrm{m}+1/2}_{\mathrm{l-m+1}}(\mathrm{x}) \\ &= \frac{1}{(2\mathrm{m}-1)!!}(1-\mathrm{x}^2)^{-\mathrm{m}/2}\left[\frac{\mathrm{l}+\mathrm{m}}{(2\mathrm{l}+1)\mathrm{x}}\mathrm{P}^{\mathrm{m}}_{\mathrm{l}-1}(\mathrm{x}) + \frac{\mathrm{l}-\mathrm{m}+1}{(2\mathrm{l}+1)\mathrm{x}}\mathrm{P}^{\mathrm{m}}_{\mathrm{l}+1}(\mathrm{x})\right]\end{aligned} \tag{2.78}$$

Finally

$$\mathrm{V}(\omega) = \mathrm{Z_X e}\sum_{\pi\mathrm{lm}}\frac{4\pi}{2\mathrm{l}+1}(-)^{\mathrm{m}}\mathcal{M}(\pi\mathrm{l},-\mathrm{m})\,\mathrm{S}_{\pi\mathrm{lm}} \tag{2.79}$$

where the multipole matrix elements depend only on properties of the nuclear states, with $\mathrm{m} = \mathrm{M_f} - \mathrm{M_i}$ being the angular momentum transfer to the internal degrees of freedom (excitation) [$\mathrm{M_i}$, $\mathrm{M_f}$ denote initial and final states]

$$\begin{aligned}\mathcal{M}_{\mathrm{Elm}} &= \frac{(2\mathrm{l}+1)!!}{\mathrm{c}\left(\frac{\omega}{\mathrm{c}}\right)^{\mathrm{l}+1}(\mathrm{l}+1)}\int \mathrm{d^3r}\,\mathbf{j}(\mathbf{r})\cdot\boldsymbol{\nabla}\times\mathbf{L}\left(\mathrm{j_l}(\frac{\omega\mathrm{r}}{\mathrm{c}})\mathrm{Y_{lm}}(\hat{\mathrm{r}})\right) \\ \mathcal{M}_{\mathrm{Mlm}} &= -\mathrm{i}\frac{(2\mathrm{l}+1)!!}{\mathrm{c}\left(\frac{\omega}{\mathrm{c}}\right)^{\mathrm{l}+1}(\mathrm{l}+1)}\int \mathrm{d^3r}\,\mathbf{j}(\mathbf{r})\cdot\mathbf{L}\left(\mathrm{j_l}(\frac{\omega\mathrm{r}}{\mathrm{c}})\mathrm{Y_{lm}}(\hat{\mathrm{r}})\right)\end{aligned} \tag{2.80}$$

Excitation functions are

$$\mathrm{S}_{\pi\mathrm{lm}} = \frac{(2\mathrm{l}+1)^{3/2}}{4\pi\mathrm{v}\gamma}\mathrm{G}_{\pi\mathrm{lm}}\left(\frac{\mathrm{c}}{\mathrm{v}}\right)\left(\frac{\omega}{\mathrm{c}}\right)^{\mathrm{l}}\mathrm{K_m}(\xi) \tag{2.81}$$

where $\xi = \frac{\omega\mathrm{b}}{\gamma\mathrm{v}} = \frac{\mathrm{E}_\gamma\mathrm{b}}{\hbar\gamma\mathrm{v}}$ is the adiabaticity parameter defined first in Eq. 2.37 and $\mathrm{G}_{\pi\mathrm{lm}}$, rewritten in terms of the Legendre polynomials, read

$$\begin{aligned}\mathrm{G_{Elm}}(\mathrm{x}) &= \mathrm{i}^{\mathrm{l}+\mathrm{m}}\frac{\sqrt{16\pi}}{\mathrm{l}(2\mathrm{l}+1)!!}\sqrt{\frac{(\mathrm{l}-\mathrm{m})!}{(\mathrm{l}+\mathrm{m})!}}\left(\mathrm{x}^2-1\right)^{-1/2} \\ &\quad\times\left[\frac{(\mathrm{l}+1)(\mathrm{l}+\mathrm{m})}{2\mathrm{l}+1}\mathrm{P}^{\mathrm{m}}_{\mathrm{l}-1}(\mathrm{x}) - \frac{\mathrm{l}(\mathrm{l}-\mathrm{m}+1)}{2\mathrm{l}+1}\mathrm{P}^{\mathrm{m}}_{\mathrm{l}+1}(\mathrm{x})\right] \\ \mathrm{G_{Mlm}}(\mathrm{x}) &= \mathrm{i}^{\mathrm{l}+\mathrm{m}+1}\frac{\sqrt{16\pi}}{\mathrm{l}(2\mathrm{l}+1)!!}\sqrt{\frac{(\mathrm{l}-\mathrm{m})!}{(\mathrm{l}+\mathrm{m})!}}\left(\mathrm{x}^2-1\right)^{-1/2}\,\mathrm{m}\,\mathrm{P}^{\mathrm{m}}_{\mathrm{l}}(\mathrm{x})\end{aligned} \tag{2.82}$$

Functions $G_{\pi lm}$ have properties: $G_{El,-m}(x) = (-)^m G_{Elm}(x)$, $G_{Ml,-m}(x) = (-)^{m+1} G_{Mlm}(x)$.
$S_{\pi lm}$ is a kinematic part, which is independent of inner degrees of freedom of the excited nucleus. It describes the strength of the field measured by the velocity ($G_{\pi lm}(c/v)$), and the adiabaticity of the excitation ($K_m(\xi)$-modified Bessel functions).

The fact that the excitation amplitude in the first-order time-dependent perturbation theory [Win79, Ber88]

$$a^1_{fi} = \frac{Z_X e}{i\hbar} \sum_{\pi lm} \frac{4\pi}{2l+1} (-)^m \mathcal{M}(\pi l, -m)\, S_{\pi lm} \tag{2.83}$$

can be expressed as a product of two independent factors, namely the matrix element describing the electromagnetic decay of the nucleus and a parameterization of the trajectory of the motion in the Coulomb field, is of great importance. Different kinematic conditions than assumed here (straight-line approximation) cannot affect the internal degrees of freedom (matrix elements), therefore one can attribute them to modifications in the excitation functions $S_{\pi lm}$ only. At the collision energy of 254 MeV/u it is highly motivated to leave the excitation amplitude with the functions $S_{\pi lm}$ given by Eq. 2.81 however for the completeness of the description one must take into account modifications introduced by the hyperbolic orbit.

2.3.3 Correction on hyperbolic orbit

To consider the Rutherford bending of the trajectory a new formula for the functions $S_{\pi lm}$ must be derived. It is clear because the matrix elements $M_{\pi lm}$ describe the inner properties of the excited target and do not depend on a way the projectile moves. The hyperbolic orbit must reduce the magnitude of the excitation through an increase of the impact parameter. The impact parameter describes properly a straight-line trajectory whereas in this case it is better to speak about half the distance of closest approach in a head-on collision. To solve the issue one considers the classical one-body problem given by the relativistic Lagrangian [Lan76]

$$\mathcal{L} = -\mu c^2 \left[1 - \frac{1}{c^2}\left(\dot{r}^2 + r^2\dot{\phi}^2\right)\right]^{1/2} - \frac{Z_c Z_X e^2}{r} \tag{2.84}$$

Three solutions depending on the sign of the charges and the magnitude of the angular momentum L in the collision (see [Lan75] §39) are possible. In our case, for not too small impact parameters leading to strong interactions

$$Lc \gg |Z_c Z_X e^2| \tag{2.85}$$

The solution relating the collision angle ϕ and the distance r between the nuclei reads

$$\frac{1}{r} = A\left[\varepsilon\cos(\chi\phi) - 1\right] \tag{2.86}$$

where

$$\begin{aligned}
\chi &= \left[1 - \left(\frac{Z_c Z_X e^2}{Lc}\right)^2\right]^{1/2} \simeq 1 \\
A &= \frac{Z_c Z_X e^2 E}{L^2 c^2 \chi^2} \simeq \frac{a}{b^2} \\
\varepsilon &= \frac{Lc}{Z_c Z_X e^2 E}\left[E^2 - \mu^2 c^4 + \left(\frac{\mu c Z_c Z_X e^2}{L}\right)^2\right]^{1/2} = \sqrt{\frac{b^2}{a^2} + \frac{1}{\gamma^2}} \simeq \sqrt{\frac{b^2}{a^2} + 1}
\end{aligned} \tag{2.87}$$

The variables used are as follows: $E = \gamma\mu c^2$ -the total bombarding energy, $L = \gamma\mu v b$ -the angular momentum, $\mu = \frac{m_c m_X}{m_c + m_X}$ -the reduced mass, γ -the Lorentz factor, $a = \frac{Z_X Z_c e^2}{\gamma\mu v^2}$ -half the distance of closest approach in a head-on collision (one assumes point-like nuclei), b -the impact parameter related to the deflection angle ϑ by $b = a\cot\frac{\vartheta}{2}$. Approximations in 2.87 are very well justified in heavy-ion collisions [Ale89].
A parametric form ([Lan76] §15)

$$r(w) = a[\varepsilon\cosh w + 1] \qquad t(w) = \frac{a}{v}[\varepsilon\sinh w + w] \tag{2.88}$$

which fulfills the condition that in the closest approach $\mathrm{w} = \mathrm{t} = 0$, is an obvious description of motion on a hyperbola with eccentricity $\varepsilon = \sqrt{\frac{\mathrm{b}^2}{\mathrm{a}^2} + 1} = \frac{1}{\sin\vartheta/2}$.
Cartesian coordinates can be chosen conveniently along the conserved vectors: $\mathbf{L} = \mathbf{r} \times \mathbf{p}$ -the angular momentum vector and $\mathbf{A} = (\mathrm{Z_X Z_c e^2/v})\hat{\mathrm{r}} - \mathbf{L} \times \hat{\mathrm{p}}$ -the Pauli vector [Ald75] (see Fig. 2.9)

$$\mathbf{r} = \begin{pmatrix} \mathrm{a}(\cosh \mathrm{w} + \varepsilon) \\ \mathrm{a}\sqrt{\varepsilon^2 - 1}\sinh \mathrm{w} \\ 0 \end{pmatrix} \tag{2.89}$$

Now, unlike in Eq. 2.53, 2.54 being a special case of a straight-line motion, the retarded potential generated by following the Coulomb trajectory results from Eq. 2.50 and reads

$$\mathrm{V}(\omega, \mathbf{r}) = \mathrm{Z_X e} \int \mathrm{d}^3\mathrm{r} \left[\rho(\mathbf{r}) - \frac{1}{\mathrm{c}}\boldsymbol{\beta}\mathbf{j}(\mathbf{r})\right] \int \mathrm{dt}\, \mathrm{e}^{\mathrm{i}\omega\mathrm{t}} \frac{\exp(\mathrm{ik}|\mathbf{r} - \mathbf{R}(\mathrm{t})|)}{|\mathbf{r} - \mathbf{R}(\mathrm{t})|} \tag{2.90}$$

where $\mathbf{R}$ is the distance between the nuclei (see Fig. 2.6). To find the orbital integrals $\mathrm{S}_{\pi\mathrm{lm}}$ exp(ikr)/r in Eq. 2.90 is expanded into the spherical Hankel functions of the first kind [Ale89]. The calculation is then made with the exact form of the expansion which is however not very trivial mathematically but it is the only form for the intermediate-energy region [Ale89]. An educative approach is to consider a non-relativistic limit of the expansion and then to find a general solution by comparing it with the relativistic case. In the excellent book of Alder and

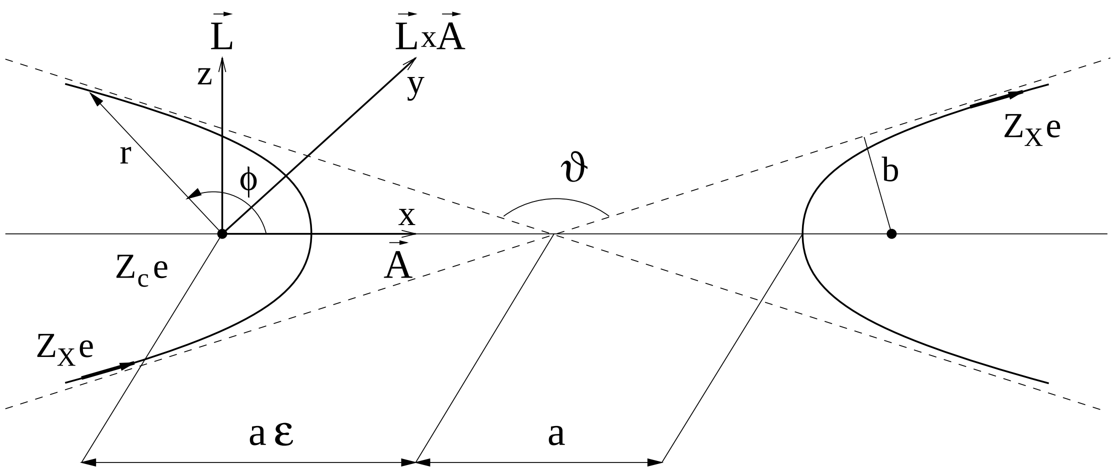

Figure 2.9: *Kepler's problem in the case of the attractive (left) and the repulsive force (right). The variables are explained in the text.*

Winther on electromagnetic excitation [Ald75] a well known form of the classical electric orbital integrals can be found

$$
\begin{aligned}
S_{Elm}(t) &= \frac{1}{r^{l+1}} Y_{lm}(\frac{\pi}{2}, 0) e^{im\phi} = \frac{1}{r^{l+1}} Y_{lm}(\frac{\pi}{2}, 0) \frac{(x+iy)^m}{r^m} \\
&= Y_{lm}(\frac{\pi}{2}, 0) \frac{[\cosh w + \varepsilon + i\sqrt{\varepsilon^2 - 1} \sinh w]^m}{a^{l+1}(\varepsilon \cosh w + 1)^{l+m+1}}
\end{aligned} \tag{2.91}
$$

where the reference system chosen implies the polar angle $\theta = \pi/2$ and the x,y,z-coordinates are taken from Eq. 2.89. The classical magnetic orbital integrals read [Ald75]

$$
\begin{aligned}
S_{Mlm}(t) &= \frac{i}{l} \frac{1}{\mathbf{r}(t)^{l+1}} \frac{\dot{\mathbf{r}}}{c} (-i\mathbf{r} \times \boldsymbol{\nabla}) Y_{lm}(\theta(t), \phi(t)) \\
&= \frac{av}{lc} \cot(\vartheta/2) \left(\frac{2l+1}{2l+3} [(l+1)^2 - m^2] \right)^{1/2} S_{E,l+1,m}(t)
\end{aligned} \tag{2.92}
$$

After introducing in the frequency domain the functions $S_{\pi lm}(\omega)$ are ready to be substituted into the excitation amplitudes 2.83. Such amplitudes describe in a proper way only the Rutherford orbit and not the relativistic retardation. To draw conclusions on a solution suitable for both effects the two kinds of calculations are compared: the classical and the relativistic pole [Ber88].

2.3.4 Influence of the nuclear force

All the previous considerations were done in the semiclassical approximation where the nuclei were treated to be point-like and to interact by means of the electromagnetic field only. In fact, they have finite sizes (^{208}Pb matters much more than ^{8}B in this respect) so a nuclear absorption plays a role for small impact parameters (nuclear break-up is a very weak process at the bombarding energy 254 MeV/u – see Chapter 1 for references). A more basic effect is imposed by quantum mechanics: due to the wave-packet nature of a projectile, diffraction on a target takes place. A description of high-energy heavy-ion collisions taking into account the diffraction effects is developed by Bertulani and Nathan [Ber93b] in a Glauber-like calculation.
In the quantal description trajectories with various impact parameters (not a single one) contribute to a given scattering angle. In order to account for this effect the dependence on the impact parameter in the excitation function $S_{\pi lm}$ (through the adiabaticity function K_m) should be changed. In the eikonal approximation (which is a proper method in our case of $E_\gamma/E_{LAB} \ll 1$ and $\vartheta \ll 1$, see e.g. the excellent book of Joachain [Joa83] on quantum collisions) one replaces [Ber93b]

$$K_m\left(\frac{\omega b}{\gamma v}\right) \rightarrow \int_0^\infty b\, db\, J_m(qb)\, K_m\left(\frac{\omega b}{\gamma v}\right) e^{i\chi(b)} \tag{2.93}$$

where $q = 2k\sin(\vartheta/2)$ is the momentum transfer and

$$\chi(b) = \left(-\frac{1}{\hbar v}\int_{-\infty}^{+\infty} U_N^{opt}(z', b)\, dz'\right) + \psi_C(b) \tag{2.94}$$

is the phase shift by the nuclear optical potential and the Coulomb potential where the Sommerfeld parameter η is defined by Eq. 2.38

$$\psi_C(b) = 2\eta\,[\ln(kb) + \text{const.}] \tag{2.95}$$

The first term in formula 2.95 is the contribution to the Coulomb phase of a point-like charge. The second term is a correction due to the extended charge distribution which eliminates the divergence of the Coulomb phase at the impact parameter b=0 [Ber93b].

Integral 2.94 can be evaluated when the optical potential is known. There is no data for the elastic scattering of ^{8}B on ^{208}Pb targets so an effective interaction reproducing the energy dependence of the total reaction cross-section must be constructed [Ber98]. As far as this simple optical potential is exact the excitation amplitude involves proper absorption effects.

Accuracy of the same order can be reached in a so called 'black disk' model [Typ97]. In the first approximation one considers only the phase-change due to the Coulomb force

$$\int_0^\infty \mathrm{b\,db\,J_m(qb)\,K_m}\left(\frac{\omega \mathrm{b}}{\gamma \mathrm{v}}\right) \mathrm{e}^{\mathrm{i}\chi_\mathrm{C}} \tag{2.96}$$

then, as a second step, one calculates

$$\int_0^\infty \mathrm{b\,db\,J_m(qb)\,K_m}\left(\frac{\omega \mathrm{b}}{\gamma \mathrm{v}}\right)\left(\mathrm{e}^{\mathrm{i}\chi} - \mathrm{e}^{\mathrm{i}\chi_\mathrm{C}}\right) = \int_0^{\mathrm{b_{min}}} \mathrm{b\,db\,J_m(qb)\,K_m}\left(\frac{\omega \mathrm{b}}{\gamma \mathrm{v}}\right)\left(-\mathrm{e}^{\mathrm{i}\chi_\mathrm{C}}\right) \tag{2.97}$$

Above, no nuclear contribution for impact parameters larger than the sum of the nuclear radii $\mathrm{b} > \mathrm{b_{min}} = \mathrm{R_B} + \mathrm{R_{Pb}}$ is assumed, and a complete absorption of the projectile for $\mathrm{b} < \mathrm{b_{min}}$.

Steps 2.96 and 2.97 yield together

$$\int_{\mathrm{b_{min}}}^\infty \mathrm{b\,db\,J_m(qb)\,K_m}\left(\frac{\omega \mathrm{b}}{\gamma \mathrm{v}}\right) \mathrm{e}^{\mathrm{i}\chi_\mathrm{C}(\mathrm{b})} \tag{2.98}$$

In the 'black disk' approximation [Typ97] one neglects the specific shape of the nuclear optical potential and substitutes expression 2.98 for the integral 2.93.

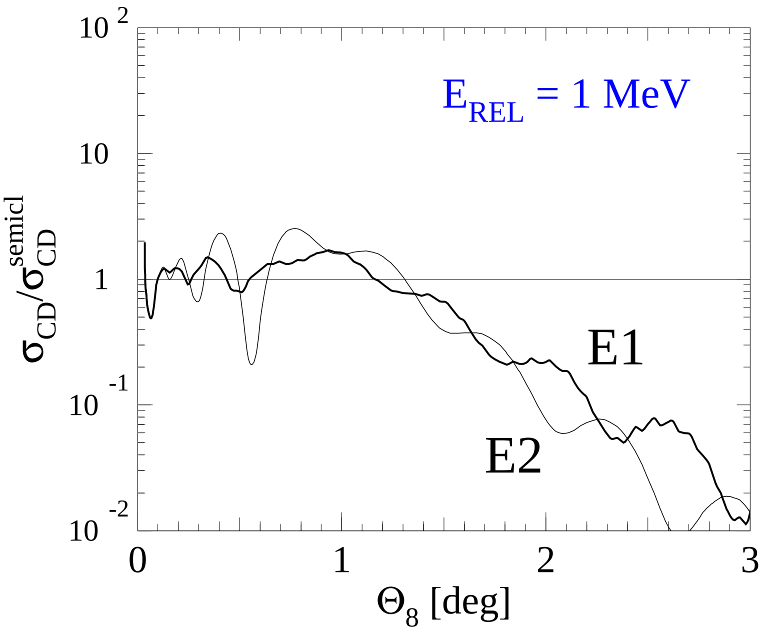

Figure 2.10: *Influence of the nuclear force [Ber98] reveals a diffraction pattern as compared to the cross-section calculated semiclassically. Below a given cut-off radius (or equivalently a cut-off angle) they do not differ crucially and the semiclassical cross-section neglecting the diffraction effects can be applied.*

2.3.5 Cross-sections and equivalent photon numbers

Finally the double-differential cross-section for the Coulomb break-up can be rewritten in the form [Ber88]

$$\frac{d^2\sigma_{CD}}{d\Omega\, dE_\gamma} = \frac{1}{E_\gamma}\sum_{\pi l}\frac{dn_{\pi l}}{d\Omega}(E_\gamma)\sigma_\gamma^{\pi l}(E_\gamma) \tag{2.99}$$

where the equivalent photon numbers per unit solid angle

$$\frac{dn_{\pi l}}{d\Omega} = \frac{Z_X^2\alpha}{2\pi}\frac{l[(2l+1)!!]^2}{(l+1)(2l+1)^3}\, c^2a^2\varepsilon^4\left(\frac{\omega}{c}\right)^{-2l+2}\sum_m |S_{\pi lm}|^2 \tag{2.100}$$

involve the excitation functions $S_{\pi lm}$ derived either in the non-relativistic limit (Rutherford bending of the trajectory) – Eqs. 2.91,2.92 or relativistic one (retardation in a straight-line motion) – Eq. 2.81. To account simultaneously for both effects an improved expression for the adiabaticity parameter can be applied: $\xi = \frac{E_\gamma b}{\hbar\gamma v} \rightarrow \frac{E_\gamma a}{\hbar\gamma v}$. Here the impact parameter b is replaced by $a = Z_X Z_c e^2/\mu v^2$-half the distance of closest approach in a head-on collision, μ-is the reduced mass of the ions and v-velocity of their relative motion.
Explicit expressions suitable for problems where both effects are present for the most important multipolarities read

$$\begin{aligned}
\frac{dn_{E1}}{d\Omega} =& \frac{Z_X^2\alpha}{4\pi^2}\left(\frac{1}{\beta}\right)^2 x^2\varepsilon^2 e^{-\pi\xi}\left\{\frac{1}{\gamma^2}\frac{\varepsilon^2-1}{\varepsilon^2}K_0^2(x) + K_1^2(x)\right\}\\
\frac{dn_{E2}}{d\Omega} =& \frac{Z_X^2\alpha}{4\pi^2}\left(\frac{1}{\beta}\right)^4 \varepsilon^2 e^{-\pi\xi}\left\{\frac{4}{\gamma^2}\left[K_1^2(x) + xK_0(x)K_1(x)\right.\right.\\
&\left.\left. +\ x^2K_0^2(x)\right] + x^2\left(2-\beta^2\right)^2 K_1^2(x)\right\}\\
\frac{dn_{M1}}{d\Omega} =& \frac{Z_X^2\alpha}{4\pi^2}x^2\varepsilon^2 e^{-\pi\xi}K_1^2(x)
\end{aligned} \tag{2.101}$$

They are easily reduced to relativistic and non-relativistic limits [Ber88].
Above, $\varepsilon = \frac{1}{\sin(\vartheta/2)}$ is the eccentricity parameter with the scattering angle ϑ, $\beta = v/c$, $\alpha = 1/137$-is the fine-structure constant, and the modified Bessel function are of argument $x = \varepsilon\xi$.

For the completeness of this description the photonuclear cross-section, being an extension of Eq. 2.34 to various multipolarities, is

$$\sigma_\gamma^{\pi l}(\omega) = \frac{(2\pi)^3(l+1)}{l[(2l+1)!!]^2}\sum_f \rho_f\left(\frac{\omega}{c}\right)^{2l-1} B(\pi l, I_i \rightarrow I_f) \tag{2.102}$$

$E_\gamma = \hbar\omega = E_c^f - E_c^i$ and $\rho_f = \frac{\mu_{ab} p_{ab}}{(2\pi\hbar)^3}$ represents the density of final states.

The reduced transition probability reads

$$B(\pi l, I_i \rightarrow I_f) = \frac{1}{2I_i + 1} \sum_{M_i M_f} \left| \langle I_f M_f \left| M(\pi lm) \right| I_i M_i \rangle \right|^2 \tag{2.103}$$

It should be stressed that the formulae are derived with the first order approximation to the Coulomb excitation process, which is very well justified by the kinematic conditions of the experiment.

Chapter 3

Experiment

In this chapter the production method of the secondary ^{8}B-beam in the fragment separator FRS of the heavy-ion facility SIS at GSI-Darmstadt, Germany is described. Then the experimental setup used to measure the invariant mass of the $^{208}\mathrm{Pb}(^{8}\mathrm{B}, ^{7}\mathrm{Be} + \mathrm{p})^{208}\mathrm{Pb}$ reaction is introduced.

3.1 ^{8}B-beam production

Since ^{8}B is an unstable isotope with a half-life of 770 ms [Ajz88] it must be produced in a reaction of some stable elements. A method for this purpose is to make a fragmentation of a heavier projectile on a primary target and then spatially separate the selected radioactive beam [Gei92]. A choice for the projectile is made by the production cross-section of a given fragment. In case of ^{8}B we used a primary beam of ^{12}C, whose ^{8}B production cross-section was assumed to be 1.55 ± 0.08 mb [Ols83].

As we intended to measure the Coulomb dissociation reaction $^{208}\mathrm{Pb}(^{8}\mathrm{B}, ^{7}\mathrm{Be}+\mathrm{p})^{208}\mathrm{Pb}$ at the highest possible energy of the projectile, we had to take into account the limit of the KaoS-spectrometer bending power. With the maximum field strength of 1.95 T [Sen93] the most effective setup of the simultaneous detection of ^{7}Be and proton has a limit of 4.0 Tm. It corresponds to the maximum ^{8}B-beam energy of 260 MeV/u. By fixing this energy on about 255 MeV/u and calculating the energy-loss of the in-beam materials, the primary ^{12}C-beam energy at the heavy-ion synchrotron SIS was determined to be 350 MeV/u.

The production sequence of the ^{8}B secondary beam was as follows. The ^{12}C beam was preaccelerated to an energy of 11.4 MeV/u in the linear accelerator UNILAC. It was then injected into the SIS synchrotron and accelerated to 350 MeV/u. Its average intensity in SIS was $4 \cdot 10^{10}$ particles/spill (spill = 7 sec.). Then it was extracted from the synchrotron in the slow mode, and directed to the fragment separator (FRS). The efficiency of the extraction was measured by the Secondary Electron Emission Transmission Monitor (SEETRAM) to be about ε=70%. At the entrance to FRS the ^{12}C beam collided the 8g/cm^2-thick production target of ^{9}Be. In such collisions of a light projectile, projectile-like ions are produced. Below, a common method of discrimination of a given isotope taking place in FRS is described.

FRS is a high-resolution forward spectrometer consisting of four 30^0 dipole stages with quadrupole doublets and triplets plus hexapoles for higher-order corrections [Gei92]. In the standard achromatic mode the whole system has the emittance of 20π mm·mrad both in the x- and y-direction. In Fig. 3.1 a sketch of the beam line is shown. Preparation of a secondary beam is based on the $\mathrm{B}\rho - \Delta\mathrm{E} - \mathrm{B}\rho$ selection method. The first (D1,D2) and the second stage (D3,D4) each perform an A/Z selection according to the magnetic rigidity, while a wedge-shaped degrader in between provides additional energy-loss selection proportional to Z^2 of the fragment. Ions of magnetic rigidity other than those selected by the dipole stage settings are eliminated from the secondary beam; this is the principle of spatial isolation of the fragments.

Table 3.1 presents the Bρ-values which were set in both stages of FRS to separate the ^{8}B fragment. It is obvious that the primary ^{12}C beam was deflected already on the first dipole (D1) since its magnetic rigidity Bρ=5.2 Tm was far off the tuned value of 4.09 Tm. In production of ^{8}B an aluminum degrader-disk was used. Together with the 516 mg/cm^2 plastic scintillator S2, it was placed in the focal plane after the D2 magnet, and served as a minimum ΔE-filter. The preparation of the beam line i.e. the ion optics and transmission optimization (beam envelope) was simulated in the Monte Carlo code MOCADI [Iwa97], which gave the settings for the magnets.

At the exit of FRS an average intensity of the secondary beam was about 10^4 ions per spill. It consisted of about 80% ^{8}B and 20% ^{7}Be-ions with a slight admixture of some other light particles (see Chapter 4). The radioactive beam was transported along the direct-transfer line to the experimental area of Cave C, where it bombarded the break-up target in front of the KaoS spectrometer.

^{8}B secondary beam					
section	$\mathrm{B}\rho_{\mathrm{out}}$	$\mathrm{E}_{\mathrm{out}}$	$\sigma_{\mathrm{E-out}}$	p	σ_{p}
	Tm	MeV/u	MeV/u	MeV/u/c	MeV/u/c
TA-S2	4.090	273.4			
S2-S8	3.982	260.6			
S8-CC	3.930	254.7	1.38	734.4	2.9

Table 3.1: *Energy of the secondary ^{8}B beam is determined from the magnetic rigidity in two stages of FRS, whereas behind FRS (S8-Cave C) it is calculated.*

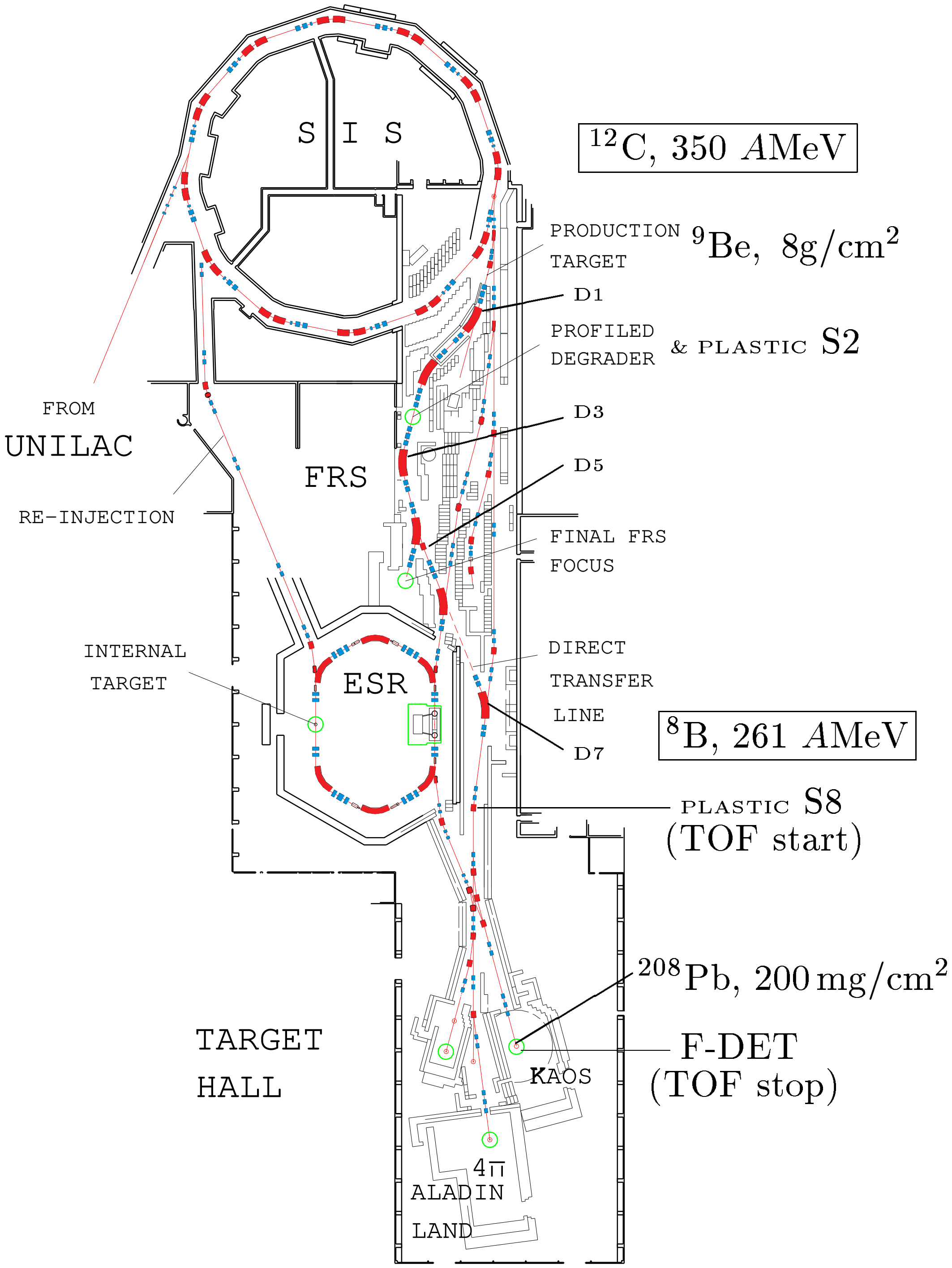

Figure 3.1: *Scheme of the GSI heavy-ion facility. A sequence of the ^{8}B secondary-beam production and the beam line to the experimental target at KaoS Cave C are shown.*

The last measured value of the beam energy comes from the value of magnetic rigidity in front of the S8 scintillator. From this point, downstream to the secondary target, it must be calculated with the simulation code ATIMA [Gei98] for the known set of the in-beam materials shown in Table 3.2, and assuming the energy spread obtained in the code MOCADI [Iwa97]. In Fig. 3.1 we can see the whole beam line down to the location of KaoS. The S8 plastic scintillator at the exit of FRS is well suited to start a time-of-flight measurement, while the plastic F-detector behind KaoS acts as a STOP wall. At our energy, the distance of 64 m between S8 and the F-detector is long enough to give good resolution of TOF, therefore it was used to recognize ^{8}B from other parasitic fragments of the secondary beam, especially ^{7}Be. S8 is 5 mm thick, so it could be used also for the energy-loss information. Unfortunately, due to count rates of about 300 kHz the energy-loss resolution was very poor and it was not possible to take advantage of the energy signal.

object	material	thickness [mg/cm^2]
SIS WINDOW	Ti	4.50
SEETRAM	Al	8.90
PRIMARY TARGET	^{9}Be	8020.70
S2 (SC21)	plastic	516.00
DEGRADER (disc)	Al	817.00
S8 (SC81)	plastic	516.00
TARGET	^{208}Pb	199.65
	Si	71.06
SSD	Si	70.60
	Si	68.73
	Si	68.73
FOIL	Fe	82.68
AIR	air	9.98
	Kapton_H	3.55
KAOS	^{2}He	<55.0>
	Kapton_H	3.55
AIR	air	<195.00>
	Kapton_H	3.55
MWPC	^{78}Ar_CO$_2$	7.42
	Kapton_H	3.55
AIR	air	<32.00>
F-DET	plastic	2170.00

Table 3.2: *In-beam materials.*

3.2 Setup of the experiment

Initially, two Parallel Plate Avalanche Counters (PPAC) were intended to track the incoming ^{8}B in front of the target. They were installed 1 and 4 m upstream from the target position, respectively. The idea was to precisely reconstruct the vertex of the reaction and to have a time signal for the TOF measurement for the beam identification.
A PPAC detector is a set of two cathodes and an anode in between, polarized with high voltage and filled with gas under low pressure. The cathodes are striped in perpendicular directions to provide a position determination through a delay-line readout of fast electrons induced on them by an avalanche made by the ionized particle. Since all three planes are made of thin foils, it gives a minimum amount of additional matter in-beam, thus minimizing the angular straggling.
The two PPACs we possessed had a time resolution of 200 ps and, dependent on it, a position resolution of 1 mm. However, they were not tight enough for low gas pressure inside, and it was a limiting factor for the high voltage that could be supplied without sparks. By reducing its value to the operational level we could reach the detection efficiency of only 60%. In addition one of the two detectors was destroyed by an implosion caused by a power supply breakdown, so we decided not to place only one PPAC detector of poor efficiency in the beam pipe. As a consequence, we do not have an event-by-event information of the beam track in front of the target.

3.2.1 Kaon Spectrometer

The Kaon Spectrometer (KaoS) is a double-focusing quadrupole-dipole system [Sen93]. It was built as a compact spectrograph for studies of meson production in collisions of heavy ions. Its geometry reflects fully requirements of the kaon detection: a short flight path (5-6.5m) for minimization of losses by decaying kaons, and high acceptance ($p_{max}/p_{min} \simeq 2$, solid angle $\Omega \leq 35$ msr with coverage of 140 and 280 mrad in vertical and horizontal directions, respectively). The advantage of very wide momentum range simultaneously analyzed with one field settings was used for the coincident detection of the break-up products. Since, in the case of Coulomb dissociation at relativistic energies, the break-up particles are dominantly focused in the beam direction, the magnet was set at 0^o i.e. along the beam line.
In principle, particles with the same absolute value of momentum should be focused exactly at the same place on the focal plane of the spectrometer. The high acceptance has its prize, however. Due to higher order aberrations one has a limit for the momentum resolution. Additionally, the multiple scattering and energy-loss straggling in the gap contribute to the same extent to the momentum smearing. To minimize the latter factor the gap was filled with helium gas. A simulation with the code GEANT [Gia94] shows that in case of air, the mo-

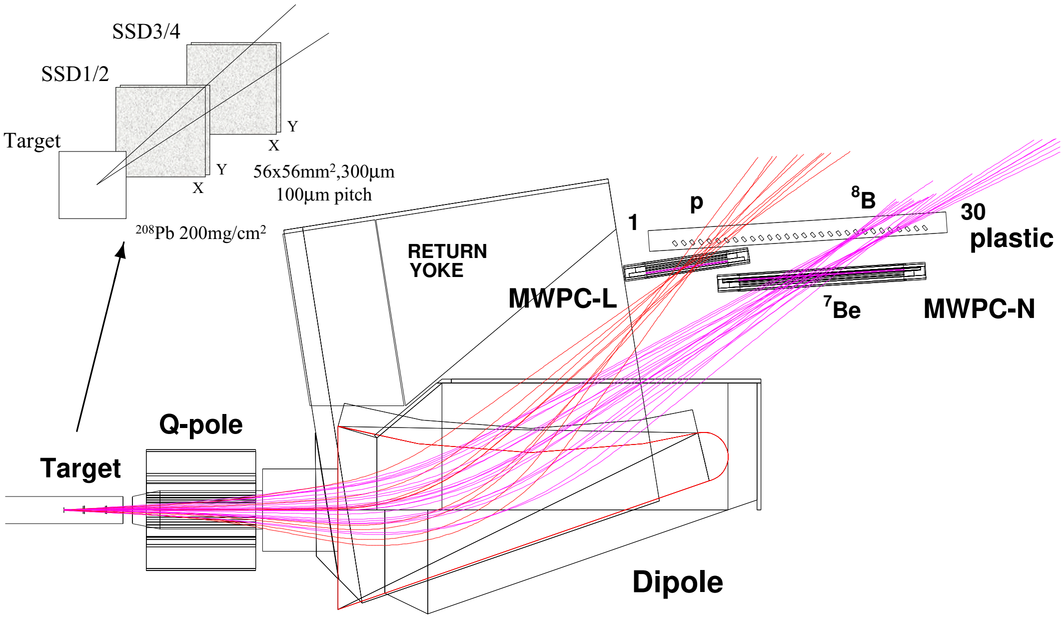

Figure 3.2: *Experimental setup in KaoS Cave C. In the left top corner a sketch of the vacuum pipe with the target and two pairs of silicon microstrip detectors separated by distances of about 15 cm, respectively, is shown.*

mentum resolution at the focal plane amounts to $\sigma_p/p \simeq 1\%$. Since KaoS has a dispersion of 2.2 m, it corresponds to a distance of about 2 cm along the focal plane. In the case of helium gas, with however two MWPC out of the focal plane, like in our setup, the 'intrinsic' momentum resolution still does not exceed 0.5% over the full solid angle.
To be able to track the particles in the simulation we had to measure the magnetic field. As the dipole magnet has a complicated shape, its ion-optics properties like field homogeneity and fringe fields had to be investigated in three dimensions. It was done with a 3-d Hall probe at GSI. Then the results were mapped into the program-package GEANT.

In the experiment, the KaoS dipole was operated at 1.54 T to perform the simultaneous detection of the break-up products. In order to check the behavior of the magnet in case of shut-downs and breaks in the run, we measured its hysteresis with a Hall probe. The hysteresis appears to be very small because the yoke and the pole pieces are made of magnetically soft iron. Moreover, the saturation effect by turning on the current 0-180 A, which corresponds to our maximum value of 1.54 T, is about 2 minutes, so relatively quick.

3.2.2 Silicon Strip Detectors

The silicon microstrip detectors (SSD) are four position sensitive planes placed, in two pairs, downstream from the target in the beam pipe, at distances of 15 and 30 cm, respectively (see Fig. 3.2). Each SSD has an area of 58×58 mm^2, a thickness of 300 μm, and is striped on one side with a pitch of 100 μm. The two sets of SSD assembled in perpendicular directions (X,Y) were intended to measure the scattering angles of the break-up particles. Since no working PPAC detector in front of the target was available, SSD were also used to measure the emittance of the beam.

Readout of individual strips of each detector was performed by daisy-chained GASSIPLEX chips [San95] and the digitizing stage by V550 and V551 CRAMS modules [CAE94a, CAE94b].

The GASSIPLEX chip is an AMPlifying multipLEXing device designed in CERN for use with silicon microstrip detectors [Beu90]. This analog-signal processor made in CMOS technology has low noise (650e$^-$+15e$^-$ per pF of input capacitance) and is low power-consuming. It can process signals within a time of two microseconds, which was very suitable to our experimental conditions. GASSIPLEX contains 16 input channels and works in three operational stages. The first stage is the Positive Transconductance Amplifier (POTA) i.e. a charge amplifier which is connected directly to the silicon strips. The second stage is the Negative Operational Transconductance Amplifier (NOTA), that is, a conjugate shaper. The last stage is the Track & Hold circuit which opens the hold capacitor to store the signal. The multiplexing block closes sequentially all 16 channels to the analog output. In order to increase the number of channels to be multiplexed at the same ADC, several GASSIPLEX chips can be 'daisy-chained'.

The module C.A.E.N. V550 is a VME Readout for Analog Multiplexed Signals housing two independent ADC blocks. In the experiment it was used to read out the front-end GASSIPLEX chips. Each block of the module can work with positive, negative, or differential input signals. The selective sensitivity of the order of mV/bit was set to provide 300 mV full input range voltage. The module uses 10 bit linear conversion. It operates in the standard way: an input signal is sampled by the ADC and, when over threshold, the pedestal (independent for each channel) is subtracted. The 2×32 bit FIFO logic provides then the storage of the output signal in a buffer. The maximum conversion rate of the unit amounts to 5 MHz; in the experiment it was operated at 0.7 MHz. The unit has diagnostic and self-test capabilities useful to easily control the operational run. The number of detector channels to be read out can be programmed via VME up to 2016 in steps of 32. In order to read out 4×576 channels we had to provide two V550 units.

The unit C.A.E.N. V551 is a VME sequencer that controls two V550 boards. The single module is able to read out up to 19 C-RAMS modules (complete VME crate) i.e. 76608 multiplexed detector channels. The model V551 can operate in a manual mode or in a remote mode; it is then possible to control it via a VME bus. The multiplexing frequency can be set from 0.5 to 5 MHz by means of a trimmer on the front panel. The timing between the clock signal and the convert signal of the acquisition cards was adjusted in the experiment with an alpha source to gain the maximum amplitude converted.

In order to operate C.A.E.N. V550 and V551 modules for the readout of the front-end analog signal processors GASSIPLEX a code under a gcc compiler performing a full control of the cards has been written [Sur95]. It was based on the MOTOROLA 68030 processor which controlled the VME bus, run under LynxOS ver. 1.39. For mapping special system memory areas into the address space of a user process, the LynxOS system calls were used. The main program source consisted of two 32-bit hardware access functions communicating with the modules. The second stage, based on the above fundamental functions, were performing a user defined action. Since the modules could be operated also in the test mode with a signal generator, a failure of the V550 electronics could be eliminated before operating it in the standard detector readout mode in the beam.

SSD have 4×576 strips to be read out. Since the GASSIPLEX plug-in board (consisting of four chips) has 64 channels, we needed 9 GASSIPLEX chips for a single detector. Unfortunately we had only eight per one crystal, so not all strips were available for the readout. We connected them in the following way: strips 1 to 480 of each detector were fully read out, in the range 481 to 544 only even strips were read out, and within 545 - 576 nothing was connected (dead strips). The silicon detectors SSD1 and SSD3 measuring positions in the X-direction were placed increasing strip number to the right, seen downstream from the target. The first Y-detector (SSD2) had its increasing strips up, while the second (SSD4) down, in the above-mentioned reference system. This system of connection was intended to minimize the loss in efficiency. In the analysis, the not fully read out regions were omitted (Chapter 4).

3.2.3 Multi Wire Proportional Counters

Multi Wire Proportional Counters (MWPC) are located near the focal plane to measure the momenta of the break-up products by determining their position in the dispersion direction. They are 120×35 cm and 60×30 cm chambers placed in the ion (MWPC-N) and in the proton momentum range (MWPC-L), respectively. A sketch of this type of chamber is given in Fig. 3.3. A 'conventional' drift chamber consists of one anode-plane with 20μm wires in distances of 1mm, and two cathodes whose wire planes are perpendicular to one another. The additional stage is a preamplification gap (pregap) consisting of two anodes separated from the first cathode with a transfer gap. The idea of two amplifying gas stages goes back to Charpak *et al.* [Cha70] and reflects the possibility of measuring minimal and strongly ionizing particles with the same detector.

A MWPC operates in the following way. A minimum-ionizing particle incident from the pregap side produces primary electrons already in the pregap. Due to the Townsend effect in the strong electric field, these electrons form an avalanche that passes through the transfer gap and is additionally amplified near the anode plane. The electron cloud is relatively quickly discharged to the anode (some ns) whereas the positive ions which are produced are more slowly and induce a signal on both cathodes. The center-of-gravity of this signal corresponds to the incident position of the particle in the pregap. A quenching gas plays an important role for an efficient detection of this kind. In the experiment the L-chamber measuring the break-up protons was operated with a mixture of argon, CO_2, and n-Heptane in proportions 78%, 20% and 2%, respectively. This composition was checked to be the most efficient [Sar91].

For the strongly ionizing particles ^{7}Be and ^{8}B new HV parameters had to be found to operate the MWPC-N chamber. This was crucial to control breakdowns in the gas, damaging the anode wires. This work is discussed completely in [Uhl98]. Due to the geometry and the power supply, the N-chamber was placed with its pregap at the back (see Fig. 3.2). This however does not matter for the principle of the two-staged gas amplification.

The readout of a single MWPC was performed in the following way. The cathode wires were connected in bunches of 5 wires to 8-bit flash ADC each. The readout was done by transputer modules T222 gathering 16 ADC, each. The transputers were linked in a line and formed a network of three chains, representing the three MWPC planes to be read out.

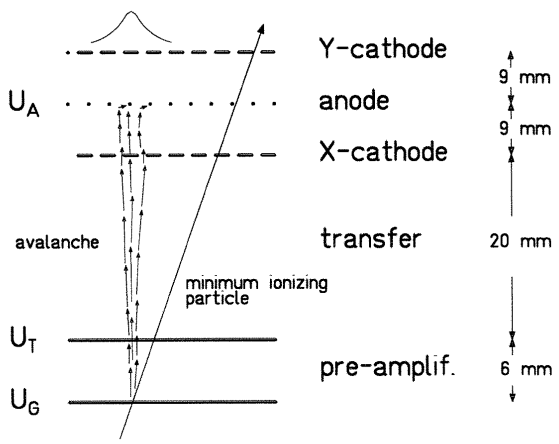

Figure 3.3: *Structure of the MWPC and its operating principle.*

3.2.4 F-Detector

The so called F-detector (FD) is an array of 30 scintillators placed near the focal plane of the KaoS dipole (see Fig. 3.2). These are plastic paddles with dimensions of $380 \times 37 \times 20$ mm each, read out at both ends with Hamamatsu R 1828 photomultipliers [Sen93]. The time and energy signals of each paddle are fed into TDCs and ADCs placed in a FASTBUS crate (see Section 3.2.5). We used these signals in the following way: time was calculated as a mean value $(\mathrm{T_{up}} + \mathrm{T_{down}})/2$ and energy loss as $(\Delta\mathrm{E_{up}} \cdot \Delta\mathrm{E_{down}})^{1/2}$. Since the width of a single paddle in the dispersion direction (37 mm) corresponds to about 2% of the momentum resolution FD is not precise enough for the momentum determination. For this purpose we used two position sensitive MWPC, as it was described in Section 3.2.3. The F-Detector fulfilled, however, two very important tasks: with it a trigger condition was built, and it served as a time-of-flight STOP-detector. Let us look at the latter first. As we have seen at the beginning of Section 3.2, an operational run of the PPAC detectors was not possible and they were dismounted from the beam line. Since the plastic time-response is very well suited for a TOF measurement, we used FD as a STOP wall for the ^{8}B beam identification, while the S8 scintillator served as a START signal. Since FD is placed behind KaoS the beam passes through additional layers of matter in the KaoS setup. When we compare, however, the distance of 60 m between the S8 START-stage and the target, we see that the additional path of 4 m to the F-detector, with the lost energy of 6 MeV/u, influences negligibly the ^{8}B TOF spectrum. Also in case of ^{7}Be being part of about 20% of the beam, we cannot mix it with the ^{7}Be break-up fragment coming from the target. A closer look on the subject of the beam composition we find in Chapter 4.

The break-up products proton and ^{7}Be have, due to their different magnetic rigidity, two separate positions at the focal plane. This is the reason why FD with its array of plastic paddles can build good trigger conditions. As we can see in Fig. 3.2 the left side of the F-detector covers the proton momentum range whereas on the right side the ions (^{7}Be, ^{8}B) are focused. The trigger scheme is shown in Fig. 3.4. We divided arbitrarily the F-detector into two parts. Paddles 1-16 and 17-30 were electronically coupled as an OR signal. A break-up event was distinguished by coincident hits in both sides of the F-detector. This is the so called 'p-Be' trigger. In case of only one hit anywhere in the paddle 17-30 region the 'BEAM' trigger was built. With this trigger the number of ^{8}B events was monitored to be able to calibrate the cross-section. Assuming the CD cross-section for $^{208}\mathrm{Pb}(^8\mathrm{B}, ^7\mathrm{Be} + \mathrm{p})^{208}\mathrm{Pb}$ to be of the order of 300 mb our 199.65 mg/cm^2-thick target yielded a break-up rate three-four orders of magnitude smaller than the beam rate. Due to dead time of the electronics only break-up events were recorded on tape. However, to keep track of the number of 'BEAM' triggers it was recorded scaled down (10^{-3}).

For testing purposes, the photomultipliers of FD were triggered by a laser

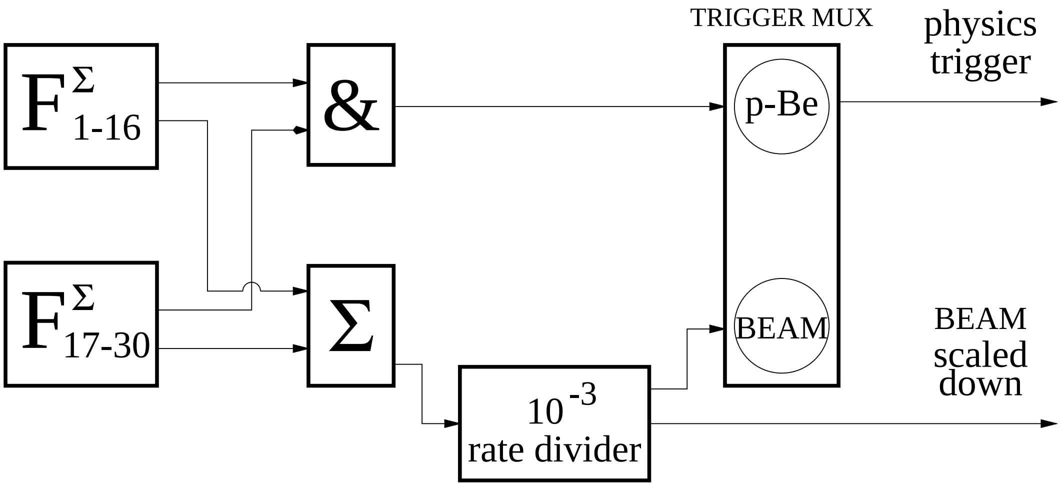

Figure 3.4: *Trigger scheme. The break-up trigger is generated by coincidence of the hits in the left and right part of the F-detector.*

before the experiment. An electronic pulser was used to control the response of the acquisition electronics.

3.2.5 Experimental electronics and data acquisition

The data acquisition system is shown in Fig. 3.5. It consisted of three branches based on VME, FASTBUS, and CAMAC controller, respectively.

- A VME crate for the readout of the silicon strip detectors housed two C.A.E.N. V550 cards being the Readout of Analog Multiplexed Signals coming from the GASSIPLEX chips (2048 channels). The C.A.E.N. V551 module is a sequencer for the V550 boards. The crate was controlled by an E7 processor (Eurocom 7 from ELTEC). Signals were transferred to the memory of the VME Master Unit.

- A FASTBUS crate served for the readout both of the two MWPCs and the plastic wall.
  The photomultiplier signals of the F-detector were split into an energy and a time branch by a sum/split card GSI SU1601. The time signal was fed through a constant-fraction discriminator GSI CF8105. Both the energy and the time branch were delayed (GSI DP1628, DL1610) in order to have a proper window to generate a trigger. The signals were fed to the SMI, a programmable controller (no CPU) of the FASTBUS crate, which operates like an event builder. The EBI is a memory unit coupled with the trigger module, where the F-subevent was stored.

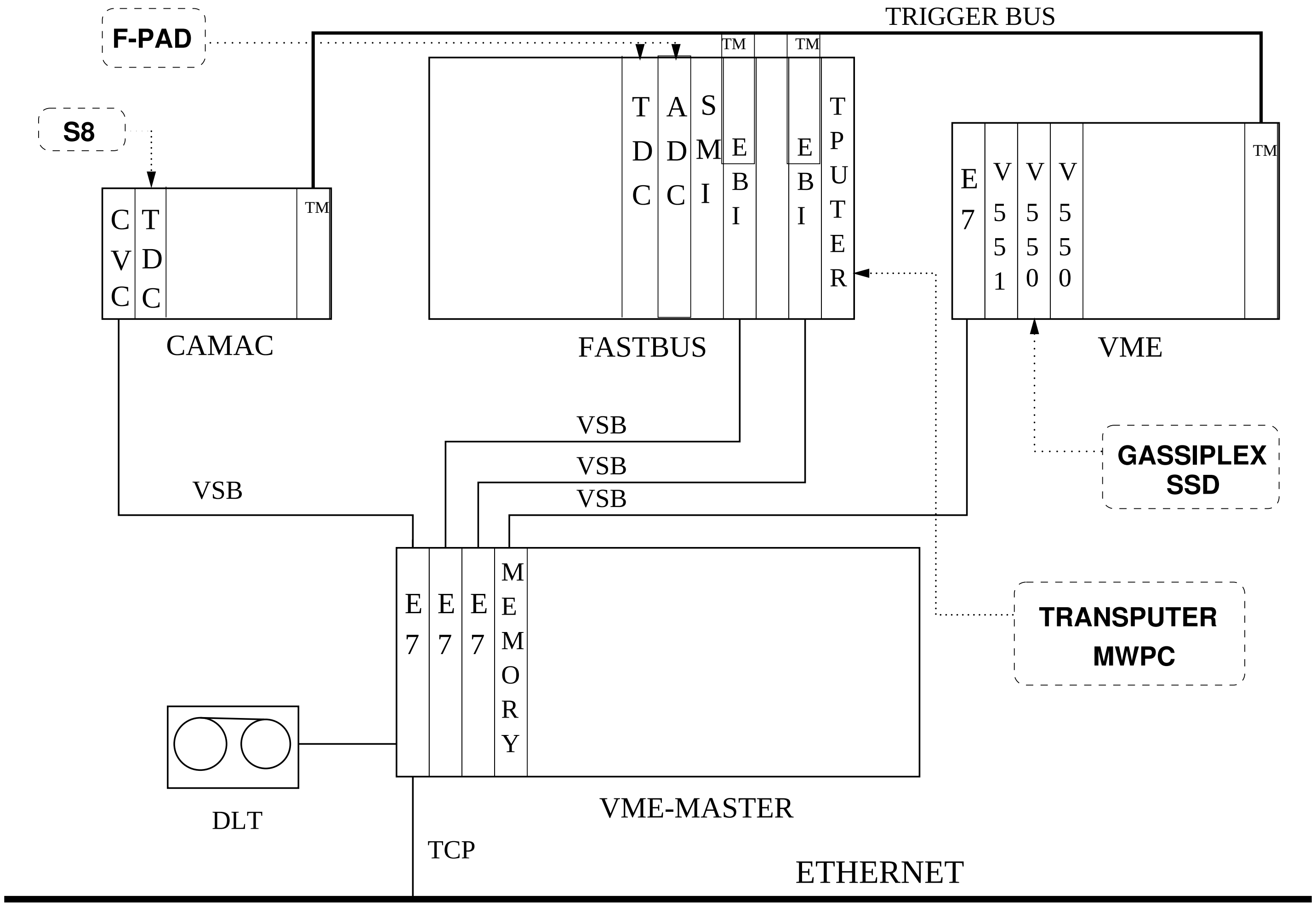

Figure 3.5: *Block-diagram of the acquisition electronics. It consists of three branches controlled by the VME Master Unit.*

The MWPC readout is a chain of the transputer modules T222 whose signals were fed to the master transputer unit in the crate. The signals were there combined to a complete subevent and stored in the EBI memory. There was no separate CPU in the FASTBUS crate, therefore it was controlled by an E7 CPU in the VME Master Unit.

- A CAMAC crate, controlled by a GSI-developed computer board CVC, received the time signal of the S8 scintillator being the START detector of the time-of-flight measurement. Additionally this crate contained a Pattern Unit and scalers (SC4800) for summing up the trigger information.

The CAMAC and the VME branch were available independently via ETHERNET connection. All branches were controlled by E7 main event builder in the VME-Master crate. The communication master-slaves was done via a VSB bus connection (a memory mapped bus). All branches had their own GSI-developed trigger modules linked with the main TRIGGER UNIT.

The complete data acquisition was performed by the Multi Branch System (MBS), run under Unix operating system Lynx ver. 1.39. All the data read out was compressed except for the CAMAC subevent. The reduction was done at the event-building stage of the processing and involved pedestal subtraction and zero suppression.
Finally, an average amount of 30 kB/s was written to a DLT tape, and was sent by ETHERNET (TCP/IP protocol) to GOOSY/PAW on-line analysis.

An additional CAMAC crate housed the experimental control devices i.e. interfaces for the high-voltage supply systems and the trigger electronics. They were controlled by a VME E6 processor via ETHERNET.
A second VME E6 processor was used to run the target ladder and to control the magnetic field of the KaoS spectrometer.

Chapter 4

Analysis

The differential cross-section $d\sigma_{CD}/dE_{REL}$ for the Coulomb dissociation $^{208}Pb(^{8}B,^{7}Be + p)^{208}Pb$ is derived when, first, the ^{8}B-particles impinging on the target, and their break-up events in the lead are identified and, then, the invariant mass is constructed. In this chapter it is explained how to discriminate the respective particles and how to calculate the normalized cross-section. In the analysis all the necessary efficiencies and errors are determined.

4.1 Data processing

The data acquisition system provides us with electronically compressed digital data stored in the GOOSY [Ess88] list-mode-data files. The raw data is then unpacked to variables which have physical meaning such as the positions on the respective detectors and the energy-deposition signals in their materials. For easy data handling and presentation the raw data are converted with the APE system [Sam92] to the Hbook format recognized in the PAW environment [Bru95]. Fig. 4.1 shows the sequence of the data processing as well as the principle of the GEANT [Gia94] simulation, which will be explained further on.
After the APE-stage of the data processing one can take advantage of the unpacked signals which are described below.

The number of triggers come from the pattern unit of the CAMAC crate. In order to pre-select the data only physical triggers are accepted here (see Chapter 3). All the laser-triggered events are rejected since their purpose is to test the photomultipliers of the plastic wall. The same is done to the pulser events used to control the electronics of all the detectors of the setup. Thus, one remains with the variable *trigger* which has two flags: the number of single hits in the right side of the plastic wall (paddles 16-30), which can be attributed to the beam particles, and the number of coincident hits from both parts of the wall (paddles 1-15 and 16-30) i.e. break-up-like events.

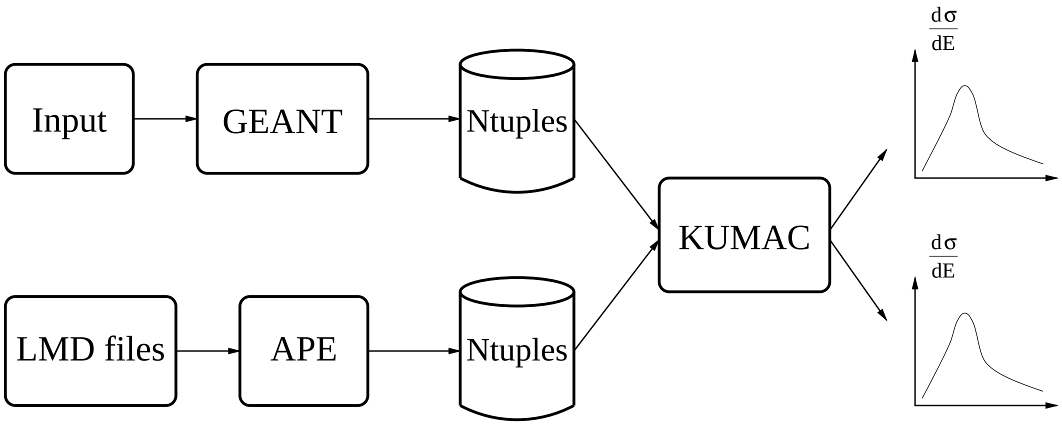

Figure 4.1: *Processing of data and simulation files.*

The CAMAC crate delivers also the values of the response time measured by the S8 detector and the plastic wall. The respective times are measured relative to the trigger signal. One has a raw time-of-flight measurement with the START and STOP signals from the above-mentioned stages, with a fixed-delay offset. The information which TOF provides is absolutely crucial. Since all the components of the beam have the same magnetic rigidity, in order to be carried through the beam optics, their velocities differ with their Z/A ratio, which results in a separation of these components in the TOF spectrum. If the separation is distinct enough one can use this information to discriminate a given TOF window i.e. a certain ion component in the beam.

The Silicon Strip Detectors (SSD) measure the energy deposited by an ion and the hit positions. The ion produces in the material of the detector a charged cloud of electron-hole pairs. The electric field in SSD separates them between the strips and the back plane. Since the cloud can be collected by more than one single wire a so called cross-talk occurs (not an electronic cross-talk, which is a capacity-coupling problem). This phenomenon increases the multiplicity of an event and requires additional care for the determination of the hit position and the energy-loss information. Reduction of the multiplicity consists in removing the cross-talks, which extend depending on the ion species and their energy (see [Bou99]). In APE the neighboring strips fired are grouped and attributed to the same particle identified by the sum of the individual energy-loss signals. The position is calculated as a centroid of the energy distribution. Due to the noise, only strips with signals above threshold are accepted to the analysis. After the APE stage of the data processing one has for each silicon detector the *position* measured as a strip number (for SSD1, SSD3 in the horizontal and for SSD2, SSD4 in the vertical direction), the energy-loss signal of an individual hit (after the cross-talk contraction it is called the *energy-loss per ion*) and the *total energy-*

loss of the event i.e. a sum of all the hits released by one trigger signal. From the list of the in-beam materials and the known ion species and their energy in the beam a calibration from the channel number into MeV of the energy-loss in a given SSD is possible. It is done with help of the program ATIMA [Gei98], which calculates various physical quantities characterizing the slowing-down of ions in matter.

The MWPC signals are unpacked from the transputer subevent. In order to localize an ion peak on the MWPC a search for a cluster, i.e. a group of neighboring wires hit, is performed. In the cluster a mean peak position is calculated. The procedure for this purpose used in APE has been adopted from the standard KaoS GOOSY analysis [Sen93]. The final variables derived in APE are the X and Y *positions* on the MWPC-N and MWPC-L.
The absolute calibration of the positions measured with the silicon strip detectors and the MWPC, with respect to the beam line, is crucial for both the precise invariant mass determination and the angular distribution of the excited ^{8}B. This topic will be discussed further on.

Besides the timing signal, which provides the TOF, the plastic wall (F-detector) yields the *energy-loss signal* constructed as it was mentioned in Chapter 3. As the energy gains and offsets of the plastic paddles differ from each other, a calibration of these quantities for the individual paddles is necessary. Such a calibration was done by measuring the energy deposit of cosmic muons. As an ion hits a certain paddle of the detector, a *position* measured in terms of the paddle number is also available.

Table 4.1 summarizes the physical variables used in the analysis.

detector	variable	unit
trigger	$\mathrm{TR_{BEAM}}$ $\mathrm{TR_{pBe}}$	count count
S8, FD	TOF	ns
SSDi i=1,2,3,4	$\mathrm{SSD1_X}$, $\mathrm{SSD3_X}$ $\mathrm{SSD2_Y}$, $\mathrm{SSD4_Y}$ $\Delta\mathrm{E_i^{ion}}$ $\Delta\mathrm{E_i^{event}}$	[cm] [cm] MeV MeV
MWPC-N MWPC-L	$\mathrm{MWPCN_X}$, $\mathrm{MWPCN_Y}$ $\mathrm{MWPCL_X}$, $\mathrm{MWPCL_Y}$	[cm] [cm]
FD	$\Delta\mathrm{E^{paddle}}$ $\mathrm{FD_X}$	channel paddle 1-30

Table 4.1: *Variables of the analysis.*

4.1.1 Stability of the measured quantities over the beam time

The experiment was a week-long measurement so one can expect variations of the beam emittance in front of the target position. It is due to a beam-line optimization done after every ion-source exchange, breakdowns (e.g. vacuum problems of the SIS-synchrotron, failures of the electronics etc.), or tuning the steering magnets in the fragment separator FRS. It affects the measured quantities (Table 4.1), and their evolution along the run number can be examined.
The fluctuations of the coordinates are irrelevant for event-by-event measurements e.g. the most important relative-energy spectrum. In cumulative spectra, however, different groups of runs can be distinguished. It is the case for the θ_8-spectrum where, due to lack of any working detector in front of the target, the reconstructed angle of the excited ^{8}B is referred to a mean-direction of the beam, incident on the target. The same is in force for the cumulative spectra of the beam emittance. Although small (i.e. not influencing the efficiency), the effect is taken into account in those cases.

In the TOF spectrum for a given trigger type (see Section 4.2.1) a slight shift in the peak positions along the runs is also observed (instability of the experimental electronics). By no means, however, it rules out the TOF as a very good particle-discrimination tool.

4.1.2 Dead time

The acquisition dead time i.e. the ratio of how many 'p-Be'-triggers were processed of all the accepted 'p-Be'-triggers is got from the information of scalers (the number of triggers after inhibit and before inhibit). In spite of the long readout time of SSD to process one event (about 1 ms), this ratio amounts to

$$\varepsilon^{\mathrm{DT}} = 95.07\% \pm 0.19\% \; (1\sigma)$$

Such a high result is due to relatively low intensity of the ^{8}B-beam (10^4/spill) and low reaction rate, which restrains pile-up events. The measured Coulomb dissociation cross-section spectra must be corrected for the efficiency factor $\varepsilon^{\mathrm{DT}}$ since only $\mathrm{TR_{pBe}}$ is affected. $\mathrm{TR_{BEAM}}$, as scaled down by a factor of 10^3, is not subject to the dead time reduction (about 2 counts of $\mathrm{TR_{BEAM}}$ may be accidently lost).

4.2 Incident beam

4.2.1 Beam composition

In Chapter 3 the production method of the radioactive ^{8}B-beam was described. The optimization done in the fragment separator FRS never results in a pure, uncontaminated secondary beam. In our case, except ^{8}B, one can expect also ^{7}Be and some other minor ions. When the contaminants produced from the primary target have broad momentum spectra they can, to some extent, cover also the magnetic rigidity used for the FRS separation of the ion it has been optimized for. A useful tool to analyze the composition of the beam is the time-of-flight spectrum i.e. the time difference between hits in the scintillator S8 placed at the exit of FRS and the focal-plane detector. Table 3.1 gives the value of the magnetic rigidity between S8 and the KaoS Cave-C, which is the only information about the incident-beam energy. For a given ion species in the beam (z denotes the charge) one can calculate its corresponding momentum p from

$$B\rho\,[\mathrm{Tm}] = 0.299792\ \mathrm{z}\ \mathrm{p}\,[\mathrm{GeV/c}] \tag{4.1}$$

and, knowing the distance traveled, calibrate the TOF spectrum by an elementary relativistic formula in nanoseconds. In the experiment, the two stages of the TOF measurement were located at a distance of 64 meters, 60 m between S8 and the target and 4 m from the target to the focal-plane detector. The energy-loss introduced by the in-beam materials placed at the latter path can be neglected with respect to the whole distance. Fig. 4.2 shows the experimental calibrated TOF spectrum for the trigger 'BEAM' (the trigger conditions are explained in Section 3.2.4). Due to different timing (different electronic fixed delay) the TOF spectrum measured for the break-up trigger is slightly shifted with respect to the one presented here, so a separate calibration is necessary.

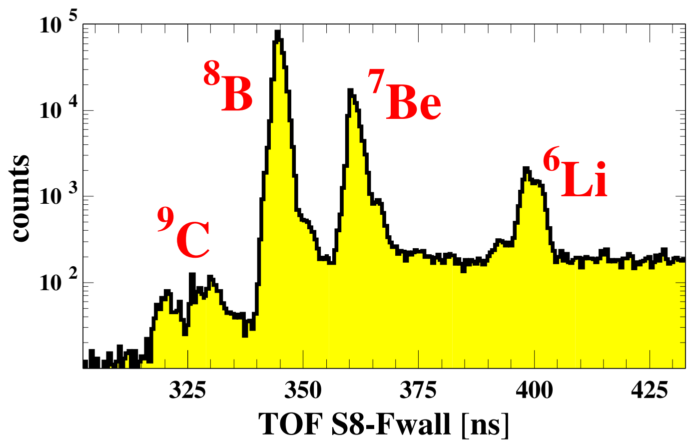

Figure 4.2: *Time-of-flight spectrum, S8-FD, triggered by the beam.*

By analyzing the peaks of TOF with respect to the most prominent ^{8}B-peak other components of the beam can be found. They are gathered in Table 4.2. The logarithmic scale used in Fig. 4.2 convinces us that the main component of

T [MeV/c^2/u]	Z/A	component	relative abundance
286.96	6/9=0.667	^{9}C	
254.66	**5/8=0.625**	**^{8}B**	82%
217.00	4/7=0.571	^{7}Be	18%
170.65	3/6=0.500	^{6}Li	

Table 4.2: *Composition of the secondary beam. The ions have the same magnetic rigidity* $B\rho = 3.93$ *Tm in the pipe.*

the secondary beam is ^{8}B. An important contribution is ^{7}Be whereas ^{6}Li and ^{9}C are negligible contaminants. Presence of such ions in the secondary beam is justified by their production cross-sections on the primary target [Ols83] in FRS.

By means of the identification methods explained in Section 4.2.3 the composition of the beam can be determined. The incident beam consists of about 82% ^{8}B and 18% ^{7}Be.

4.2.2 Emittance of the beam at the target

Emittance of the beam at the break-up target is measured by the position information $(\mathrm{SSD1_X}, \mathrm{SSD3_X}, \mathrm{SSD2_Y}, \mathrm{SSD4_Y})$ of the two pairs of SSD (see Section 4.4.1 for comments). The results are collected in Table 4.3 where the variables denote spatial coordinates in the horizontal and vertical direction (x,y) and the respective inclination angles (x',y'). The numbers are centroids of the distributions and their spreads (1σ). Note that only non-interacting ^{8}B particles are

	target [mg/cm^2]	x [mm]	σ_x	x′ [mrad]	$\sigma_{x'}$	y [mm]	σ_y	y′ [mrad]	$\sigma_{y'}$
DATA	**199.65**	-0.60	2.9	-0.36	**6.3**	0.95	5.7	-0.57	**4.2**
GEANT		-0.60	3.0	-0.39	**6.3**	0.94	5.7	-0.57	**4.2**
DATA	**none**	-0.90	2.9	-0.38	**4.8**	1.20	5.4	-0.46	**2.7**
GEANT		-0.59	3.0	-0.29	**5.2**	0.96	5.7	-0.48	**2.5**

Table 4.3: *Emittance of the* ^{8}*B-beam at the KaoS target-position, measured with and without the Pb break-up target (DATA), in comparison with results from the GEANT simulation.*

taken into account (no break-up partners in SSD); reconstructing the ^{8}B target position from the tracks of ^{7}Be and proton would broaden the distribution.

Multiple Coulomb scattering (MCS) in the target material can be evaluated by comparing the runs with and without target. The effect is clearly visible by the smearing of the angular distributions (in boldface). Results of the GEANT simulation are in agreement with the data which manifests a proper treatment of the atomic phenomena in the simulation code. It is important in order to explain the experimental resolution which is affected solely by MCS in the lead target.

The dimension of the target is X = 32mm × Y = 20mm. In Table 4.3 we can see that the beam spot is expanded beyond the target dimensions more in Y direction. Since the target is mounted on a frame (target ladder) interactions with its material are expected. Fig. 4.3 shows the ratio of the identified ^{7}Be from break-up events and the distribution of ^{8}B (about the identification see Section 4.2.3, 4.3.2). It is the cross-section profile in X and Y direction since this ratio measures the number of target atoms. The target frame is made of aluminum which contains about 50 times more target atoms per cm^2 than ^{208}Pb. On the other hand the probability to interact with Al is about 4 times lower than with ^{208}Pb. The netto effect is visible as the enhancements at the edges of the central part, corresponding to the area of lead. In the analysis the active spot of the lead target for the ^{8}B-CD is considered to be limited by the range of (-1cm,1cm) in both directions. The efficiency of this target cut amounts to

$$\varepsilon^{\mathrm{TG}} = 90.45\% \pm 0.20\% \; (1\sigma).$$

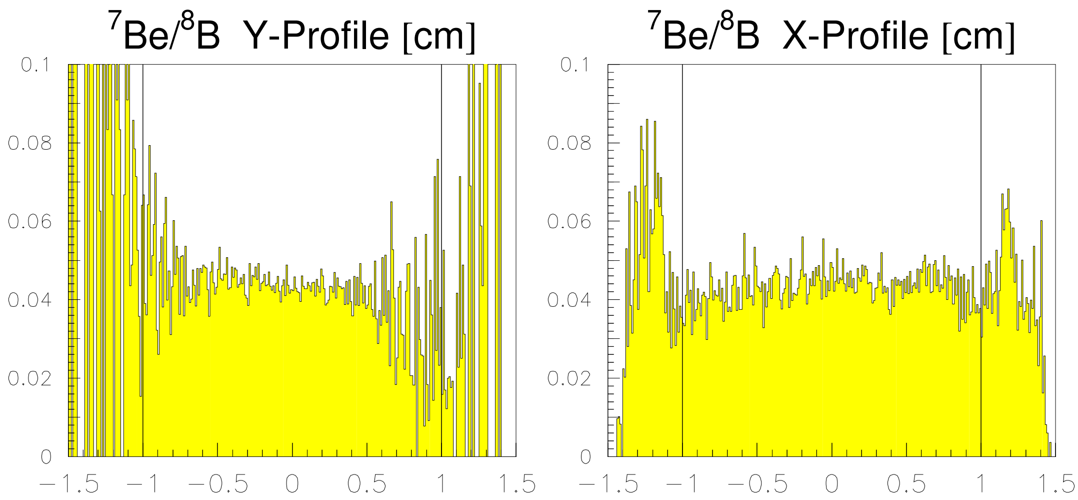

Figure 4.3: *Cross-section profiles.*

4.2.3 Number of ^{8}B in the incident beam

Identification by the time-of-flight measurement

In Fig. 4.2 one can see that the distributions are not sharp and a sort of pedestal is present. The problem of the broad TOF peaks is due to the STOP signal which is generated by several F-paddles hit (not a single one), which are not exactly aligned in time. The visible pedestal is built by events which fire the TDC of the START-stage but for any reason (mostly due to the gaps between plastic paddles of FD) have no stop signal, i.e. yield overflow. Uncorrelated STOP signals from the background can lead to the same effect. The efficiency of the identification with the TOF method one gets by evaluating the number of the ^{8}B events (recognized by energy-loss in SSDs) found outside the ^{8}B peak in the overflow tail of the distribution. It amounts to

$$\varepsilon^{\mathrm{TOF}} = 91.90\% \pm 0.10\% \; (1\sigma).$$

Separate gates for the ^{8}B selection in TOF are given in Table 4.4 for trigger $\mathrm{TR_{BEAM}}$ and $\mathrm{TR_{pBe}}$.

Identification by the energy-loss in SSD

Each SSD provides us with the energy-loss-per-ion signal. This is a very good and important tool for particle discrimination. A thorough description of the analysis leading to the energy-loss selection is explained in Section 4.3 for the case of ^{7}Be. Here we refere to Fig. 4.6 on page 80 to explain how ^{8}B is identified. Fig. 4.6 presents energy-loss distributions in the four SSD. The prominent peak of ^{8}B is well separated from other ions but there is an overlap with ^{7}Be. Owing to the fact that in each SSD the Gaussian-like ^{8}B-distribution has a slightly different position and width, one needs four different gates for selection of ^{8}B. By requiring all four SSD energy-loss-per-ion gates in coincidence an efficient identification of ^{8}B is possible. When we require each ΔE-gate in a range of plus minus three sigma around the mean value of the respective Gaussian distribution we have a probability of $(99.73\%)^4 = 98.92\%$ to find ^{8}B by the energy-loss-per-ion method. Since within the gates on ^{8}B 13%, 22%, 58% and 6% of the ^{7}Be events in $\mathrm{SSD_1}$-$\mathrm{SSD_4}$ are also present, a wrong identification of ^{7}Be as ^{8}B is probable in $13\% \times 22\% \times 58\% \times 6\% = 0.1\%$ of the cases. Hence the efficiency of the method is

$$\varepsilon^{\Delta\mathrm{E}} = 98.92\% \pm 0.10\% \; (1\sigma).$$

In Table 4.4 the windows on ^{8}B ΔE-selection are collected. The same procedure (with the same efficiency of the method) refers to ^{7}Be. In Fig. 4.6 the identified

$\mathbf{N_B^{raw} = 10^3 \times TR_{BEAM}\,(F_{1-30}) + TR_{pBe}\,(F_{1-16}\ \wedge\ F_{17-30})}$		
condition	window	trigger type
multiplicity	SSD,MWPC-N,FD>0	
Pb-breakup	$-10\text{mm} < \text{X}_{\text{TARGET}} < 10\text{mm}$ $-10\text{mm} < \text{Y}_{\text{TARGET}} < 10\text{mm}$	
TOF	$339.4\text{ns} < \text{TOF} < 351.5\text{ns}$ $336.3\text{ns} < \text{TOF} < 358.7\text{ns}$	TR_{BEAM} TR_{pBe}
ΔE	$\Delta\text{E}^{\text{ion}}_{\text{SSDi}}(^8\text{B}) \in (\text{peak} \pm 3\sigma)$ **1.** $(5.58, 0.45)$ MeV **2.** $(5.55, 0.45)$ MeV **3.** $(5.42, 0.56)$ MeV **4.** $(5.42, 0.47)$ MeV	 TR_{BEAM}

Table 4.4: *Conditions for selection of ^{8}B-particles impinging on the central part of the lead target.*

components of the beam are superimposed as the chequered (^{8}B) and hatched (^{7}Be) histograms.

To get the number of ^{8}B impinging on the target ^{8}B was recognized within the trigger condition TR_{BEAM} (ΔE, TOF) corresponding to non-interacting projectiles. For this trigger-type no reactions occurring in the detectors are assumed. The projectile is supposed to reach FD and to release TR_{BEAM}. Since TR_{BEAM} was recorded scaled-down by a factor of 10^3 the number of ^{8}B found is multiplied by this factor.

The number of ^{8}B-projectiles identified by a given method ($\text{N}_\text{B}^{\text{raw}}$) has to be corrected for the efficiency of the selection to yield the true number of $^8\text{B} - \text{N}_\text{B}$ (the intrinsic efficiency of the detectors is assumed to be 100%). The results are shown in Table 4.5. We can see that they are consistent. The total number of ^{8}B for trigger TR_{BEAM} is taken as deduced by the TOF&ΔE method.

Trigger TR_{pBe} corresponds to break-up events where two parts of FD are hit. It is clear that TR_{pBe} also counts to the total number of ^{8}B as soon as at least

METHOD	$\text{N}_\text{B}^{\text{raw}}(\text{TR}_{\text{BEAM}})$ $[10^8]$	$\varepsilon_{\text{METHOD}}$	$\text{N}_\text{B}(\text{TR}_{\text{BEAM}})$ $[10^8]$
ΔE	2.4894	0.9892 ± 0.001	2.5166 ± 0.0025
TOF	2.3988	0.9190 ± 0.001	2.6102 ± 0.0028
TOF&ΔE	2.2723	0.9190×0.9892	$\mathbf{2.4996 \pm 0.0063}$

Table 4.5: *Number of ^{8}B in TR_{BEAM} to normalize the CD cross-section.*

two particles are detected and ^{8}B-projectile is found. The latter is possible in this case only in TOF, which is negligibly sensitive to reactions in the setup. However, it is worth mentioning that ^{7}Be from the beam can react in the setup producing (at least) two fragments that can induce $\mathrm{TR_{pBe}}$ with the reaction probability very close to that of ^{8}B. In this way the proportion of ^{8}B and ^{7}Be in the beam is almost identical for $\mathrm{TR_{BEAM}}$ and $\mathrm{TR_{pBe}}$ and the number of $\mathrm{N_B(TR_{pBe})}$ is available also by the energy-loss-per-ion method.

METHOD	$\mathrm{N_B^{raw}(TR_{pBe})}$ [10^5]	$\varepsilon_{\mathrm{METHOD}}$	$\mathrm{N_B(TR_{pBe})}$ [10^5]
TOF	5.8234	0.9190 ± 0.001	$\mathbf{6.3367 \pm 0.0069}$

Table 4.6: *Number of ^{8}B in TR_{pBe} to normalize the CD cross-section. Note its magnitude in contrast to TR_{BEAM}.*

Finally we have $\mathrm{N_B = N_B^{TOF\&\Delta E}(TR_{BEAM}) + N_B^{TOF}(TR_{pBe})} = (2.5059 \pm 0.0053) \times 10^8$.

A correction for particle-loss due to interaction with materials in the setup (nuclear absorption) will be discussed in Section 4.6.4.

To normalize the cross-section one needs to calculate the product of $\mathrm{N_B}$ and the number of ^{208}Pb target atoms $\mathrm{N_{Pb} = d_{Pb}\, A_V / m_{Pb}^{mol}}$, where $\mathrm{A_V}$ -the Avogadro constant, $\mathrm{m_{Pb}^{mol}} = 207976.8\,\mathrm{mg/mol}$, and $\mathrm{d_{Pb}} = (199.65 \pm 0.2)\,\mathrm{mg/cm^2}$ is the target thickness. We get $\mathrm{N_{Pb}} = (5.781 \pm 0.006) \times 10^{-4}\,\mathrm{b^{-1}}$, and the product yields

$$\mathrm{N_{Pb} \cdot N_B} = (144.867 \pm 0.337) \times 10^6\,\mathrm{mb^{-1}}$$

4.3 Break-up

In this section it is explained how to discriminate the products of the ^{8}B Coulomb break-up. It seems that there is a clear distinction between events from a reaction in the Pb-target and the non-interacting beam. The first case should be characterized by coincident hits in the left and right part of FD thus generating TR_{pBe}. However, some break-up protons have insufficient energy-loss in FD and the left part of FD is not triggered. Instead of TR_{pBe} such events feed TR_{BEAM}. Hence, the determination of the break-up products cannot be based on requiring the trigger condition only.

4.3.1 Study of the break-up products

First let us study all possible break-up events. To show that also other reaction channels than $^{8}B \rightarrow ^{7}Be + p$ are fed we use the total energy-loss signal in any SSD. Such a spectrum is shown in Fig. 4.4 for SSD4. The total energy deposited in the material of a single SSD, ΔE^{event}, is the sum of all energy-loss-per-ion signals, ΔE^{ion}, present in one TR_{pBe} event (this is however true for any trigger). Since it is proportional to the sum of Z^2 of the ions impinging on the detector, we find in the minimum-bias spectrum (hatched), for SSD4 multiplicity equal (at

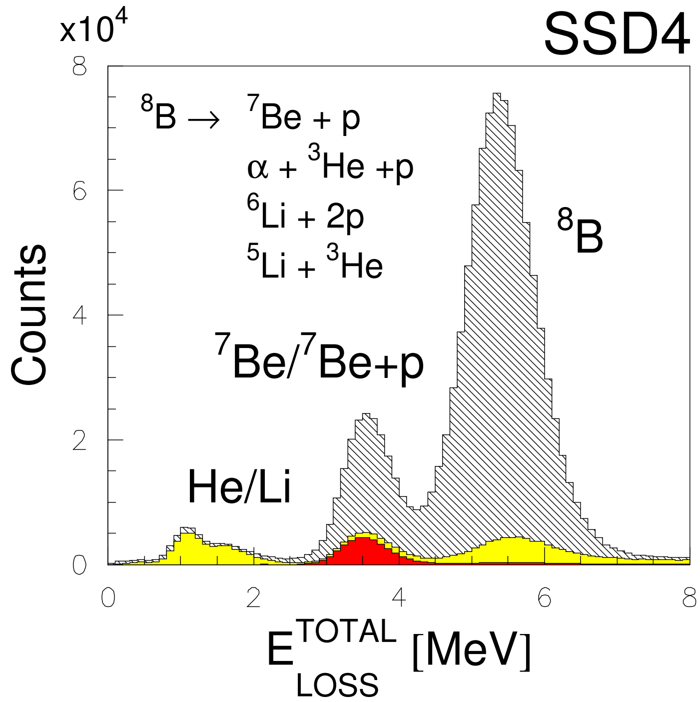

Figure 4.4: *Total energy-loss in a single SSD. The hatched, grey and black shading is explained in the text.*

least) two (grey histogram), from right to left:
– ^{8}B from the beam ($\Sigma Z^2 = 25$) (see comments on TR_{BEAM} and TR_{pBe} on page 76).
– $^8B \rightarrow {}^7Be + p$ ($\Sigma Z^2 = 16 + 1 = 17$) or ^{7}Be from the beam ($\Sigma Z^2 = 16$). These two cases cannot be distinguished due to the very small energy-loss of protons in silicon, close to noise.
– The third, left-most peak consists, in fact, of three close peaks. Process $^8B \rightarrow {}^5Li + {}^3He$ ($\Sigma Z^2 = 9 + 4 = 13$), though possible, is very weak and therefore not visible. $^8B \rightarrow {}^6Li + 2p$ ($\Sigma Z^2 = 9 + 2 = 11$) is less probable than $^8B \rightarrow {}^4He + {}^3He + p$ ($\Sigma Z^2 = 4 + 4 + 1 = 9$), which is most pronounced.

The reaction channels found here are consistent with calculations in ATIMA [Gei98] for energy-loss signals in silicon.

The black histogram shows cuts from Section 4.3.2 when they are displayed in a representation of the ΔE^{event}-spectrum.

We saw in Section 4.2.1 that the secondary beam is not homogeneous and consists of two main components ^{8}B and ^{7}Be in the proportion of about 82%/18%. Both of them can undergo disintegration in the layers of matter in the setup.

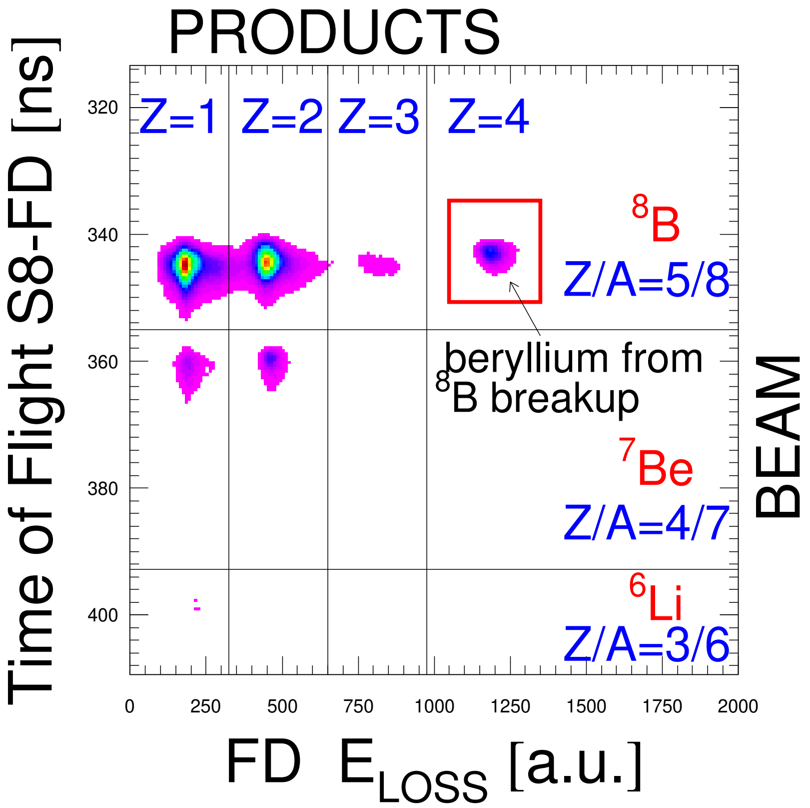

Figure 4.5: *Energy-loss in FD vs. time-of-flight S8-FD is a good tool to study the beam composition and the break-up products.*

Fig. 4.4 shows reactions leading to fragments of ^{8}B. They overlap those coming from ^{7}Be. In order to know which beam component a given fragment comes from, let us analyze TOF *vs.* energy-loss signals in FD, ΔE^{paddle}. Due to the fact that a particle can fire two neighboring plastic paddles, which worsen the resolution of ΔE^{paddle}, the energy-loss selection in FD is not as sharp as that of SSD. It is used here to display only qualitatively all the reactions of a given beam component. The two-dimensional spectrum TOF *vs.* ΔE^{paddle} is shown in Fig. 4.5 for TR_{pBe}. On the vertical axis we can see three different fragments in the beam (mainly ^{8}B and ^{7}Be). The horizontal axis shows ions separated with different energy-loss in the plastic wall. The energy-loss scales like Z^2 and we recognize proton, helium, lithium and beryllium. The spot attributed to ^{7}Be from the break-up of ^{8}B is very distinct.

4.3.2 Identification of ^{7}Be

Like in the case of ^{8}B from the beam, in order to determine whether ^{7}Be is the product of the ^{8}B Coulomb break-up the energy-loss-per-ion signal of each SSD was used. It is shown in Fig. 4.6. The selection steps are indicated as follows:
– The minimum-bias ΔE^{ion}-spectrum for TR_{pBe} is sketched in white.
– The windows of $\pm 3\sigma$ around the ^{8}B and ^{7}Be peak in each of four SSD are superimposed as the chequered and hatched histograms, respectively (the method is explained for ^{8}B in Section 4.2.3). These peaks are the components of the beam.
– Multiplicity at least 2 in each SSD makes the grey histogram. It is interesting to compare grey histograms in Fig. 4.6 (ΔE^{ion}) and Fig. 4.4 (ΔE^{event}).
– The windows of $\pm 3\sigma$ around the ^{7}Be peak from the reaction under the condition that ^{8}B is found in TOF.
This black is the crucial cut showing ^{7}Be ($\Delta E_i^{ion} \approx 3.5$ MeV) from the ^{8}B break-up. Note that the energy-loss signals of ^{7}Be from CD are slightly different than those of ^{7}Be from the beam ($E_{BEAM}(^{7}\mathrm{Be}) = 217$ MeV/u, see Table 4.2; $E_{CD}(^{7}\mathrm{Be}) \approx 254$ MeV/u). It is worth mentioning that any reaction producing ^{7}Be outside the ^{208}Pb-target or the case of ^{7}Be interacting in SSD are excluded by the requirement that the ΔE^{ion} conditions for ^{7}Be are fulfilled for all four SSD.

The cut for ^{7}Be being the product of the ^{8}B break-up has the selection efficiency $\varepsilon(^{7}\mathrm{Be}) = 91.90\% \pm 0.10\%$ (the efficiency of the ^{8}B determination in TOF – see Table 4.6).

Table 4.7 summarizes the steps of ^{7}Be selection.

The energy-loss for protons as found by ATIMA [Gei98] is only 200 keV and it lies within the range of noise. Hence the energy-loss spectrum in SSD is not the appropriate tool to select the CD protons. The sharp peak presented here is the result of the proton selection discussed further in Section 4.3.3.

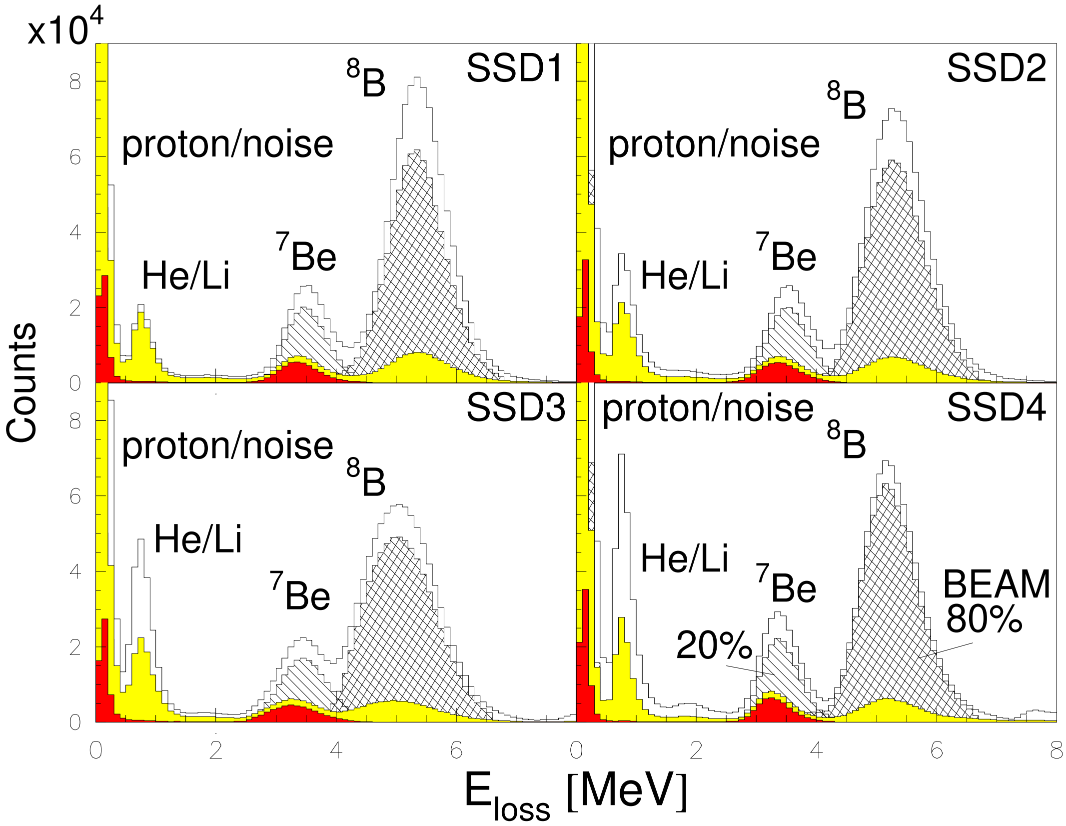

Figure 4.6: *Identification of ^{7}Be from ^{8}B break-up by analyzing the energy-loss-per-ion information.*

^{7}Be from the ^{8}B-CD in lead

condition	window	trigger type
multiplicity	SSD>1	
Pb-breakup	$-10\text{mm} < X_{\text{TARGET}} < 10\text{mm}$ $-10\text{mm} < Y_{\text{TARGET}} < 10\text{mm}$	
ΔE	$\Delta E^{\text{ion}}_{\text{SSDi}}(^{7}\text{Be}) \in (\text{peak} \pm 3\sigma)$ **1.** $(3.57, 0.32)_1$ MeV **2.** $(3.55, 0.31)_2$ MeV **3.** $(3.46, 0.41)_3$ MeV **4.** $(3.46, 0.30)_4$ MeV	TR_{pBe}
^{8}B-CD	$336.3\text{ns} < \text{TOF} < 358.7\text{ns}$	TR_{pBe}

Table 4.7: *Conditions for selecting ^{7}Be from ^{8}B Coulomb break-up in the ^{208}Pb target.*

4.3.3 Identification of the break-up proton

Unlike in the case of ^{7}Be, the energy-loss cut cannot be applied to unambiguously identify the CD protons. The precise selection of both break-up partners is, however, important for determination of the invariant mass. As an additional tool to discriminate the CD protons the reaction vertex within the ^{208}Pb target is reconstructed.

As we remember, SSD provide us with position information of the impinging particles. The X and Y SSD are placed in two pairs 15 cm from one another and 15 and 30 cm from the target. This makes the tracking possible. The Z coordinate is taken along the beam line with its origin in the middle of the target.

The procedure to search for the CD proton is as follows:
– As soon as we have identified ^{7}Be by its energy-loss windows in SSD the ^{7}Be trajectory is known and its position on the target can be deduced.
– For events with multiplicity at least 2 in each SSD we follow the ^{7}Be track and reconstruct the trajectory (one or more if present) of the remaining particle. Due to finite experimental resolution (multiple Coulomb scattering in the materials) we do not expect that this track and the track of ^{7}Be intersect exactly somewhere within the target thickness (see Fig. 4.7). Instead, we calculate the point of closest approach in the Z-direction by minimizing the distance D(Z) between the two

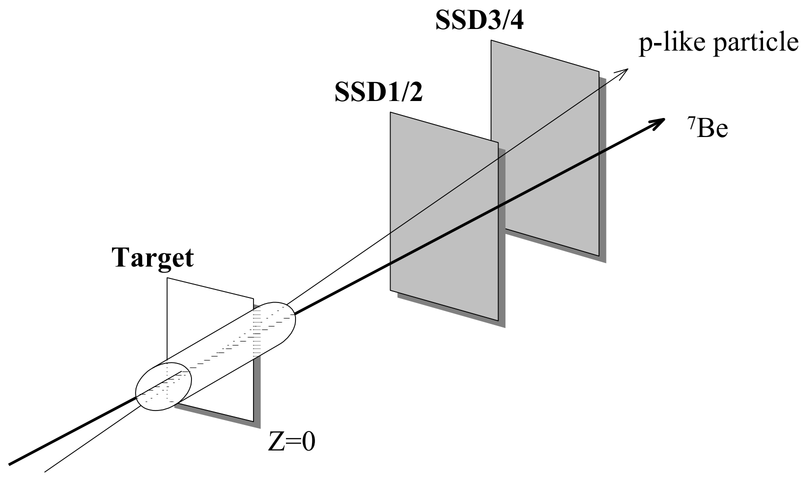

Figure 4.7: *Principle of the proton search.*

trajectories $D(Z) = \sqrt{(X_{Be}(Z) - X_p(Z))^2 + (Y_{Be}(Z) - Y_p(Z))^2}$, where the index p denotes the second particle which could be the proton. The closest approach we call the interaction point, Z_{int}, it is attained from the condition dD/dZ=0. For Z_{int} we calculate for both particles their coordinates in the X- and Y-direction. X_{int} and Y_{int} we take as the mean value $X_{int} = (X_{Be}(Z_{int}) + X_p(Z_{int}))/2$, $Y_{int} = (Y_{Be}(Z_{int}) + Y_p(Z_{int}))/2$. The interaction coordinates are shown in Fig. 4.8.
– Since, by rescattering in the setup, (noise or) other protons than the one of CD are present, the procedure yields in one event a number of combinations and additional criteria are needed to associate the right proton to ^{7}Be.
Firstly, the paths of ^{7}Be and p should be diverging downstream from the target. Secondly, the interaction point should be within the target range (we note also break-up events that are produced in SSD – see the maximum in Z_{int} between the two pairs of SSD). Finally, if still more than one combination remains (few cases), the case of the smallest $\sqrt{X_{int}^2 + Y_{int}^2 + Z_{int}^2}$ is chosen.

The result is shown in black in Fig. 4.8. From huge background of events protons originating from the break-up reaction in the target are selected. For the black spectra the mean positions and their standard deviations are found

$$X_{int} = -0.68 \text{ mm} \pm 2.97 \text{ mm} \qquad Y_{int} = 1.05 \text{ mm} \pm 5.65 \text{ mm}$$

By comparison with Table 4.3 we see that they reflect the beam spread.
For Z_{int} we find

$$Z_{int} = 1.05 \text{ mm} \pm 7.10 \text{ mm}$$

It is clear that the uncertainty in the determination of the interaction point along the beam direction is much larger than the target thickness (0.176mm). It is due to the fact that the opening angle of the reaction is small (see Section 4.4) and

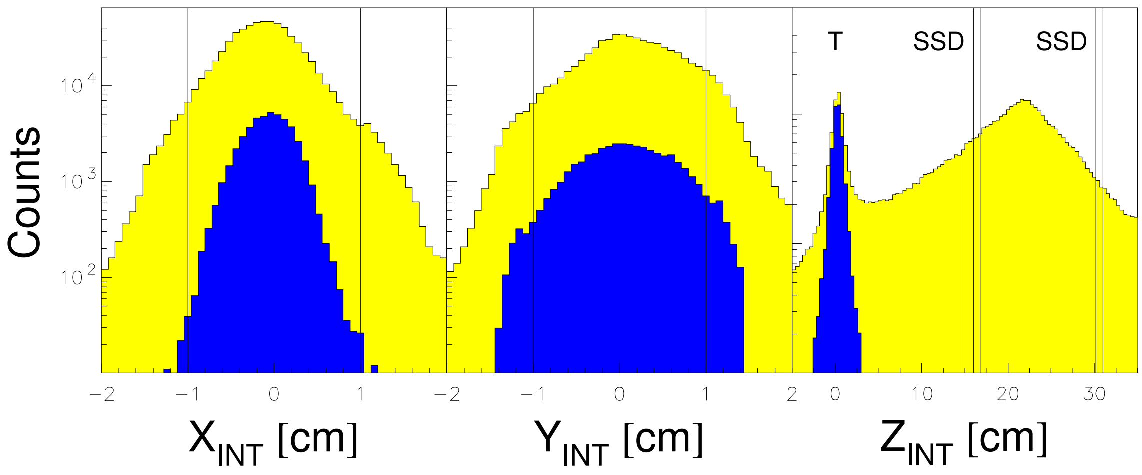

Figure 4.8: *Vertex on a target shows the proton origin.*

the resulting paths are almost parallel thus yielding a relatively large error of the interaction point. However, the first material after the target is SSD1, which is placed 150 mm downstream, and the identification of the vertex within ^{208}Pb is by no means unambiguous.
The vertex-reconstruction method of matching proton to the identified ^{7}Be is assumed to have an efficiency equal to 100%. It is due to the fact that all the identified CD-protons have their energy-loss, although quite low (about 200 keV), above the SSD threshold, which means they all can be selected. An issue arises how probable misidentification of noise for a true proton signal is. The idea of evaluating this kind of a systematic error is as follows [Bou99]: In trigger $\mathrm{TR_{BEAM}}$ we identify about 1.6% of events which seem to be 'true' CD events i.e. in SSD-$\Delta\mathrm{E}^{\mathrm{ion}}$ we select ^{7}Be and an apparent partner determined with the reaction vertex is present. The latter must be, however, a noise signal since a detailed analysis (e.g. requiring ^{8}B in TOF, ^{7}Be and proton signal in MWPC, ^{7}Be in FD-ΔE) shows that only about 0.02% of such events may be true CD events. As a result, one may consider that 1.6% of the identified CD events are due to ^{7}Be plus a noise signal. Therefore this quantity is taken as the uncertainty of the vertex-reconstruction efficiency

$$\varepsilon^{\mathrm{vertex}} = 100\% \pm 1.6\%$$

The total efficiency to find CD events is then

$$\varepsilon^{\mathrm{CD}} = \varepsilon(^{7}\mathrm{Be}) \cdot \varepsilon(\mathrm{p}) = 91.90\% \pm 1.60\%$$

where $\varepsilon(^{7}\mathrm{Be})$ evaluated in Section 4.3.2 was used.

In the 199.65mg/cm^2-target a total number of 37357 breakup events is found. The yield obtained within the active target window, $\mathrm{X_T}, \mathrm{Y_T} \in (-1\mathrm{cm}, 1\mathrm{cm})$, amounts to 33659 CD-events. Their ratio, 90.10%, corresponds well to the efficiency of the target cut given in Section 4.2.2.

4.4 Reconstruction of the invariant mass

Our experimental goal was to reconstruct the invariant mass in the system ^{208}Pb(^{8}B $\rightarrow ^7$Be+p)^{208}Pb. For that purpose the ^{8}B-break-up products were identified in coincidence. Now, according to Formula 1.4, the laboratory momenta $\mathrm{p_{Be}}$, $\mathrm{p_p}$ and the opening angle θ_{17} between the fragments must be determined. This is done as follows.

The momenta of particles running through KaoS can, in principle, be determined from positions in the focal plane of the spectrometer (see Chapter 3). In reality this is not feasible. Firstly, KaoS has a very large momentum acceptance which causes aberrations compared to first-order ion optics [Sen93]. Secondly, the two MWPC, which are intended to measure the positions of the reaction products in the dispersion and vertical direction, are placed off the focal plane. For these reasons it is clear that the measured positions behind KaoS do not correspond to the absolute-momentum vectors but depend also on the angles at which particles enter the spectrometer. Since these angles are deduced from the positions in SSD we write, up to the third-order matrix elements,the momentum vector in the form of a function

$$
\begin{aligned}
\mathrm{p} = \mathrm{u_0} & \\
&+ \mathrm{u_1 X_{SSD}} + \mathrm{u_2 Y_{SSD}} + \mathrm{u_3 X_{N/L}} + \mathrm{u_4 Y_{N/L}} \\
&+ \mathrm{u_5 X^2_{SSD}} + \mathrm{u_6 X_{SSD} Y_{SSD}} + \mathrm{u_7 X_{SSD} X_{N/L}} + \mathrm{u_8 X_{SSD} Y_{N/L}} \\
&+ \mathrm{u_9 Y^2_{SSD}} + \mathrm{u_{10} Y_{SSD} X_{N/L}} + \mathrm{u_{11} Y_{SSD} Y_{N/L}} \\
&+ \mathrm{u_{12} X^2_{N/L}} + \mathrm{u_{13} X_{N/L} Y_{N/L}} \\
&+ \mathrm{u_{14} Y^2_{N/L}} \\
&+ \mathrm{u_{15} X^3_{SSD}} + \mathrm{u_{16} X^2_{SSD} Y_{SSD}} + \mathrm{u_{17} X^2_{SSD} X_{N/L}} + \mathrm{u_{18} X^2_{SSD} Y_{N/L}} \\
&+ \mathrm{u_{19} X_{SSD} Y^2_{SSD}} + \mathrm{u_{20} X_{SSD} Y_{SSD} X_{N/L}} + \mathrm{u_{21} X_{SSD} Y_{SSD} Y_{N/L}} \\
&+ \mathrm{u_{22} X_{SSD} X^2_{N/L}} + \mathrm{u_{23} X_{SSD} X_{N/L} Y_{N/L}} \\
&+ \mathrm{u_{24} X_{SSD} Y^2_{N/L}} \\
&+ \mathrm{u_{25} Y^3_{SSD}} + \mathrm{u_{26} Y^2_{SSD} X_{N/L}} + \mathrm{u_{27} Y^2_{SSD} Y_{N/L}} \\
&+ \mathrm{u_{28} Y_{SSD} X^2_{N/L}} + \mathrm{u_{29} Y_{SSD} X_{N/L} Y_{N/L}} \\
&+ \mathrm{u_{30} Y_{SSD} Y^2_{N/L}} \\
&+ \mathrm{u_{31} X^3_{N/L}} + \mathrm{u_{32} X^2_{N/L} Y_{N/L}} \\
&+ \mathrm{u_{33} X_{N/L} Y^2_{N/L}} \\
&+ \mathrm{u_{34} Y^3_{N/L}}
\end{aligned}
\tag{4.2}
$$

where $\mathrm{X_{N/L}}$, $\mathrm{Y_{N/L}}$ denote the horizontal and vertical positions in $\mathrm{MWPC_N}$ (^{7}Be, ^{8}B) and $\mathrm{MWPC_L}$ (proton), respectively. $\mathrm{X_{N/L}}$, $\mathrm{Y_{N/L}}$ and the variables $\mathrm{X_{SSD}}$, $\mathrm{Y_{SSD}}$ will be discussed in the next subsection.

In order to find the coefficients $\mathrm{u_i}$ one should solve the classical minimization problem for the measured MWPC and SSD positions and the corresponding momenta. However, due to energy and angular straggling on the layers of matter downstream from the target (see Table 3.2) an experimental calibration of the momentum is not possible. Instead, tracking of particle trajectories is necessary.

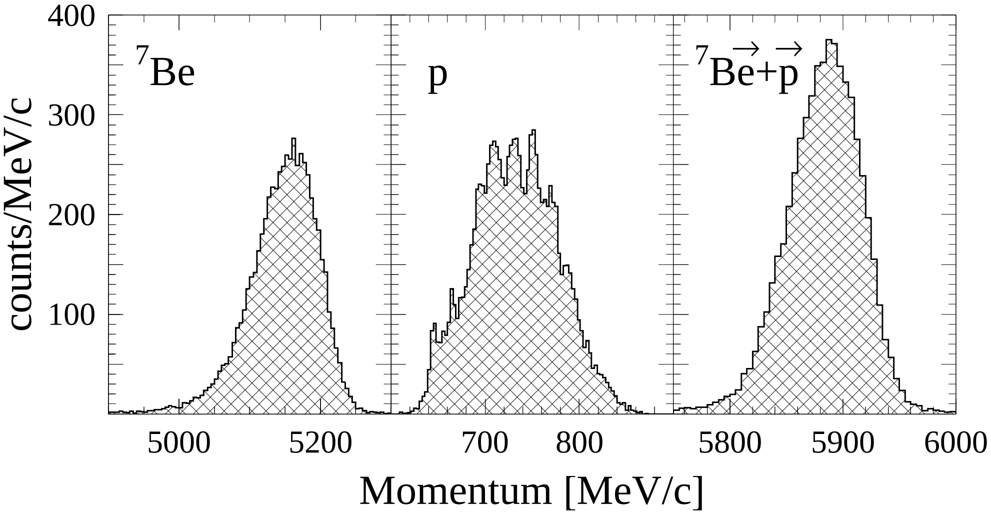

Figure 4.9: *Momenta of the break-up particles (the obviously puzzling structure of the proton momentum will be explained in Section 4.6.1). The p_B-momentum is reconstructed from the absolute momenta p_{Be} and p_p and the information about the reaction opening angle θ_{17}.*

This is done in a Monte Carlo simulation with the code GEANT [Gia94] (see Section 4.9). The atomic effects in the materials are different for the proton and ^{7}Be so one should reconstruct the trajectories of these particles separately. The precision of the reconstruction can be judged by investigating the distribution $(\mathrm{p_{fit}} - \mathrm{p_0})/\mathrm{p_0}$. In case of protons we get RMS=0.5%, ^{7}Be yields RMS=0.3%.

With the calculated coefficients one can derive now, from the detector positions, the momenta of the break-up products. Their spectra and the vectorial sum, the momentum of ^{8}B, are shown in Fig. 4.9. Table 4.8 contains the mean values and the widths (1σ) of the momentum distributions, compared to the GEANT simulation. It is noticeable that the spread of ^{8}B-momentum is reduced compared to that of ^{7}Be and proton. It is due to the convolution with the experimental resolution which makes the spreads of the component vectors partially cancel out.

[MeV/c]	^{7}Be	proton	^{8}B
DATA	5144 ± 49	742.3 ± 37.3	5886 ± 32
GEANT	5133 ± 40	744.9 ± 34.0	5877 ± 27

Table 4.8: *Peaks of the measured momentum distributions and their 1σ-spreads in units of MeV/c.*

In reconstructing the experimental momentum of ^{8}B the recoil of the ^{208}Pb target is disregarded because, according to the simulation, it is negligible (^{208}Pb is much heavier than ^{8}B).
It is worth mentioning that the momentum of ^{8}B at the center of the lead target, as found from the analysis of the magnetic rigidity (Table 3.1), amounts to 5888±26 MeV/c, which is a good consistency-check for the momentum calibration.

4.4.1 Measuring positions in space

In the following the measurement of positions in the active detectors is discussed. As we remember, four SSD are assembled in the pipe downstream from the target. They are centered along the beam axis with an estimated precision of 1mm i.e. 10 strips. Unfortunately this precision cannot be better since there is no way to introduce any checking technique (e.g. laser) – at least one end of the pipe is unavailable for manipulation. Using the beam to determine possible offsets on SSD is only possible under the assumption the beam is (constantly) centered and aligned with the optical axis. This information, however, is unavailable from the detectors which are to be calibrated. Instead, the beam spot at the target is reconstructed by drawing the ratio of ^{7}Be from the break-up to the number of the impinging ^{8}B (Fig. 4.3).
In fact, only relative offsets must be determined

$$\begin{aligned} X_{SSD}(i) =& (SSD3_X(i) + \text{offset}_3) - (SSD1_X(i) + \text{offset}_1) \\ =& SSD3_X(i) - SSD1_X(i) + \text{offset}_X \\ Y_{SSD}(i) =& (SSD4_Y(i) + \text{offset}_4) - (SSD2_Y(i) + \text{offset}_2) \\ =& SSD4_Y(i) - SSD2_Y(i) + \text{offset}_Y \end{aligned} \tag{4.3}$$

which limits the systematic errors of the measurement.
Now, since the dimension ($X \times Y = 32 \times 24$ mm^2) and the position of the ^{208}Pb-target is known (the target can, from the technical point of view, be more precisely positioned in the pipe), we can align it with the beam spot i.e. center the beam between the target frames by manipulating the relative offsets. The resulting angles are natural constraints of the method – projections along the optical axis cannot lead to positions outside the beam tube.
The aluminum frame is clearly visible because of the enhancement in the reaction rate (Fig. 4.3). The Y-profile has well pronounced 'edges' as the vertical spread of the incident beam is wider than the target Y-dimension. Owing to the cross-section profiles we can fix the relative offsets of SSD. The numerical values are listed in Table 4.9.
As an independent method to determine the Y-offsets one can take advantage of the optical properties of KaoS and plot the Y-position at the target (deduced from SSD) against the Y-position in $MWPC_N$. In the first order the points

should lie on a straight line with the slope given by the Y-magnification of the spectrometer [Bou99]. This information also sets the Y-offsets and yields results [Bou99] close to the method presented here.

Now let us pay attention to measuring positions with MWPC. MWPC are placed not far from the focal plane of the spectrometer and in first order the position measured along the dispersion direction corresponds directly to the absolute momentum. This feature can be used to check the momentum calibration. For that purpose two sweep runs were performed. This was done as follows:
Beams with a fixed energy (^{12}C of 100 MeV/u directly from SIS, ^{8}B of 261 MeV/u from FRS) ran through the spectrometer whose magnetic field was changed in steps. Magnitudes of the steps were calculated in order to hit all the 30 plastic F-paddles. Due to its magnetic rigidity and a maximum dipole field in KaoS of 1.95 Tm, with the ^{8}B-beam it was possible to cover only the 'heavy-ion' range (paddles 16-30) while ^{12}C swept also the 'proton' range (1-15) hence the full space.
The measured hit positions in MWPC were compared with those from the simulation. This revealed discrepancies, which were not encountered in the focal plane of the spectrometer – for all the field magnitudes there was good correspondence between the simulated and the measured pattern from the F-paddles. In order to explain the disagreement in case of MWPC we proved that:
– the tracking engine of GEANT (above all the energy-loss procedure) is correct,
– the beam energy in front of the spectrometer agrees with the nominal energy, measured at FRS/SIS (i.e. additional layers of matter in the beam are not present).
We found that the KaoS' magnetic-field in GEANT is not precise enough (as far as the out-of-the-focal-plane positions are concerned). In spite of the 3-dim measurement of the field with a Hall probe (page 58) the fringe fields of the spectrometer are very complicated for the mapping. The proper check of the momentum calibration would be a run with a fixed magnetic field (with magnitude equal to the experimental one, 1.54 T) with the energy changed in steps. It would fully correspond to the experimental condition of particles of various energies running in the field of one constant magnitude.

In order to apply the momentum calibration from GEANT to the experimental data it was necessary to recalibrate the measured MWPC positions to match them to the simulated ones. It was found that besides plain offsets small slopes were needed. The 'proper' correspondence data-simulation was obtained with the linear function

$$\begin{aligned} \mathrm{X_N} =& \mathrm{slope_{NX}} \cdot \mathrm{MWPCN_X} + \mathrm{offset_{NX}} \\ \mathrm{Y_N} =& \mathrm{MWPCN_Y} \\ \mathrm{X_L} =& \mathrm{slope_{LX}} \cdot \mathrm{MWPCL_X} + \mathrm{offset_{LX}} \\ \mathrm{Y_L} =& \mathrm{MWPCL_Y} \end{aligned} \tag{4.4}$$

where $\mathrm{MWPCN_X}$, $\mathrm{MWPCL_X}$ [cm] are obtained from the known mapping of a wire number to a nominal position in MWPC-N and MWPC-L, respectively. Numerical values for the calibration of the measured positions are listed in Table 4.9.

SSD	$\mathrm{offset_X}$	+1.15 mm	$\mathrm{offset_Y}$	–0.40 mm
$\mathrm{MWPC_N}$	$\mathrm{slope_{NX}}$	+1.0644	$\mathrm{offset_{NX}}$	–1.4333 cm
$\mathrm{MWPC_L}$	$\mathrm{slope_{LX}}$	+1.0483	$\mathrm{offset_{LX}}$	–3.1298 cm

Table 4.9: *Constants of the position calibration.*

For the completeness of the description the other component of the invariant mass (besides the momenta shown in Fig. 4.9), the opening angle θ_{17}, is shown in Fig. 4.10, as measured from the SSD positions.
Finally, the invariant mass spectrum is presented in Fig. 5.1 in Chapter 5.

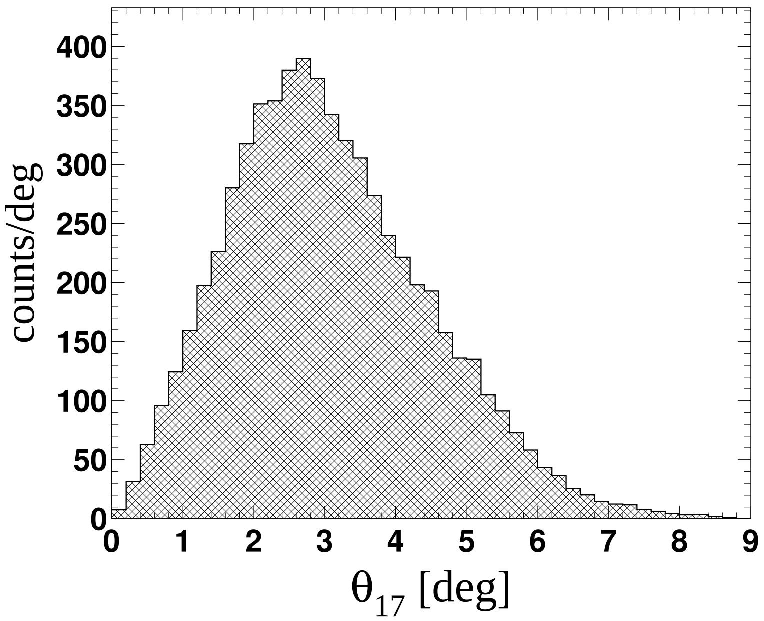

Figure 4.10: *Angle θ_{17} between the outgoing break-up partners, p and ^{7}Be.*

4.5 Accuracy of the invariant mass determination

The invariant mass spectrum depends on the momentum calibration, and therefore is biased by the selection of the offsets to the spatial positions of the detectors. In Section 4.4.1 it was determined
(i) the SSD offsets by the cross-section 'image' of the target and
(ii) the MWPC slopes and offsets by analyzing the sweep runs.
It is important to check how different values of these coefficients affect the momentum calibration and hence the invariant mass distribution. Several calculations were performed in which different values of offsets entered into the momentum calibration. The criteria for selecting only the 'reasonable' values were as follows:
–the beam is not necessarily centered at the target position, however new offsets cannot result in projections along the optical axis outside the beam pipe,
–in case of MWPC, the sweep run with primary ^{12}C is used alternatively to deduce the slopes and offsets of both $MWPC_L$ and $MWPC_N$ (as a standard I use the sweep run with secondary ^{8}B to calibrate $MWPC_N$ of the 'heavy-ions' momentum range).
For each calibration the spectrum of the invariant mass was calculated and its consistency was checked with the incident beam energy (mean momentum vec-

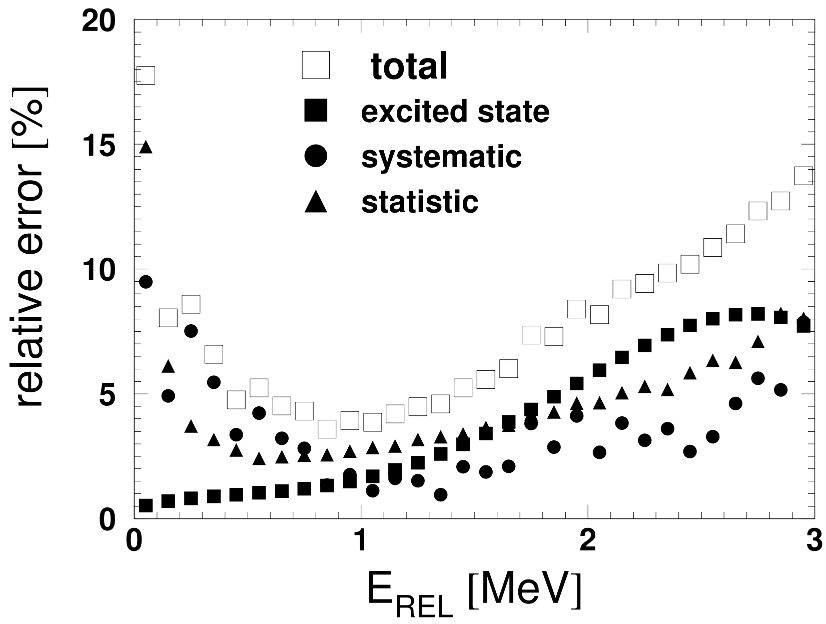

Figure 4.11: *Relative error of the CD differential cross-section vs. the relative energy.*

tor of ^{8}B). Different calibrations result in a different yield of counts for a given E_{REL}-bin so an envelope of counts arises. This envelope is taken as the systematic uncertainty (systematic error) of the invariant mass. Recall that the invariant mass spectrum is obtained as it is discussed in Section 4.4.

Since the probability to find a given number of counts in a relative energy interval is given by the Poisson distribution, the statistic error (variance) is taken as the square root of the measured yield. The relative statistic error is then $\delta_{STAT} = 1/\sqrt{\text{yield}}$.

Correction for feeding the first excited state in ^{7}Be (discussed further in Section 4.8) introduces the uncertainty derived from the RIKEN experiment (see Table 4.11).

The above-mentioned relative errors are presented in Fig. 4.11. Added quadratically they yield the total relative error, which increases towards low and high relative energy and is minimum around $E_{REL} = 1$ MeV. It is used in Chapter 5 to determine error bars of the measured yields in the relative-energy bins.

4.6 Efficiency

4.6.1 Trigger efficiency

The proton momentum is reconstructed in Fig. 4.9. We can see a structure of separate peaks in the momentum spectrum. This obviously puzzling effect demonstrates a reduction in the trigger efficiency. The GEANT simulation revealed two reasons of the phenomenon connected with the trigger detector FD:
1) FD consists of 30 single plastic paddles (not a continuous wall) which do not cover fully the focal plane of the spectrometer. This is due to the orientation of FD which is not along the focal plane (as for the usual measurement) but has been changed in order to give space for the two MWPC (see Fig. 3.2). The particles running through the slits do not trigger and these events are lost.
2) When the thresholds on the FD paddles are set too high a fraction of particles with signals in FD below the threshold is rejected.
The two effects do not affect the heavy ions ^{7}Be and ^{8}B, but only the CD-protons due to their spatial coverage of FD and relatively low energy-loss in plastic. It means that only the number of TR_{pBe}-events is subject to the trigger-efficiency correction whereas TR_{BEAM} (scaled down) is not effected.
Both effects lead to the characteristic structure in the proton momentum in Fig. 4.9.
The trigger efficiency is deduced as follows. The constant-fraction threshold of each plastic paddle is determined by measuring the proton peak position and its cut in the FD energy-loss spectrum. Then the thresholds are applied into the GEANT simulation and the agreement between the experimental and simulated proton-momentum distribution is checked. Ratio of the simulated events with- and without FD energy-loss cuts gives the overall number

$$\varepsilon^{\mathrm{TR}} = 95.0\% \pm 0.5\%$$

It turns out that the events which are lost due to the trigger inefficiency are distributed homogeneously over the invariant-mass spectrum (E_{REL}). It is not strange since, in spite of only selected (not all) proton momenta which are lost (those corresponding to the positions on the edges of the plastic paddles), a number of combinations in constructing E_{REL} is available (the reaction opening angle plays a role).

4.6.2 Geometrical efficiency

Beyond the geometrical acceptance of the spectrometer no data can be measured. Fortunately, due to the kinematics of CD at 254 MeV/u the break-up particles are focused in the forward angles and only a small fraction of all the CD events is lost.

The geometrical efficiency correction (involving the geometrical acceptance) has to rely on the GEANT simulation. In order to avoid uncertainties in determination of the real conditions close to the geometrical limits of the detectors the same 'safety' cuts are introduced to the measured data and simulation.
The structure and assembly of the active detectors in the setup of the KaoS spectrometer was described in Chapter 3. Here the crucial features of the active detectors, responsible for the cuts applied, are underlined.

Each SSD has 576 strips (1 strip=0.1 mm). Since not enough GASSIPLEX chips were available the full readout of SSD was limited to 1-480 strips. In the range 481-544 every other strip was connected while within 545-576 there were dead strips. To remove ambiguities in determining the cross-talk signals collected within strips 481-544 they were cut out. The active part of SSD is then (SSD4 is placed upside down in the common reference system)

$$
\begin{aligned}
-2.88\,\mathrm{cm} &< \mathrm{SSD1_X} < 1.92\,\mathrm{cm}\\
-2.88\,\mathrm{cm} &< \mathrm{SSD2_Y} < 1.92\,\mathrm{cm}\\
-2.88\,\mathrm{cm} &< \mathrm{SSD3_X} < 1.92\,\mathrm{cm}\\
-1.92\,\mathrm{cm} &< \mathrm{SSD4_Y} < 2.88\,\mathrm{cm}
\end{aligned}
$$

This cut rejects particles with large angles. This affects mostly the CD-protons, being the light particles with wide angular spread around the spatially focused ^{7}Be partners.

In a similar way the distributions in MWPC were examined. The dispersive X-direction was cut about 0.5 cm from the edges to let the peak-finding routine to determine the position from not distorted (cut off) signal distribution on the wires. The same was applied to the Y-direction of both MWPC (mostly the case of large θ_{17}-angles)

$$
\begin{aligned}
-60.0\,\mathrm{cm} &< \mathrm{X_N} < 60.0\,\mathrm{cm}\\
-15.5\,\mathrm{cm} &< \mathrm{Y_N} < 16.5\,\mathrm{cm}\\
-26.0\,\mathrm{cm} &< \mathrm{X_L} < 30.0\,\mathrm{cm}\\
-12.0\,\mathrm{cm} &< \mathrm{Y_L} < 13.5\,\mathrm{cm}
\end{aligned}
$$

As for SSD, the cuts on MWPC affect solely the CD-protons; MWPC-N is large enough to measure the whole ^{7}Be distribution.

4.6.3 Double-hits cut-off

Due to cross-talks between neighboring strips it is impossible to detect in SSD two particle peaks separated by not more than three strips. This leads to a cut-off in the SSD positions

$$\begin{array}{ll} \mathrm{SSDi_X(Be)} - \mathrm{SSDi_X(p)} > 3\,\mathrm{strips} & \mathrm{i} = 1,3 \\ \mathrm{SSDi_Y(Be)} - \mathrm{SSDi_Y(p)} > 3\,\mathrm{strips} & \mathrm{i} = 2,4 \end{array}$$

This minimum separation of hits in SSD clearly cuts events with very small opening angles between p and ^{7}Be, θ_{17}. This prevents double hits which would introduce uncertainty in the precise determination of both the particle positions and the identification of the particles themselves ($\Delta E^{\mathrm{ion}}_{\mathrm{SSDi}}$). The small-opening-angle cut-off yields

$$\varepsilon^{\theta_{17}} = 95.97\% \pm 0.15\%$$

and is a function of the relative energy.

4.6.4 Transmission through the layers of matter

Probability to interact with materials of the setup must be taken into account to correct for absorption of particles in the layers of matter (Table 3.2). The parameterization of Kox *et al.* [Kox87] for the measured total reaction cross-section is used. The calculated transmission for ^{7}Be is of 98.90%, for protons it is of 99.52%. In case of ^{8}B a value of 98.74% is found. The total transmission up to FD is then 98.90% × 99.52%/98.74% yielding

$$\varepsilon^{\mathrm{ABS}} = 99.68\% \pm 0.20\%$$

4.6.5 Total efficiency

In addition to the efficiency from the aforementioned effects, a constant factor of 1.0032 is taken as a correction for accidental coincidences between $\mathrm{TR_{pBe}}$ and $\mathrm{TR_{BEAM}}$. The efficiency curve is shown in Fig. 4.12. As we can see, the experimental efficiency is pretty high. This is due to the high detection efficiency of the heavy, charged ions and the geometrical acceptance of the setup at the KaoS spectrometer. A peak efficiency of about 70% is reached at medium values of the relative energy. The observed fall towards low $\mathrm{E_{REL}}$ is caused by the small-θ_{17} cut-off while the decrease in efficiency towards high $\mathrm{E_{REL}}$ is due to the finite geometrical acceptance of the detectors. The same cuts are applied to the measured data which reduces the statistics by about 35% but allows keeping the experimental conditions under control i.e. makes the determined cross-section less uncertain.

cuts applied	remaining events
geometrical acceptance	37357
& active Pb-target	33659
& trigger efficiency	31977
& geometrical 'safety' cuts	25017
& $\theta_{17} > 3$ strips	24010

Table 4.10: *Reduction in the statistics of the break-up events through the efficiency cuts. The cuts are meant to be 'AND-ed' from top to bottom of the table.*

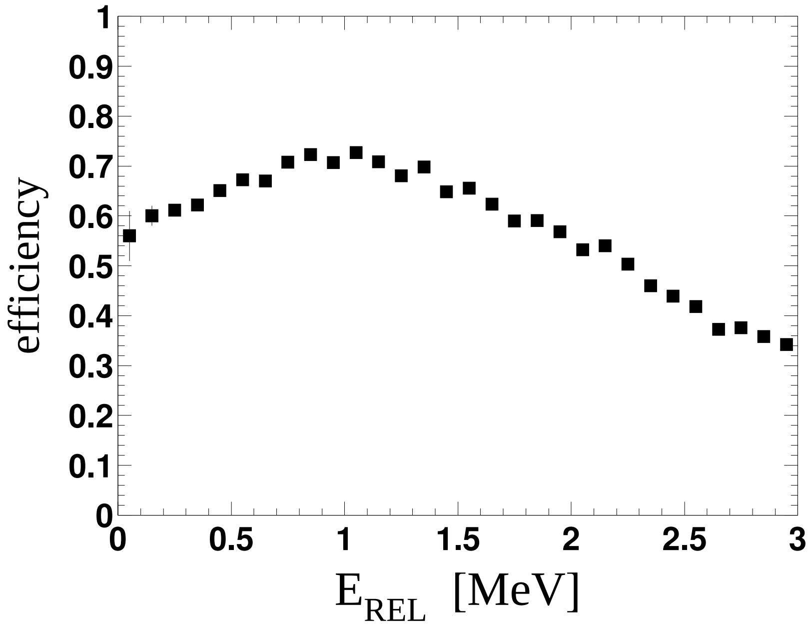

Figure 4.12: *Total efficiency as a function of the relative p-^{7}Be energy, E_{REL}.*

4.7 Resolution

For the determination of the invariant mass the momenta of the break-up partners and the reaction opening angle are measured. The opening angle is calculated from the measured positions in SSD. The intrinsic angular resolution of the system of four SSD (in two pairs) amounts to 2.8 mrad which takes into account cross-talks between neighboring strips. In fact, due to angular straggling, the opening angle resolution amounts to σ=4.8 mrad.
Resolution of the momentum determination i.e. calibration from the measured positions to the absolute momentum is σ_p/p=0.5% for the proton and σ_p/p=0.3% in case of ^{7}Be.
Resolution as a function of the relative energy between the fragments can be deduced only from the GEANT Monte Carlo simulation of the setup. For that purpose, the CD-break-up with a sharp, monoenergetic E_{REL} is generated with good statistics and then the invariant mass is reconstructed from the measured positions on the active detectors. The 1σ-widths of the measured Gaussian-like E_{REL}-distributions are shown in Fig. 4.13. When the energy unit is keV, a func-

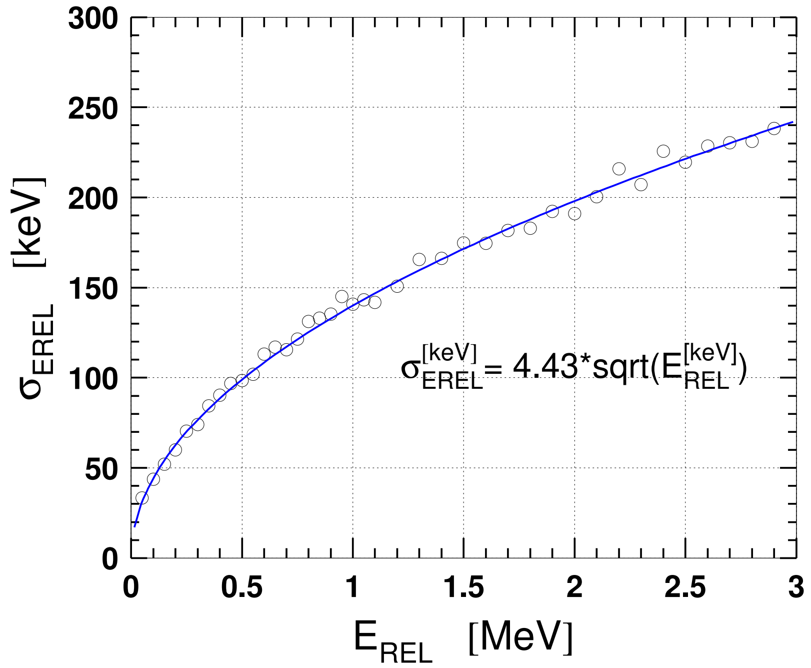

Figure 4.13: *Resolution of the invariant-mass determination for the 200 mg/cm^2-thick lead target.*

tion of the form $\sigma_{\mathrm{EREL}} = 4.43 \cdot \sqrt{\mathrm{E_{REL}}}$ appears to be a global fit to the points. As we can see the resolution is really the limiting factor of the experiment. It is due to the multiple Coulomb scattering in the materials of the setup, mainly the 200 mg/cm^2-thick lead target. It is worth mentioning that for the intensity of the secondary ^{8}B-beam which was available (see Chapter 3) a thinner target would not yield enough statistics.

In order to compare the measured data with other results or theory the latter must be folded with the experimental resolution. It should be stressed that the GEANT simulation is of great importance as the only tool for the resolution determination. The Monte Carlo apparatus-distorted events carry the whole information on the undistorted input variables which, in our case, are energy dependences of the S_{17}-factor for the E1 and M1 transitions (see Section 4.9). The unfolded experimental S_{17}-factors are found by comparing the simulated and the measured yield. Such method of deconvolution [Lin95] is efficient, faithful and binning free (see [Sur98] for a study). Finally, for comparison with other data, the determined S_{17}-factor is presented in the binning of the resolution.

4.8 Dissociation to the excited state in ^{7}Be

The nuclear structure of ^{7}Be is shown in Fig. 2.4. We can see an excited $\frac{1}{2}^-$ state at 429 keV. The Coulomb break-up $^8\mathrm{B} \to {}^7\mathrm{Be} + \mathrm{p}$ can proceed to the ground state of ^{7}Be both directly and through the $\frac{1}{2}^-$ level, followed by emission of 429 keV γ-rays. This is depicted schematically in Fig. 4.14.

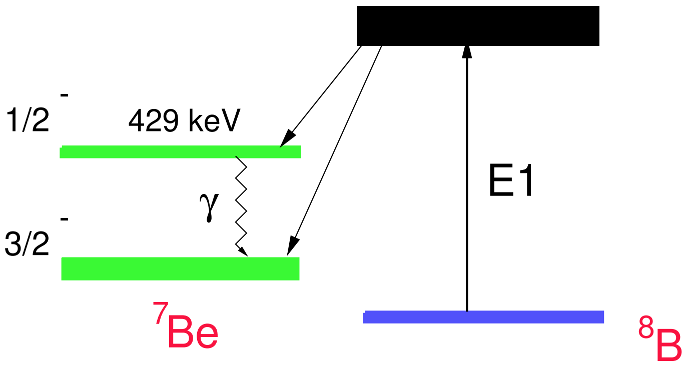

Figure 4.14: *Scheme of the branching in ^{7}Be.*

Considering Formula 2.36 the branching ratio of the process, in case of the dipole transitions, can be expressed as

$$\mathrm{R} = \frac{\sigma^{\mathrm{ex}}}{\sigma^{\mathrm{gs}}} = \left(\frac{\mathrm{E}_\gamma}{\mathrm{E}_\gamma + \mathrm{E}_{\mathrm{ex}}}\right)^3 \frac{\mathrm{n}_{\mathrm{E1}}^{\mathrm{ex}}}{\mathrm{n}_{\mathrm{E1}}^{\mathrm{gs}}} \frac{(2\mathrm{I}_{\mathrm{Be}^*}+1)}{(2\mathrm{I}_{\mathrm{Be}}+1)} \frac{\mathrm{S}_{17}^{\mathrm{ex}}}{\mathrm{S}_{17}^{\mathrm{gs}}} \tag{4.5}$$

where $\mathrm{E}_\gamma = \mathrm{E}_{\mathrm{REL}} + \mathrm{Q}$ (the Q-value is 137 keV), $\mathrm{E}_{\mathrm{ex}} = 429$ keV, $\mathrm{I}_{\mathrm{Be}^*} = \frac{1}{2}$, $\mathrm{I}_{\mathrm{Be}} = \frac{3}{2}$, n_{E1} denotes the E1 equivalent photon number, and $\mathrm{S}_{17}^{\mathrm{gs}}$ ($\mathrm{S}_{17}^{\mathrm{ex}}$) is the astrophysical factor, assumed for simplicity to be proportional to the respective spectroscopic factor [Coh67].

The calculated branching ratio is presented in Fig. 4.15 by the solid line.

In the experiment of RIKEN the 429 keV γ-rays were measured in coincidence with the ^{8}B break-up partners to correct for feeding the first excited state in ^{7}Be [Iwa96, Kik98b]. We use the RIKEN results for necessary correction of our data to extract the astrophysical S_{17}-factor from the ^{8}B-CD process exclusively to the ground state of ^{7}Be. Since the RIKEN and GSI CD-experiments have been performed at different ^{8}B-beam energies the measured ratio must be readjusted from 50 MeV/u to 250 MeV/u-equivalent photon fluxes (Formula 2.101) to suit the kinematics of the GSI experiment

$$\mathrm{R}_{\mathrm{GSI}} = \left(\frac{\mathrm{n}_{\mathrm{E1}}^{\mathrm{ex}}}{\mathrm{n}_{\mathrm{E1}}^{\mathrm{gs}}}\right)_{250\mathrm{MeV/u}} \cdot \left(\frac{\mathrm{n}_{\mathrm{E1}}^{\mathrm{gs}}}{\mathrm{n}_{\mathrm{E1}}^{\mathrm{ex}}}\right)_{50\mathrm{MeV/u}} \cdot \mathrm{R}_{\mathrm{RIKEN}} \tag{4.6}$$

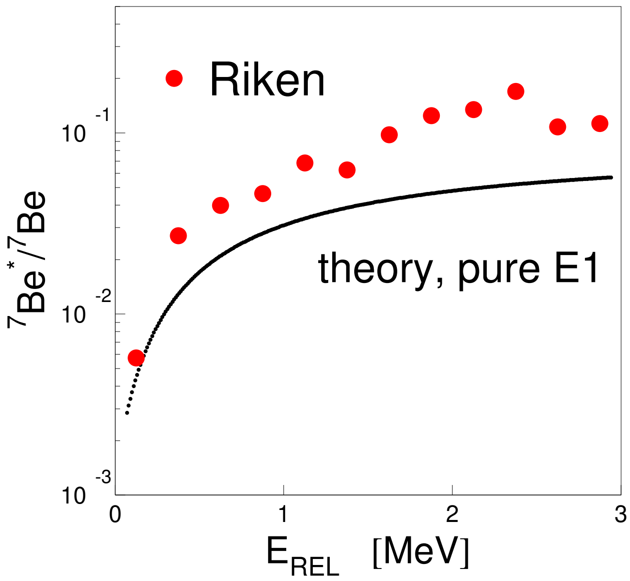

Figure 4.15: *Branching ratio for feeding the first excited state in ^{7}Be, as measured in the RIKEN experiment (block points). The full theoretical curve is explained in the text.*

The latter is true under the assumption that only the E1 transitions contribute.

Finally the measured cross-section must be multiplied by the factor $1/(1 + \mathrm{R_{GSI}})$ to obtain the cross-section to the ground state. The effect is negligible at low $\mathrm{E_{REL}}$ and maximum at about 2.4 MeV (see Fig. 4.15). Alternatively, the simulated ground-state yield is corrected by $(1+\mathrm{R_{GSI}})$ to compare it with the measured CD data. The numerical values and their uncertainties [Iwa96, Kik98b] are presented in Table 4.11.

$\mathrm{E_{REL}}$	$(1+\mathrm{R_{GSI}})$	$\mathrm{E_{REL}}$	$(1+\mathrm{R_{GSI}})$	$\mathrm{E_{REL}}$	$(1+\mathrm{R_{GSI}})$
0.0-0.1	1.003 ± 0.005	1.0-1.1	1.066 ± 0.017	2.0-2.1	1.162 ± 0.060
0.1-0.2	1.011 ± 0.007	1.1-1.2	1.072 ± 0.019	2.1-2.2	1.178 ± 0.065
0.2-0.3	1.018 ± 0.008	1.2-1.3	1.079 ± 0.022	2.2-2.3	1.195 ± 0.069
0.3-0.4	1.025 ± 0.009	1.3-1.4	1.086 ± 0.026	2.3-2.4	1.214 ± 0.074
0.4-0.5	1.031 ± 0.010	1.4-1.5	1.094 ± 0.030	2.4-2.5	1.194 ± 0.077
0.5-0.6	1.037 ± 0.010	1.5-1.6	1.103 ± 0.034	2.5-2.6	1.158 ± 0.080
0.6-0.7	1.043 ± 0.011	1.6-1.7	1.113 ± 0.039	2.6-2.7	1.132 ± 0.082
0.7-0.8	1.049 ± 0.012	1.7-1.8	1.123 ± 0.044	2.7-2.8	1.134 ± 0.082
0.8-0.9	1.054 ± 0.013	1.8-1.9	1.135 ± 0.049	2.8-2.9	1.137 ± 0.081
0.9-1.0	1.060 ± 0.015	1.9-2.0	1.148 ± 0.054	2.9-3.0	1.137 ± 0.077

Table 4.11: *Numerical values of the total to the ground-state cross-section ratio, $(1 + R_{GSI})$, and their accuracy.*

4.9 GEANT simulation

A Monte Carlo simulation using the program packet GEANT [Gia94] was prepared and run for the momentum calibration in order to reconstruct the invariant mass and for evaluating the detection efficiencies and the resolution.
GEANT is a simulation tool containing all relevant cross-sections for atomic interactions in matter: energy-loss due to ionization, multiple Coulomb scattering etc., and allowing tracking of particles in a magnetic field.
The energy-loss calculation in GEANT is performed according to the particle 'tracking type'. This determines all the physical processes the particle undergoes, hence is crucial for a reliable simulation. For ^{7}Be and ^{8}B the 'heavy-ion' tracking was used. In order to check the procedure, the energy-loss on the experimental layers of matter was calculated in ATIMA [Gei98]. Good consistency was found (within 98%) which means that the computing engine of GEANT is appropriate (see [Las95]).
The magnetic field of the KaoS spectrometer was mapped into GEANT as a matrix of the measured maximum magnetic field intensity for all the coordinate points (Section 3.2.1).
The Monte Carlo generator of the simulated process is explained in the section below.

4.9.1 Kinematics of the event

There exists an invariant quantity in the collision system $^8\mathrm{B} +^{208}\mathrm{Pb}$

$$\mathrm{s} = (\mathrm{p_B} + \mathrm{p_{Pb}})^2 \tag{4.7}$$

where p denotes a four-momentum.
By expressing this quantity in the laboratory (LAB)

$$\mathrm{s} = \mathrm{m_{Pb}^2} + \mathrm{m_B^2} + 2\mathrm{m_{Pb}}\mathrm{E_B^{LAB}} \equiv \mathrm{inv.} \tag{4.8}$$

we see that this is the total energy available to the process, where $\mathrm{E_B^{LAB}} = \sqrt{\mathrm{m_B^2} + \mathbf{p}_\mathrm{B}^2} = \mathrm{m_B} + \mathrm{T_B^{LAB}}$ and T denotes kinetic energy and m denotes rest mass.

For the transformation **(1)** in Fig. 4.16 we have the velocity of the Coulomb dissociation system ($\mathrm{CM_{CD}}$) in LAB

$$\boldsymbol{\beta}_1 = \frac{\mathbf{p}_\mathrm{B}^\mathrm{LAB}}{\mathrm{m_{Pb}} + \mathrm{T_B^{LAB}}} \tag{4.9}$$

or alternatively

$$\gamma_1 = \frac{\mathrm{E_B^{LAB}} + \mathrm{m_{Pb}}}{\mathrm{E_{TOTAL}^{CM_{CD}}}} = \frac{\mathrm{E_B^{LAB}} + \mathrm{m_{Pb}}}{\sqrt{\mathrm{s}}} \tag{4.10}$$

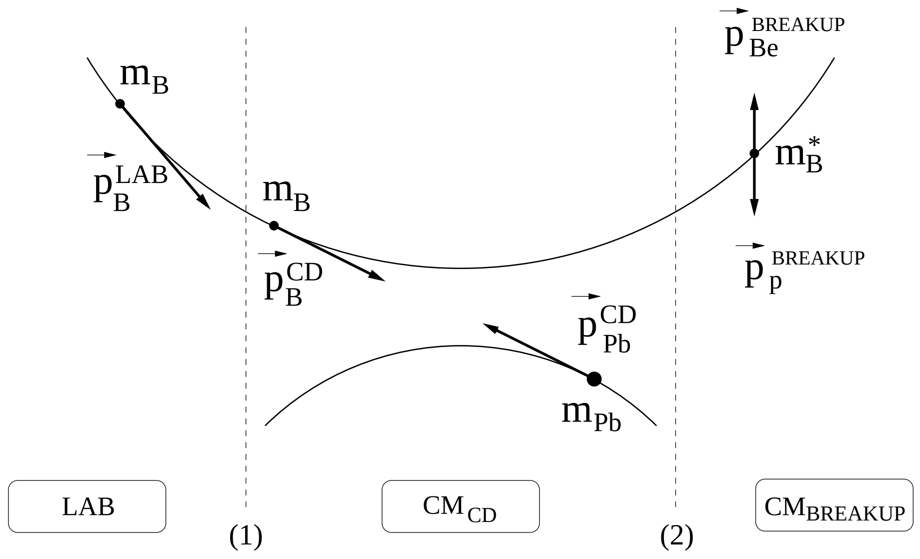

Figure 4.16: *Kinematics of the collision studied.*

The momentum vector of ^{8}B in CM_{CD} can be obtained from the conditions

$$\begin{cases} |\mathbf{p}_B^{CM_{CD}}| = |\mathbf{p}_{Pb}^{CM_{CD}}| \\ \sqrt{s} = \sqrt{m_{Pb}^2 + (\mathbf{p}_{Pb}^{CM_{CD}})^2} + \sqrt{(m_B^*)^2 + (\mathbf{p}_B^{CM_{CD}})^2} \end{cases} \tag{4.11}$$

and one gets

$$|\mathbf{p}_B^{CM_{CD}}| = |\mathbf{p}_{Pb}^{CM_{CD}}| = \frac{\{[s - (m_{Pb} + m_B^*)^2][s - (m_{Pb} - m_B^*)^2]\}^{1/2}}{2\sqrt{s}} \tag{4.12}$$

We note that m_B^* describes the rest mass of ^{8}B plus the excitation energy gained through the Coulomb interaction with the heavy target ^{208}Pb.

For the motion of $CM_{BREAKUP}$ in CM_{CD} **(2)** one has

$$\gamma_2 = \frac{m_B^* + T_B^{CM_{CD}}}{m_B^*} \tag{4.13}$$

The momenta of ^{7}Be and proton in $CM_{BREAKUP}$ are obtained from the analogous to Eq. 4.11 conditions

$$\begin{cases} |\mathbf{p}_{Be}^{CM_{BR}}| = |\mathbf{p}_p^{CM_{BR}}| \\ m_B^* = \sqrt{m_{Be}^2 + (\mathbf{p}_{Be}^{CM_{BR}})^2} + \sqrt{m_p^2 + (\mathbf{p}_p^{CM_{BR}})^2} \end{cases} \tag{4.14}$$

The result is

$$|\mathbf{p}_{\mathrm{Be}}^{\mathrm{CM_{BR}}}| = |\mathbf{p}_{\mathrm{p}}^{\mathrm{CM_{BR}}}| = \frac{\{[(\mathrm{m_B^*})^2 - (\mathrm{m_{Be}} + \mathrm{m_p})^2][(\mathrm{m_B^*})^2 - (\mathrm{m_{Be}} - \mathrm{m_p})^2]\}^{1/2}}{2\mathrm{m_B^*}} \tag{4.15}$$

The Q-value of the reaction, 137 keV, is the minimum excitation energy that must be available for the break-up event to occur. We see this explicitly from

$$\mathrm{m_B^*} = \mathrm{m_B} + \mathrm{E^*} = \mathrm{m_{Be}} + \mathrm{m_p} - \mathrm{Q} + \mathrm{E^*} = \mathrm{m_{Be}} + \mathrm{m_p} + \mathrm{E_{REL}} \tag{4.16}$$

In other words the relative energy of the break-up partners, ^{7}Be and proton, must be $\mathrm{E_{REL}} > 0$.

In each of the above systems the components of the momenta are found with the respective Lorentz transformation

$$\begin{pmatrix} \mathrm{E^{CM}} \\ \mathbf{p}_{\parallel}^{\mathrm{CM}} \end{pmatrix} = \begin{pmatrix} \gamma & -\gamma\beta \\ -\gamma\beta & \gamma \end{pmatrix} \begin{pmatrix} \mathrm{E^{LAB}} \\ \mathbf{p}_{\parallel}^{\mathrm{LAB}} \end{pmatrix} \qquad \mathbf{p}_{\perp}^{\mathrm{CM}} = \mathbf{p}_{\perp}^{\mathrm{LAB}} \tag{4.17}$$

For simulating the Coulomb dissociation of ^{8}B the ^{8}B excitation energy is distributed in a way proportional to the probabilities of the relevant electromagnetic transitions i.e. to the respective EM matrix-elements . This is equivalent, as we have seen in Section 2.2 where we related the CD process to the direct-capture reaction, to calculating/assuming the energy dependences of the respective S-factors.

So, the ^{8}B Coulomb break-up is simulated here according to Eq. 2.36. Explicit formulae for the equivalent photon numbers are given by Eq. 2.101. The necessary input S-factors are taken either from the experimental data: the E1-dependence from the data sets of Filippone [Fil83] and Vaughn [Vau70], the M1 resonance ($\mathrm{E_{REL}}$=632 keV) as a Lorentzian fitted to the data of Filippone, or from model calculations (e.g. [Ber96c, Ber98]).
As a final goal, by comparing the simulated and the measured yields, the $\mathrm{S_{17}}$ astrophysical factor is determined, which is discussed in Chapter 5.

Chapter 5

Results

5.1 CD differential cross-section

The aim of this work was to measure the cross-section $d\sigma_{CD}/dE_{REL}$ for the Coulomb break-up process $^8B \rightarrow {}^7Be + p$, as a function of the p-Be relative energy. It is calculated as follows

$$\frac{d\,\sigma_{CD}}{dE_{REL}}(E_{REL}) = \frac{N_{CD}(\Delta E_{REL})}{\Delta E_{REL}} \times \frac{1}{N_{Pb} \cdot N_B} \times \frac{1}{\varepsilon^{CD}} \times \frac{1}{\varepsilon^{DT}} \times \frac{1}{\varepsilon\,(E_{REL})} \tag{5.1}$$

where

$\frac{N_{CD}(\Delta E_{REL})}{\Delta E_{REL}}$	is the measured yield of the CD events within a relative-energy bin
$N_{Pb} \cdot N_B$	is the product of the number of the target atoms and the number of the beam particles, in terms of mb^{-1} (Section 4.2.3)
ε^{CD}	is the analysis efficiency to find the CD events (Section 4.3.3)
ε^{DT}	is the correction for the dead time of the acquisition system (Section 4.1.2)
$\varepsilon\,(E_{REL})$	is the efficiency correction involving components derived in Section 4.6 (geometrical efficiency, trigger efficiency, low-θ_{17}, cut-off, correction on the transmission losses). The resulting efficiency curve is shown in Fig 4.12.

In Fig. 5.1 the experimental yield i.e. the product $\frac{d\sigma_{CD}}{dE_{REL}} \times \varepsilon\,(E_{REL})$, where $\varepsilon(E_{REL})$ is the last component of the efficiency correction in Formula 5.1, is presented. We note that the M1-resonance at $E_{REL} = 632$ keV is not so pronounced as in the direct-capture measurements (Fig. 1.6). This is due to our experimental resolution (see Fig. 4.13) and the lower sensitivity of CD to the M1 transition.

The plotted error bars are calculated from the total relative error according to

$$\begin{aligned}\delta^2_{\mathrm{d}\sigma_{\mathrm{CD}}/\mathrm{dE}} &= \delta^2_{\mathrm{STAT}}(\mathrm{E_{REL}}) + \delta^2_{\mathrm{SYST}}(\mathrm{E_{REL}}) + \delta^2_{\mathrm{EX}}(\mathrm{E_{REL}}) \\ &+ \delta^2_{\mathrm{N_{Pb}\cdot N_B}} + \delta^2_{\mathrm{CD}} + \delta^2_{\mathrm{DT}} + \delta^2_{\mathrm{EFF}}(\mathrm{E_{REL}}) \end{aligned} \tag{5.2}$$

where the relative errors $\delta_{\mathrm{STAT}}(\mathrm{E_{REL}})$, $\delta_{\mathrm{SYST}}(\mathrm{E_{REL}})$, $\delta_{\mathrm{EX}}(\mathrm{E_{REL}})$ were described in Section 4.5. The relative uncertainties of the cross-section normalization, analysis efficiency, and the dead-time correction are $\delta_{\mathrm{N_{Pb}\cdot N_B}} = 0.337/144.867 = 0.23\%$ (Section 4.2.3), $\delta_{\mathrm{CD}} = 1.60\%$ (Section 4.3.3), $\delta_{\mathrm{DT}} = 0.19\%$ (Section 4.1.2), respectively. The efficiency cuts introduce $\delta_{\mathrm{EFF}}(\mathrm{E_{REL}})$ which involves the respective errors from Section 4.6, added also quadratically.
As a comparison to the experimental data a GEANT Monte Carlo simulation was done; it is explained in Section 4.9. Evaluating the response of the detector system allows solving the crucial aspects of the analysis including the determination of the detection efficiency and the experimental resolution (Chapter 4). Primarily, with the simulated yield the astrophysical $\mathrm{S_{17}}$-factor is intended to be measured.

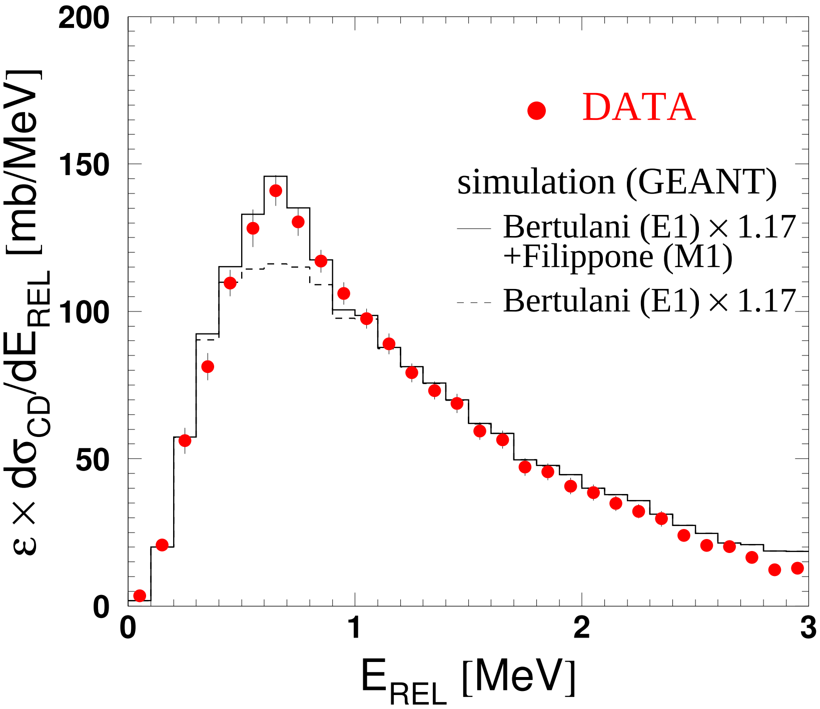

Figure 5.1: *Yield (cross-section × efficiency) of the Coulomb break-up* $^{208}Pb(^{8}B,^{7}Be+p)^{208}Pb$ *as a function of the relative energy p-Be. The histograms are Monte Carlo simulations.*

The full histogram in Fig. 5.1 shows the simulated non-resonant E1 S_{17}-factor from the model of Bertulani [Ber96c] plus the experimental M1-resonance S_{17}-factor described as a Lorentzian distribution fitted to the Filippone direct-capture data [Fil83], both converted to the CD cross-section by the semiclassical theory of Bertulani and Baur [Ber88] (Note in Fig. 2.10 that the semiclassical approach is valid up to a grazing angle of about $\theta_8 = 1.9$ deg. This implies an upper limit in integration over the deflection angle in Eq. 2.101). The simulated yield was corrected by the factor $(1 + R_{GSI})$ to take into account both channels of the CD break-up process (see Section 4.8). The resulting yield was normalized to the data by multiplying the E1 input S_{17}-factor by a factor of 1.17. As we can see the shape and magnitude of the experimental energy-dependence are well reproduced. The E1 simulated yield alone, normalized by the same factor 1.17 is shown by the dashed histogram.
The choice for the input S_{17}-factors was done as follows. In Section 1.2.1 two main approaches to the nuclear model of ^{8}B were described. Unfortunately, neither the cluster model calculations nor the potential models provide a precise description of ^{8}B. However, disregarding all other crucial aspects, it seems that the potential models have the formal advantage to be scalable whereas the cluster description predicts both the energy dependence and the absolute magnitude, so no adjustable parameters are available. In view of this fact the continuum non-resonant contribution was taken from a coupled-channels study by Bertulani [Ber96c]. This E1 amplitude was normalized by the factor of 1.17 to fit the data. Unlike E1, the M1 resonance reflects a more evident spectroscopic property of ^{8}B. Unfortunately, not only in the model of Bertulani, but in any model of ^{8}B the total width of the M1-resonance at $E_{REL} = 632$ keV is not properly reproduced. Therefore, we used for the input M1 S_{17}-factor the total cross-section and the gamma width from the measurement of Filippone [Fil83]. We saw in Section 2.1.2 that the Filippone experimental widths agreed perfectly with the prediction of Decrock [Dec93].
The general goal was to simulate input S-factors of such energy dependence that the observed yield was reproduced the best. Such procedure guarantees that the response of the detector system corresponds exactly to the experimental one and the measurement of the astrophysical factor is precise enough.

In Chapter 1 the problem of the multipole composition of the S_{17}-factor was discussed. Although the E2 transitions are not relevant for the capture cross-section at low energies they are amplified in the Coulomb-dissociation approach. However, as we have seen, different CD-experiments report different contributions of the E2 amplitude. It seems that only the interference effects reveal the E2 strength [Kel96, Dav98] whereas in the CD data [Sch96, Kik97] its effect is reduced, as compared to predictions of the first-order process.
The relative-energy spectrum (Fig. 5.1) is not the most appropriate tool to study the multipole composition of the measured cross-section. The best way for that

purpose is to look at the angular distribution of the excited ^{8}B i.e. the center-of-mass of the released ^{7}Be and proton [Ber96c]. The E2 transitions are dominant at large scattering angles, so a method to separate the E1 from the E2 contribution would be to integrate the angular distribution up to a cut-off angle at which E2 becomes relatively large [Ber96c]. Fig. 5.2 shows the experimental yield of the break-up events as a function of the scattering angle θ_8 of the excited ^{8}B, in three relative-energy bins (in Chapter 2 the Coulomb scattering angle θ was denoted ϑ to distinguish it from the spherical angle). Since there was no running detector available to track the incident beam in front of the target (Chapter 3), the angular spectra are not event-by-event ones but are folded with the beam emittance (lower right figure). The angular spreads are larger than the resolution estimated in Section 4.7 to be 4.8 mrad (0.27 deg), so some conclusions can be drawn. The solid histograms represent the results of the simulation of the

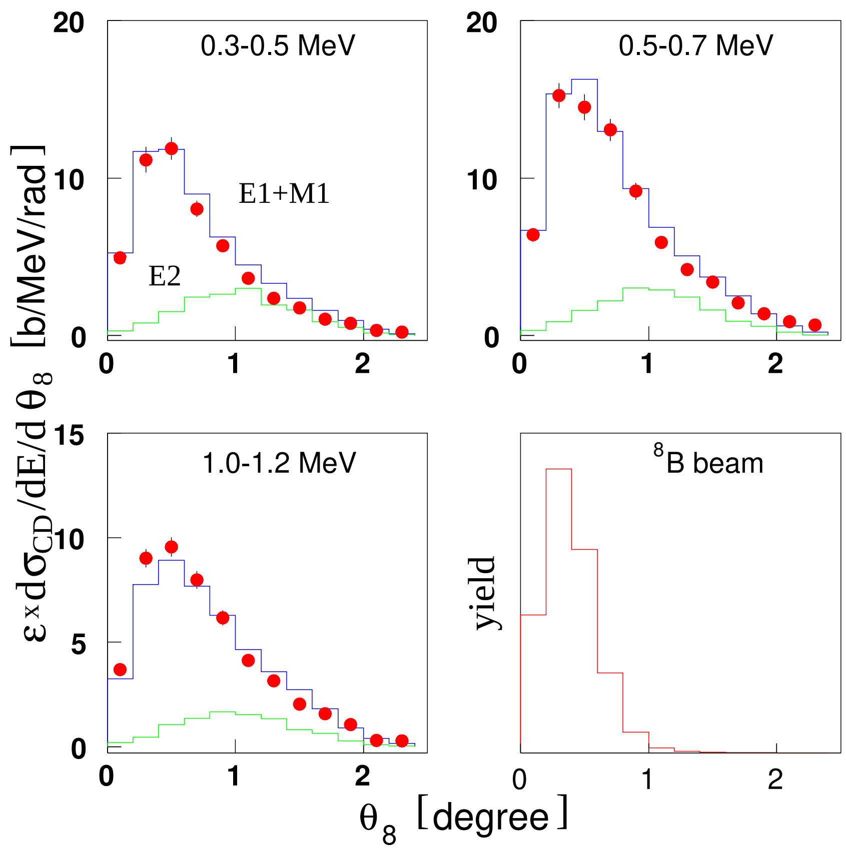

Figure 5.2: *Angular distributions of the excited ^{8}B for three relative-energy bins. The last figure shows the angular spread of the incident ^{8}B beam. Like in Fig. 5.1 the experimental yields include the efficiency correction $\varepsilon(E_{REL})$, the last component in Formula 5.1.*

E1 amplitude from the theory of Bertulani [Ber96c] scaled by the factor of 1.17 plus the M1-resonance contribution as taken from the data of Filippone [Fil83] (both described above). The simulated E2 distributions ([Ber96c]) are shown by the thin histogram. As we can see the experimental yields are reproduced better using the E1 (normalized) and the M1 multipolarity than by the sum of E1, M1 and the E2 amplitude. It is clearly visible that there is no room for the E2 component. Unfortunately, at our beam energy of 254 MeV, possible interference effects between E1 and E2 amplitudes do not lead to noticeable asymmetries in the angular distributions (in the longitudinal-momentum spectra either) and cannot be helpful in determining the strength of E2.
Judging by the relative-energy spectrum, the angular spectra of the excited ^{8}B and, last but not least, taking into account the results of other CD-experiments with lower bombarding energies (the E2 strength decreases with increasing bombarding energy) we extract S_{17} by assuming pure E1 plus M1 multipole components.

By taking all the analyzed CD-events $0 < E_{REL} < \infty$, normalizing the number by the target thickness times the beam intensity ($N_{Pb} \cdot N_B$) and correcting for all the efficiency components, the total reaction cross-section is measured

$$\sigma_{CD}^{TOT} = \frac{N_{CD}}{N_{Pb} \cdot N_B} \times \frac{1}{\varepsilon^{CD}} \times \frac{1}{\varepsilon^{DT}} \times \frac{1}{\varepsilon\left(E_{REL}\right)} \tag{5.3}$$

The measured value amounts to

$$\sigma_{CD}^{TOT} = 295^{+16}_{-11} \text{ mb}$$

where the error bars result from the lower/upper limits of the factors in Formula 5.3.

5.2 Measurement of the astrophysical S_{17}-factor

To derive the continuum E1 S_{17}-factor from the CD data the simulated M1-resonance component is subtracted from the measured yield. Then the theoretical (input) S_{17}-factor is scaled by the ratio of the observed and simulated counts

$$S_{17}(E_{REL}) = \frac{(d\sigma_{CD}(E_{REL})/dE_{REL})_{DATA}}{(d\sigma_{CD}(E_{REL})/dE_{REL})_{GEANT}} \times S_{INPUT}(E_{REL}) \qquad (5.4)$$

The error of such measurement is taken as

$$\delta^2_{\mathrm{S_{17}}} = \delta^2_{\mathrm{d\sigma_{CD}/dE}}(\mathrm{E_{REL}}) + \delta^2_{\mathrm{GEANT}}(\mathrm{E_{REL}}) \qquad (5.5)$$

where $\delta_{\mathrm{d\sigma/dE}}(\mathrm{E_{REL}})$ is the relative error of the measured differential cross-section given by Formula 5.2 and $\delta_{GEANT}(E_{REL}) = \sqrt{yield}/yield$ is the relative statistical error of the simulated yield in a given $\mathrm{E_{REL}}$-bin. When adding the yields of the 100 keV bins into larger, resolution-like bins the errors of 100 keV bins are added quadratically.

The resulting S_{17}-factors are presented in Table 5.1 and Fig. 5.3 as a function of the relative energy p-Be. Together with the GSI CD-data, the existing (p, γ) and the RIKEN-II [Kik98a] CD results are shown. The (p, γ) measurements are normalized to the $^7\mathrm{Li(d,p)}^8\mathrm{Li}$ peak cross-section of 147 ± 11 mb [Ade98].

First, let me compare the two CD-experiments. As we can see, at relative energies above the M1-resonance peak no agreement between the two data sets can be found. The discrepancy is both in the energy dependence and the absolute magnitude. The experimental procedure in RIKEN involves the subtraction of background, which is not the case in the GSI experiment. It is puzzling that first, their error bars do not reflect larger uncertainties and, second, their lowest-$\mathrm{E_{REL}}$ data-points show good agreement with the GSI data. Due to low yields these points should be affected the most.

bin of $\mathrm{E_{REL}}$ [keV]	$\mathrm{E_{REL}}$ [keV]	$\mathrm{S_{17}}$ [eV·b]	$\Delta\mathrm{S_{17}}$ [eV·b]
100-300	223	18.94	2.21
300-500	407	17.90	1.39
500-800	651	20.08	3.95
800-1200	989	23.91	1.92
1200-1600	1389	27.00	2.73
1600-2000	1787	30.92	4.44
2000-2500	2228	35.75	6.23
2500-3000	2722	36.53	8.74

Table 5.1: *Numerical values of the measured S_{17}-factor.*

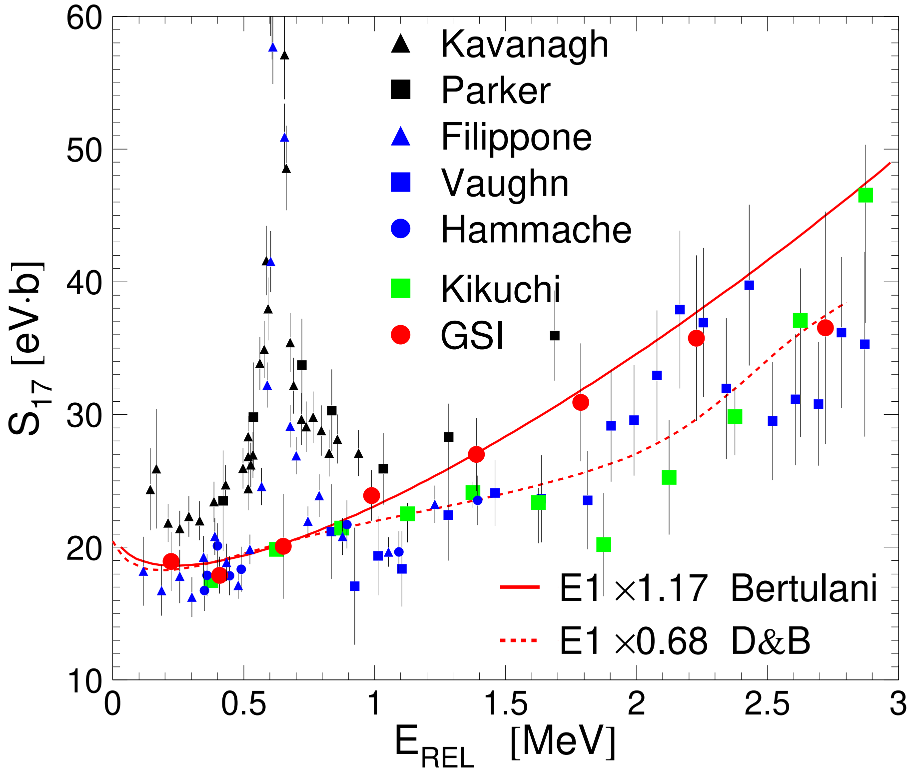

Figure 5.3: *Astrophysical S_{17}-factors determined in the GSI CD-experiment (large circles) in comparison with the RIKEN results [Kik98a] and other, direct-capture, measurements. The full line is based on the theoretical model of Bertulani [Ber96c] normalized to the data. The dashed line represents the cluster model of Descouvemont and Baye [Des94] scaled to our low E_{REL} data-points.*

Both at GSI and RIKEN the S_{17}-factors are deduced assuming pure continuum E1-excitation. Even if an unobserved E2 contribution is present, the RIKEN CD-data are measured at lower laboratory energy (≈50 MeV/u) and should be more sensitive to E2. Consequently, they should yield higher S_{17}-factors than ours. So, it is not clear why the two CD-experiments differ from each other at higher E_{REL}.

As to the direct-capture results, below the M1 resonance our data-points are in line with the Filippone [Fil83] and the most recent Hammache [Ham98] data. At energies above the M1 peak the GSI points seem to be closer to the data of Parker *et al.* [Par66] than to the 'lower-value' S_{17}-results. Note, however, the magnitude of the error bars; they follow larger uncertainties of the correction for feeding the excited state in ^{7}Be (see Fig. 4.11).

The energy dependence of our S_{17}-data points follows closely the prediction of Bertulani's one-body potential model [Ber96c]. The absolute height has to be adjusted by multiplying the theoretical values by a factor of 1.17 as was already shown in the discussion of the differential CD cross-section (Fig. 5.1). For comparison, the cluster-model calculation of Descouvemont and Baye [Des94] is fitted to the low-E_{REL} data-points (dashed line) which requires a normalization factor for the theoretical data of 0.68. Up to about $E_{REL} = 700$ keV both models (see page 15) describe the GSI data equally well. At higher relative energy our data evidently favor the potential-model calculation. The RIKEN results seem to be closer to the cluster-model prediction. Also the last direct-capture experiment of Hammache [Ham98] agrees better with the cluster model from [Des94].

5.3 Extrapolation towards the Gamov peak

In none of the direct-capture and CD experiments S_{17} can be measured at the Gamov peak, about $E_{REL} = 18$ keV. This is due to insufficient yields at the astrophysical energy-window and to the experimental resoluton available (the latter only for CD). From existing data one must extrapolate the energy dependence of the S_{17}-factor in order to fix it, conventionally, at $E_{REL} = 0$ keV. In Section 1.2.1 the relevant physics leading to three ways of extrapolation towards low energies was discussed.

Now the following facts should be underlined:
– Model calculations like we can see in Fig. 5.3 ([Ber96c], [Des94]) are global fits to the data. They assume a nuclear structure of ^{8}B and predict its features over the full range of energy. The single-particle model of Bertulani [Ber96c] appears to describe the GSI data very well; the cluster model of Descouvemont and Baye [Des94] disagrees with our data at higher relative energies. A possible explanation must take into account nuclear-distortion effects, stronger at higher E_{REL}. For that reason, any extrapolation to $E_{REL} = 0$ should use data points below $E_{REL} = 400 - 500$ keV. Up to these energies $^7\mathrm{Be}(\mathrm{p},\gamma)^8\mathrm{B}$ is well assumed to remain a peripheral Coulomb scattering process of point-like charges. Its energy dependence is dominated by an E1 s-wave capture (plus a d-wave admixture) which is a distinctive feature of S_{17} at very low E_{REL}.
– Limiting the energy-range safely below the M1-resonance at $E_{REL} = 632$ keV reduces experimental uncertainties involved in subtraction of M1 from the CD data. A yield of pure E1 continuum excitation is available for an extrapolation.
– Up to $E_{REL} = 500$ keV not more than 3% break-up events feed the inelastic channel in ^{7}Be (see Fig. 4.15, Table 4.11). This introduces a relatively small error (Fig. 4.11) to the pure ground-state break-up process.

At GSI, we extrapolate the zero energy S_{17}-factor from our two data points below $E_{REL} = 500$ keV, using a theoretical energy dependence from the model of Jennings *et al.* [Jen98]. In Section 1.2.1 the physical concepts on which this model is based were introduced. They lead to a Laurent series expansion of the S_{17}-factor

$$S_{17}(E_{REL}) = S_{17}(0)\left[\left(\frac{a}{Q + E_{REL}} + b\right) + c \cdot E_{REL}\right] \tag{5.6}$$

For energies $E_{REL} < 400$ keV S_{17} is dominated by a pole set by the binding energy of the valence proton in ^{8}B (Q-value of the reaction, 137 keV). This property is responsible for the characteristic upturn of S_{17} towards $E_{REL} = 0$. Parameters of a=0.0409 [MeV] and b=0.703 (which are bound by the requirement a/Q+b=1) were found by the authors of Ref. [Jen98] by fitting the expansion to different model calculations. The linear term c shows the effect of the nuclear distortion

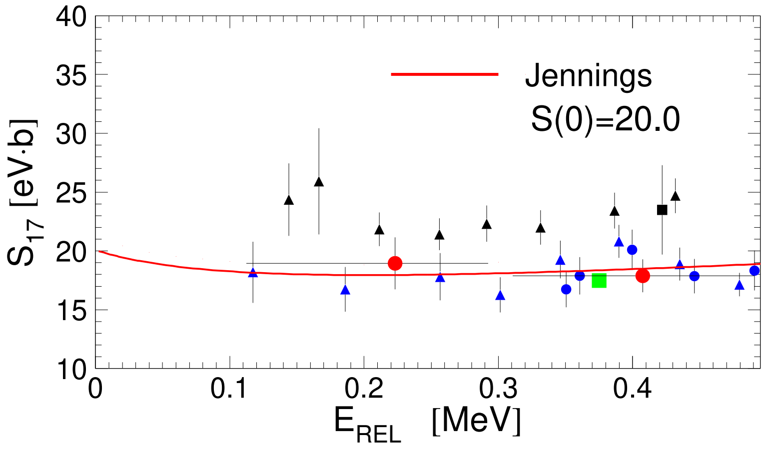

Figure 5.4: *Extrapolation of S_{17} towards E_{REL}=0 with the energy dependence of Jennings et al. [Jen98]. The data points are explained in Fig. 5.3.*

and, on the contrary, is strongly model-dependent. This effect was simulated by a hard-sphere radius r_C. From the data of elastic scattering of thermal neutrons from ^{7}Li a value of r_C = 1.0 fm was found. This implied a slope parameter of c=0.343 [MeV^{-1}].

The only free factor which remains to be determined is $S_{17}(0)$. Fig. 5.4 shows a least-squares fit of Eq. 5.6 to our two data points below $E_{REL} < 500$ keV with the parameters as listed above (since we have only two data points we do not attempt to determine c from our data). $S_{17}(0) = (20.0 \pm 1.3)$ eV·b with $\chi^2 = 0.347$ for two data points has been found. $\chi^2 < 1$ is clear since the experimental error-bars are larger than the minimized distances data points – theoretical curve.

For comparison, a WKB approximation (Eq. 1.3) is presented in Fig. 5.5. In this case one has $S_{17}(0) = (18.3 \pm 1.2)$ eV·b with $\chi^2 = 1.092$.

In both cases we note that, due to larger error bars, the lowest S_{17}-factor has less statistical weight. Moreover, the fits are 'rigid' since their energy-dependences are fixed by following certain physical assumptions.

Our zero-energy S_{17}-factor agrees very well with the data of Filippone *et al.* and Hammache *et al.*, so prefer the lower group of results. However, I note the experimental resolution and the (mostly) systematic uncertainties resulting in the vertical error bars.

Let me compare the GSI result with other extrapolated values of $S_{17}(0)$. The INT Conference [Ade98] used the theoretical energy-dependence of Johnson *et al.* [Joh92] to extrapolate S_{17} towards low E_{REL} from the data of Filippone *et al.* [Fil83]. Their results were considered as the only measurement with two independent and consistent determinations of the target areal density. An addi-

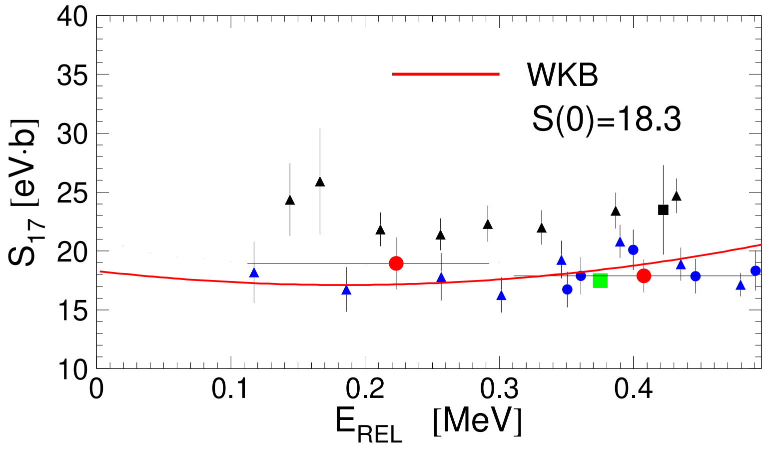

Figure 5.5: *Extrapolation of S_{17} towards E_{REL}=0 with the energy dependence of the WKB approximation [Sch68]. The data points are explained in Fig. 5.3.*

tional argument was an overlap of the Filippone data with those of Vaughn *et al.* [Vau70] in the region around $E_{REL} = 1$ MeV. The recommended zero-energy S_{17}-factor from the INT Conference is $S_{17}(0) = 19^{+4}_{-2}$ eV·b. The error bars take into account other, also the 'higher-value' results. The recent (p, γ) experiment of Hammache *et al.* [Ham98] yields $S_{17}(0) = (18.5 \pm 1.0)$ eV·b when using the model of Descouvemont and Baye [Des94] for extrapolating to $E_{REL} = 0$. The same model and the combined data sets of Filippone, Hammache and Vaughn, so the 'lower-value' results, yield $S_{17}(0) = (18.3 \pm 0.8)$ eV·b. An extrapolation from the RIKEN-II CD-data with [Des94] leads to $S_{17}(0) = (18.9 \pm 1.8)$ eV·b [Kik98a].

So, the two lowest data-points of the GSI CD-experiment are extrapolated towards $E_{REL} = 0$ using the model of Jennings *et al.* [Jen98]. $S_{17}(0) = (20.0 \pm 1.3)$ eV·b is found where the precision reflects the experimental uncertainties. Here no error for the choice of the theoretical model is applied. The energy dependence of Jennings is a detailed approach suitable to describe various theoretical predictions looking most adequate nowadays.

5.4 Conclusions and outlook

The Solar Neutrino Problem has intrigued us for more than thirty years now. Probable solutions of that problem go beyond the standard physics. A motivated assumption is that the neutrino has a mass. To test quantitatively this hypothesis parameters of the neutrino oscillations between the mass eigenstates are investigated. These quantities are related to the magnitude of the astrophysical factor S_{17} i.e. the cross-section for the production of ^{8}B in the Sun.

In this work I investigated the direct-capture cross-section $^7\mathrm{Be}(\mathrm{p},\gamma)^8\mathrm{B}$ by the Coulomb dissociation method. In this approach a relativistic nucleus ^{8}B breaks up into $^7\mathrm{Be}+\mathrm{p}$ in the Coulomb field of a high-Z target. At the heavy-ion laboratory GSI in Darmstadt, Germany we performed an experiment of that kind with a radioactive secondary beam of ^{8}B at $E_{\mathrm{LAB}} = 254$ MeV/u. The break-up products were identified in coincidence at the high-acceptance spectrometer KaoS. The total measured Coulomb-dissociation cross-section amounts to $\sigma_{\mathrm{CD}}^{\mathrm{TOT}} = 295^{+16}_{-11}$ mb. The relative-energy spectrum of ^{7}Be and proton has been measured event-by-event. From this data the astrophysical factor $S_{17}(E_{\mathrm{REL}})$ has been determined. Using a theoretical energy dependence the zero-energy S-factor is found – $S_{17}(0) = (20.0 \pm 1.3)$ eV·b. This value agrees with other direct-capture measurements and with the RIKEN Coulomb-dissociation experiment at $E_{\mathrm{LAB}} = 50$ MeV/u. At higher relative-energies the two CD measurements disagree. The remaining theoretical issues like the E2 amplitude are subject of an improved experiment with better resolution and precision.

The Coulomb dissociation has proven to be an alternative method to measure the direct-capture cross-section $^7\mathrm{Be}(\mathrm{p},\gamma)^8\mathrm{B}$. There are also other astrophysical (p,γ) reactions successfully studied in this way. Taking advantage of the KaoS spectrometer at the heavy-ion laboratory GSI in Darmstadt, Germany, a series of CD-experiments is planned [Sum98] (currently ^{8}B, ^{27}P, ^{23}Al). Studying astrophysical reaction-rates by the Coulomb break-up of radioactive beams seems nowadays to be a challenging subject of science.

Bibliography

[Abd94] J. Abdurashitov, E. Faizov, V. Gavrin, A. Gusev, A. Kalikhov, T. Knodel, I. Knyshenko, V. Kornoukhov, I. Mirnov, A. Pshukov, A. Shalagin, A. Shikhin, P. Timofeyev, E. Veretenkin, V. Vermul, G. Zatsepin, T. Bowles, J. Nico, W. Teasdale, D. Wark, J. Wilkerson, B. Cleveland, T. Saily, R. Davis Jr., K. Lande, C. Lee, P. Wildenhain, S. Elliott, M. Cherry, and R. Kouzes. "Results from SAGE". *Physics Letters B*, Vol. 328, pp. 234–248, 1994.

[Abd96] J. Abdurashitov, V. Gavrin, S. Girin, V. Gorbatchev, A. Gusev, A. Kalikhov, T. Knodel, I. Mirmov, A. Pshukov, A. Shalagin, A. Shikhin, E. Veretenkin, V. Vermul, V. Yants, G. Zatsepin, T. Bowles, J. Nico, W. Teasdale, D. Wark, S. Elliott, J. Wilkerson, B. Cleveland, T. Daily, R. Davis Jr., K. Lande, C. Lee, P. Wildenhain, and M. Cherry. "Results from SAGE". *Nuclear Physics B (Proc. Suppl.)*, Vol. 48, pp. 299–303, 1996.

[Abr72] M. Abramowitz and I. Stegun. *Handbook of Mathematical Functions.* Dover Publications, Inc., New York, 1972.

[Ade98] E. Adelberger, S. Austin, J. Bahcall, A. Balantekin, G. Bertsch, G. Bogaert, L. Brown, L. Buchmann, F. Cecil, A. Champagne, L. Braeckeleer, C. Duba, R. Elliott, S. J. Freedman, M. Gai, G. Goldring, C. Gould, A. Gruzinov, W. Haxton, K. Heeger, E. Henley, C. Johnson, M. Kamionkowski, R. Kavanagh, E. Koonin, K. Kubodera, K. Langanke, T. Motobayashi, V. Pandharipande, P. Parker, R. Robertson, C. Rolfs, R. Sawyer, N. Shaviv, T. Shoppa, K. Snover, E. Swanson, R. Tribble, S. Turck-Chièze, and J. Wilkerson. "Solar Fusion Rates". *Reviews of Modern Physics*, Vol. 70, pp. 1265–1291, 1998.

[Ajz88] F. Ajzenberg-Selove. "ENERGY LEVELS OF LIGHT NUCLEI A=5-10". *Nuclear Physics A*, Vol. 490, pp. 1–225, 1988.

[Ald75] K. Alder and A. Winther. *Electromagnetic Excitation.* North-Holland Publishing Co., Amsterdam, 1975.

[Ale89] A. Aleixo and C. Bertulani. "Coulomb Excitation in Intermediate-Energy Collisions". *Nuclear Physics A*, Vol. 505, pp. 448–470, 1989.

[Ans95] P. Anselmann, R. Fockenbrock, W. Hampel, G. Heusser, J. Kiko, T. Kirsten, M. Laubenstein, E. Pernicka, S. Pezzoni, U. Rön, M. Sann, F. Spielker, R. Wink, M. Wojcik, R. v.Ammon, K. Ebert, T. Fritsch, D. Heidt, E. Henrich, C. Schlosser, L. Stieglitz, F. Weirich, M. Balata, H. Lalla, E. Belotti, C. Cattadori, O. Cremonesi, N. Ferrari, E. Fiorini, L. Zanotti, M. Altmann, F. v. Feilitzsch, R. Mößbauer, U. Schanda, G. Berthomieu, E. Schatzmann, I. Carmi, I. Dostrovsky, C. Bacci, P. Belli, R. Bernabei, S. d'Angelo, L. Paoluzi, A. Bevilacqua, S. Charbit, M. Cribier, G. Dupont, L. Gosset, J. Rich, M. Spiro, T. Stolarczyk, C. Tao, D. Vignaud, J. Boger, R. Hahn, F. Hartmann, J. Rowley, R. Stoenner, and J. Weneser. "First results from the ^{51}Cr neutrino source experiment with the GALLEX detector". *Physics Letters B*, Vol. 342, pp. 440–450, 1995.

[Arn90] M. Arnould and N. Prantzos. "NUCLEOSYNTHESIS: AN OVERVIEW". Proceedings of the Joliot-Curie summer school "La Physique Nucleaire du laboratoire aux etoiles", Bordeaux, 1990. See also Arnould and Takahashi, Rep. Progr. Phys., 1999.

[Azh99] A. Azhari, V. Burjan, F. Carstoiu, H. Dejbakhsh, C. Gagliardi, V. Kroha, A. Mukhamedzhanov, L. Trache, and R. Tribble. "The ^{10}B(^{7}Be, ^{8}B)^{9}Be Reaction and the ^{7}Be(p, γ)^{8}B S Factor". *Physical Review Letters*, Vol. 82, pp. 3960–3963, 1999.

[Bah88] J. Bahcall and R. Ulrich. "Solar models, neutrino experiments, and helioseismology". *Reviews of Modern Physics*, Vol. 60, pp. 297–372, 1988.

[Bah89a] J. Bahcall. *Neutrino Astrophysics*. Cambridge University Press, Cambridge, 1989.

[Bah89b] J. Bahcall and W. Haxton. "Matter-enhanced neutrino oscillations in the standard solar model". *Physical Review D*, Vol. 40, pp. 931–941, 1989.

[Bah92] J. Bahcall and M. Pinsonneault. "Standard solar models, with and without helium diffusion, and the solar neutrino problem". *Reviews of Modern Physics*, Vol. 64, pp. 885–926, 1992.

[Bah95] J. Bahcall and M. Pinsonneault. "Solar models with helium and heavy-element diffusion". *Reviews of Modern Physics*, Vol. 67, pp. 781–808, 1995.

[Bah96] J. Bahcall. "Solar Neutrinos: Where We Are, Where We Are Going". *The Astrophysical Journal*, Vol. 467, pp. 475–484, 1996.

[Bah98a] J. Bahcall, S. Basu, and M. Pinsonneault. "How uncertain are solar neutrino predictions?". *Physics Letters B*, Vol. 433, pp. 1–8, 1998.

[Bah98b] J. Bahcall, P. Krastev, and A. Smirnov. "Where do we stand with solar neutrino oscillations?". *Physical Review D*, Vol. 58, p. 096016-1, 1998.

[Bar86] F. Barker and R. Spear. "A COMMENT ON THE ^{7}Be(p, γ)^{8}B CROSS SECTION AND THE SOLAR NEUTRINO PROBLEM". *The Astrophysical Journal*, Vol. 307, pp. 847–851, 1986.

[Bar88] F. Barker. "Comments on 'Radiative Capture Reaction ^{7}Be(p, γ)^{8}B at Low Energies'". *Physical Review C*, Vol. 37, pp. 2920–2921, 1988.

[Bar95] F. Barker. "The low-energy ^{7}Be(p, γ)^{8}B cross section from an R-matrix approach". *Nuclear Physics A*, Vol. 588, pp. 693–705, 1995.

[Bau94] G. Baur and H. Rebel. "Coulomb dissociation studies as a tool of nuclear astrophysics". *Journal of Physics G: Nuclear and Particle Physics*, Vol. 20, pp. 1–33, 1994.

[Bau96] G. Baur and H. Rebel. "COULOMB BREAKUP OF NUCLEI-APPLICATIONS TO ASTROPHYSICS". *Annual Review of Nuclear and Particle Science*, Vol. 46, pp. 321–350, 1996.

[Ber85] C. Bertulani and G. Baur. "Relativistic Coulomb Collisions and the Virtual Radiation Spectrum". *Nuclear Physics A*, Vol. 442, pp. 739–752, 1985.

[Ber88] C. Bertulani and G. Baur. "Electromagnetic Processes in Relativistic Heavy Ion Collisions". *Physics Reports*, Vol. 163, pp. 299–408, 1988.

[Ber93a] G. Bertsch and C. Bertulani. "Coulomb reacceleration as a clock for nuclear reactions". *Nuclear Physics A*, Vol. 556, pp. 136–146, 1993.

[Ber93b] C. Bertulani and A. Nathan. "Excitation and Photon Decay of Giant Resonances from High-Energy Collisions of Heavy Ions". *Nuclear Physics A*, Vol. 554, pp. 158–172, 1993.

[Ber95] C. Bertulani. "The Photodissociation of ^{8}B and the Solar Neutrino Problem". *Nuclear Physics A*, Vol. 587, pp. 318–338, 1995.

[Ber96a] V. Berezinsky, G. Fiorentini, and M. Lissia. "LAST HOPE for an astrophysical solution to the solar neutrino problem". *Physics Letters B*, Vol. 365, pp. 185–192, 1996.

[Ber96b] R. Bernabei. "Implications of the GALLEX results after the Chromium source experiment". *Nuclear Physics B (Proc. Suppl.)*, Vol. 48, pp. 304–308, 1996.

[Ber96c] C. Bertulani. "$^{7}\mathrm{Be}(\mathrm{p},\gamma)^{8}\mathrm{B}$ cross section from indirect breakup experiments". *Zeitschrift für Physik A*, Vol. 356, pp. 293–297, 1996.

[Ber96d] C. Bertulani and L. Canto. "Theory of multiphonon excitation in heavy-ion collisions". *Physical Review C*, Vol. 53, pp. 334–346, 1996.

[Ber98] C. Bertulani and M. Gai. "A study of the Coulomb dissociation of ^{8}B and the $^{7}\mathrm{Be}(\mathrm{p},\gamma)^{8}\mathrm{B}$ reaction". *Nuclear Physics A*, Vol. 636, pp. 227–239, 1998.

[Beu90] E. Beuville, K. Borer, E. Chesi, E. Heijne, P. Jarron, B. Lisowski, and S. Singh. "AMPLEX, A LOW-NOISE, LOW POWER ANALOG CMOS SIGNAL PROCESSOR FOR MULTI-ELEMENT SILICON PARTICLE DETECTORS". *Nuclear Instruments and Methods in Physics Research A*, Vol. 288, pp. 157–167, 1990.

[Bou99] F. Boué. *The Coulomb Dissociation of ^{8}B and Implications for the S_{17} Astrophysical S-Factor*. PhD thesis, L'Université Bordeaux I, 1999.

[Bro96] B. Brown, A. Csótó, and R. Sherr. "Coulomb displacement energy and the low-energy astrophysical S_{17} factor for the $^{7}\mathrm{Be}(\mathrm{p},\gamma)^{8}\mathrm{B}$ reaction". *Nuclear Physics A*, Vol. 597, pp. 66–84, 1996.

[Bru68] H. Brunnader, J. Hardy, and J. Cerny. "Carbon-10 and Mass Measurements for Light Nuclei". *Physical Review*, Vol. 174, pp. 1247–1249, 1968.

[Bru95] R. Brun *et al. PAW Physics Analysis Workstation, Program Library Q121*. CERN, 1995.

[Bru98] A. Brun, S. Turck-Chièze, and P. Morel. *The Astrophysical Journal*, Vol. 506, p. 913, 1998.

[CAE94a] C.A.E.N. *V550 User's Manual Preliminary*. Viareggio, Italy, 1994.

[CAE94b] C.A.E.N. *V551 User's Manual Preliminary*. Viareggio, Italy, 1994.

[Cas94] V. Castellani, S. Degl'Innocenti, G. Fiorentini, M. Lissia, and B. Ricci. "Neutrinos from the Sun: Experimental results confronted with solar models". *Physical Review D*, Vol. 50, pp. 4749–4761, 1994.

[Cas97] V. Castellani, S. Degl'Innocenti, G. Fiorentini, M. Lissia, and B. Ricci. "Solar neutrinos: beyond standard solar models". *Physics Reports*, Vol. 281, pp. 309–398, 1997.

[Cas99] V. Castellani, S. Degl'Innocenti, W. Dziembowski, G. Fiorentini, and B. Ricci. "HELIOSEISMOLOGY, SOLAR MODELS AND NEUTRINO FLUXES". *Nuclear Physics B (Proc. Suppl.)*, Vol. 70, pp. 301–314, 1999.

[Cha70] G. Charpak, D. Rahm, and H. Steiner. "SOME DEVELOPMENTS IN THE OPERATION OF MULTIWIRE PROPORTIONAL CHAMBERS". *Nuclear Instruments and Methods in Physics Research B*, Vol. 80, pp. 13–34, 1970.

[Chr96] J. Christensen-Dalsgaard. "Helioseismology, Solar Models and Solar Neutrinos". *Nuclear Physics B (Proc. Suppl.)*, Vol. 48, pp. 325–334, 1996.

[Cla83] D. Clayton. *Principles of Stellar Evolution and Nucleosynthesis.* The University of Chicago Press, Chicago and London, 1983.

[Cle98] B. Clevelad, T. Daily, R. Davis Jr., J. Distel, K. Lande, C. Lee, P. Wildenhain, and J. Ullman. *The Astrophysical Journal*, Vol. 495, 1998.

[Coh67] S. Cohen and D. Kurath. "SPECTROSCOPIC FACTORS FOR THE 1p SHELL". *Nuclear Physics A*, Vol. 101, pp. 1–16, 1967.

[Cri99] M. Cribier. "Results of the whole GALLEX experiment". *Nuclear Physics B (Proc. Suppl.)*, Vol. 70, pp. 284–291, 1999.

[Cso95] A. Csótó, K. Langanke, S. Koonin, and T. Shoppa. "$^{7}\mathrm{Be}(\mathrm{p},\gamma)^{8}\mathrm{B}$ cross section and the properties of $^{7}\mathrm{Be}$". *Physical Review C*, Vol. 52, pp. 1130–1133, 1995.

[Dar96a] A. Dar and G. Shaviv. *The Astrophysical Journal*, Vol. 468, p. 933, 1996.

[Dar96b] A. Dar and G. Shaviv. "STANDARD SOLAR NEUTRINOS". *Nuclear Physics B (Proc. Suppl.)*, Vol. 48, pp. 335–342, 1996.

[Dav68] R. Davis, D. Harmer, and K. Hoffman. *Physical Review Letters*, Vol. 20, pp. 1205–1209, 1968.

[Dav94] R. Davis. "A Review of the Homestake Solar Neutrino Experiment". *Progress in Particle and Nuclear Physics*, Vol. 32, pp. 13–32, 1994. Proceedings of the International School of Nuclear Physics, Erice, 8-17 September 1993 (edited by A. Faessler).

[Dav98] B. Davids, D. Anthony, S. Austin, D. Bazin, B. Blank, J. Caggiano, M. Chartier, H. Esbensen, P. Hui, C. Powell, H. Scheit, B. Sherrill, M. Steiner, P. Thirolf, J. Yurkon, and A. Zeller. "Measurement of E2 Transitions in the Coulomb Dissociation of $^{8}\mathrm{B}$". *Physical Review Letters*, Vol. 81, pp. 2209–2212, 1998.

[Dec93] P. Decrock, M. Gaelens, M. Huyse, G. Reusen, G. Vancraeynest, P. Van Duppen, J. Wauters, T. Delbar, W. Galster, P. Leleux, I. Licot, E. Liénard, P. Lipnik, C. Michotte, J. Vervier, and H. Oberhummer. "Study of the $^{13}\mathrm{N}(\mathrm{d},\mathrm{n})^{14}\mathrm{O}$ reaction cross section and its astrophysical implications for the $^{13}\mathrm{N}$ proton capture reaction". *Physical Review C*, Vol. 48, pp. 2057–2067, 1993.

[Des94] P. Descouvemont and D. Baye. "Microscopic study of the $^{7}\mathrm{Li}(\mathrm{n},\gamma)^{8}\mathrm{Li}$ and $^{7}\mathrm{Be}(\mathrm{p},\gamma)^{8}\mathrm{B}$ reactions in a multiconfiguration three-cluster model". *Nuclear Physics A*, Vol. 567, pp. 341–353, 1994.

[Eis70] J. Eisenberger and W. Greiner. *EXCITATION MECHANISMS OF THE NUCLEUS.* North-Holland Publishing Company, Amsterdam, London, 1970.

[Ell96a] S. Elliott, J. Abdurashitov, T. Bowles, M. Cherry, B. Cleveland, T. Daily, R. Davis Jr., V. Gavrin, S. Girin, V. Gorbatschev, A. Gusev, A. Kalikhov, N. Khairnasov, V. Karaulov, T. Knodel, V. Kornoukhov, Y. Khomyakov, K. Lande, C. Lee,

V. Levitin, V. Maev, I. Mirmov, P. Nazarenko, J. Nico, A. Pshukov, A. Shalagin, A. Shikhin, V. Shkolnik, N. Skorikov, W. Teasdale, E. Veretenkin, V. Vermul, D. Wark, P. Wildenhain, J. Wilkerson, V. Yants, and A. Zatsepin, G.T. Zvonarev. "Preliminary Results from the Russian-American Gallium Experiment Cr-neutrino Source Measurement". *Nuclear Physics B (Proc. Suppl.)*, Vol. 48, pp. 370–374, 1996.

[Ell96b] J. Ellis. "ASTROPARTICLE PHYSICS - A PERSONAL OUTLOOK". *Nuclear Physics B (Proc. Suppl.)*, Vol. 48, pp. 522–544, 1996.

[Esb95] H. Esbensen, G. Bertsch, and C. Bertulani. "Higher-order Dynamical Effects in Coulomb Dissociation". *Nuclear Physics A*, Vol. 581, pp. 107–118, 1995.

[Esb96] H. Esbensen and G. Bertsch. "Effects of E2 transitions in the Coulomb dissociation of ^{8}B". *Nuclear Physics A*, Vol. 600, pp. 37–62, 1996.

[Ess88] H. Essel. *GOOSY Data Acquisition and Analysis.* GSI, 1988.

[Fil83] B. Filippone, A. Elwyn, C. Davids, and D. Koetke. "Proton capture cross section of ^{7}Be and the flux of high energy solar neutrinos". *Physical Review C*, Vol. 28, pp. 2222–2229, 1983.

[Fio94] G. Fiorentini, M. Lissia, G. Mezzorani, M. Moretti, and D. Vignaud. "Solar neutrino experiments and determination of the neutrino oscillation parameters". *Physical Review D*, Vol. 49, pp. 6298–6318, 1994.

[Fow84] W. Fowler. "Experimental and theoretical nuclear astrophysics: the quest for the origin of the elements". *Reviews of Modern Physics*, Vol. 56, pp. 149–179, 1984.

[Fuk96] Y. Fukuda, T. Hayakawa, K. Inoue, K. Ishihara, H. Ishino, S. Joukou, T. Kajita, S. Kasuga, Y. Koshio, T. Kumita, K. Matsumoto, M. Nakahata, K. Nakamura, K. Okumura, A. Sakai, M. Shiozawa, J. Suzuki, Y. Suzuki, T. Tomoeda, Y. Totsuka, K. Hirata, K. Kihara, Y. Oyama, M. Koshiba, K. Nishijima, T. Horiuchi, K. Fujita, S. Hatakeyama, M. Koga, T. Maruyama, A. Suzuki, M. Mori, T. Kajimura, T. Suda, A. Suzuki, T. Ishizuka, K. Miyano, H. Ozawa, T. Hara, Y. Nagashima, M. Takita, T. Yamaguchi, Y. Hayato, K. Kaneyuki, T. Suzuki, Y. Takeuchi, T. Tanimori, S. Tasaka, E. Ichihara, S. Miyamoto, and K. Nishikawa. "Solar Neutrino Data Covering Solar Cycle 22". *Physical Review Letters*, Vol. 77, pp. 1683–1686, 1996.

[Fuk98] Y. Fukuda et al. *Physical Review Letters*, Vol. 81, p. 1158, 1998.

[Gai95] M. Gai and C. Bertulani. "Comment on 'E2 Contribution to the ^{8}B $\rightarrow$ p $+^7$ Be Coulomb Dissociation Cross Section'". *Physical Review C*, Vol. 52, pp. 1706–1708, 1995.

[Gei92] H. Geissel, P. Armbruster, A. Behr, A. Brünle, K. Burkard, M. Chen, H. Folger, B. Franczak, H. Keller, O. Klepper, B. Langenbeck, F. Nickel, E. Pfeng, M. Pfützner, E. Roeckl, K. Rykaczewski, I. Schall, D. Schardt, C. Scheidenberger, K. Schmidt, A. Schröter, T. Schwab, K. Sümmerer, M. Weber, G. Münzenberg, T. Brohm, H. Clerc, M. Fauerbach, J. Gaimard, A. Grewe, E. Hanelt, B. Knódler, M. Steiner, B. Voss, J. Weckenmann, C. Ziegler, A. Magel, H. Wollnik, J. Dufour, Y. Fujita, D. Vieira, and B. Sherrill. "The GSI projectile fragment separator (FRS): a versatile magnetic system for relativistic heavy ions". *Nuclear Instruments and Methods in Physics Research B*, Vol. 70, pp. 286–297, 1992.

[Gei98] H. Geissel *et al. ATIMA – ATomic Interaction with MAtter.* GSI, 1998.

[Gia00] L. Gialanella, F. Strieder, L. Campajola, A. D'Onofrio, U. Greife, G. Gyurky, F. Schümann, G. Imbriani, G. Oliviero, A. Ordine, V. Roca, C. Rolfs, M. Romano, D. Rogalla, C. Sabbarese, E. Somorjai, F. Terrasi, and H. Trautvetter. "Absolute cross section of p(^{7}Be, γ)^{8}B using a novel approach". *European Physical Journal A*, Vol. 7, pp. 303–305, 2000.

[Gia94] S. Giani *et al. GEANT Detector Description and Simulation Tool, Program Library W5013.* CERN, 3.21 Ed., 1994.

[Gra88] I. Gradshteyn and I. Ryzhik. *Table of Integrals, Series, and Products - Corrected and Enlarged Edition.* Academic Press, Inc., San Diego, California, 1988.

[Ham96] W. Hampel, G. Heusser, J. Kiko, T. Kirsten, M. Laubenstein, E. Pernicka, W. Rau, U. Rön, C. Schlosser, M. Wójcik, Y. Zakharov, R. v.Ammon, K. Ebert, T. Fritsch, D. Heidt, E. Henrich, L. Stieglitz, F. Weirich, M. Balata, M. Sann, F. Hartmann, E. Belotti, C. Cattadori, N. Cremonesi, O. Ferrari, E. Fiorini, L. Zanotti, M. Altmann, F. v. Feilitzsch, R. Mös̈bauer, G. Berthomieu, E. Schatzmann, I. Carmi, I. Dostrovsky, C. Bacci, P. Belli, R. Bernabei, S. d'Angelo, L. Paoluzi, A. Bevilacqua, M. Cribier, L. Gosset, J. Rich, M. Spiro, C. Tao, D. Vignaud, J. Boger, R. Hahn, J. Rowley, R. Stoenner, and J. Weneser. "GALLEX solar neutrino observations: Results for GALLEX III". *Physics Letters B*, Vol. 388, pp. 384–396, 1996.

[Ham98] F. Hammache, G. Bogaert, C. Angulo, S. Barhoumi, L. Brillard, J. Chemin, G. Claverie, A. Coc, M. Hussonnois, M. Jacotin, J. Kiener, A. Lefebvre, J. Scheurer, J. Thibaud, and E. Virassamynaiken. "New Measurement and Analysis of the ^{7}Be(p, γ)^{8}B Cross Section". *Physical Review Letters*, Vol. 80, pp. 928–931, 1998.

[Hat95] N. Hata and W. Haxton. "Implications of the GALLEX source experiment for the solar neutrino problem". *Physics Letters B*, Vol. 353, pp. 422–431, 1995.

[Hax95] W. Haxton. "THE SOLAR NEUTRINO PROBLEM". *Annual Review of Astronomy and Astrophysics*, Vol. 33, pp. 459–503, 1995.

[Hax96] W. Haxton. "Nuclear and Atomic Physics of the Solar Neutrino Problem". *Nuclear Physics B (Proc. Suppl.)*, Vol. 48, pp. 317–324, 1996.

[Hir91] K. Hirata, K. Inoue, T. Ishida, T. Kajita, K. Kihara, M. Nakahata, K. Nakamura, S. Ohara, N. Sato, Y. Suzuki, Y. Totsuka, Y. Yaginuma, M. Mori, Y. Oyama, A. Suzuki, T. K., M. Yamada, M. Koshiba, K. Nishijima, T. Suda, T. Tajima, K. Miyano, H. Miyata, H. Takei, Y. Fukuda, E. Kodera, Y. Nagashima, M. Takita, K. Kaneyuki, T. Tanimori, E. Beier, L. Feldscher, E. Frank, W. Frati, S. Kim, A. Mann, F. Newcomer, R. Van Berg, and W. Zhang. "Real-time, directional measurement of ^{8}B solar neutrinos in the Kamiokande II detector". *Physical Review D*, Vol. 44, pp. 2241–2260, 1991.

[Ino99] K. Inoue. "Solar Neutrinos at Super-Kamiokande". *Nuclear Physics B (Proc. Suppl.)*, Vol. 70, pp. 273–283, 1999.

[Iwa96] N. Iwasa, T. Motobayashi, Y. Ando, M. Kurukawa, H. Murakami, J. Ruan, S. Shimoura, S. Shirato, N. Inabe, T. Kubo, Y. Watanabe, M. Gai, R. France III, K. Hahn, Z. Zhao, T. Nakamura, T. Teranishi, Y. Futami, K. Furutaka, T. Delbar, and M. Ishihara. "Study of the ^{7}Be(p, γ)^{8}B Reaction with the Coulomb Dissociation Method". *Journal of the Physical Society of Japan*, Vol. 65, pp. 1256–1263, 1996.

[Iwa97] N. Iwasa, H. Geissel, G. Münzenberg, C. Scheidenberger, T. Schwab, and H. Wollnik. "MOCADI, a universal Monte Carlo code for the transport of heavy ions through matter within ion-optical systems". *Nuclear Instruments and Methods in Physics Research B*, Vol. 126, pp. 284–289, 1997.

[Jac75] J. Jackson. *Classical Electrodynamics.* Wiley, New York, 2nd Ed., 1975.

[Jen98] B. Jennings, S. Karataglidis, and T. Shoppa. "Extrapolation of the astrophysical S factor for ^{7}Be(p, γ)^{8}B to solar energies". *Physical Review C*, Vol. 58, pp. 3711–3721, 1998.

[Joa83] C. Joachain. *Quantum Collision Theory.* North-Holland Physics Publishing, Amsterdam, 1983.

[Joh92] C. Johnson, E. Kolbe, S. Koonin, and K. Langanke. "THE FATE OF ^{7}Be IN THE SUN". *The Astrophysical Journal*, Vol. 392, pp. 320–327, 1992.

[Kav60] R. Kavanagh. "Proton Capture in ^{7}Be". *Nuclear Physics*, Vol. 15, pp. 411–420, 1960.

[Kav69] R. Kavanagh *et al. Bulletin of the American Physical Society*, Vol. 14, p. 1209, 1969.

[Kel96] J. Kelley, S. Austin, A. Azhari, D. Bazin, J. Brown, H. Esbensen, M. Fauerbach, M. Hellström, S. Hirzebruch, R. Kryger, D. Morrissey, R. Pfaff, C. Powell, E. Ramakrishnan, B. Sherrill, M. Steiner, T. Suomijärvi, and M. Thoennessen. "Study of the Breakup Reaction ^{8}B $\rightarrow^7$ Be+p : Absorption Effects and E2 Strength". *Physical Review Letters*, Vol. 77, pp. 5020–5023, 1996.

[Kie91] J. Kiener, H. Gils, H. Rebel, S. Zagromski, G. Gsottschneider, N. Heide, H. Jelitto, J. Wentz, and G. Baur. "Measurement of the Coulomb dissociation cross section of 156 MeV ^6Li projectiles at extremely low relative fragment energies of astrophysical interest". *Physical Review C*, Vol. 44, pp. 2195–2208, 1991.

[Kik97] T. Kikuchi, T. Motobayashi, N. Iwasa, Y. Ando, M. Kurukawa, S. Moriya, H. Murakami, T. Nishibo, J. Ruan, S. Shirato, S. Shimoura, T. Uchibori, Y. Yanagisawa, T. Kubo, H. Sakurai, T. Terani shi, Y. Watanabe, M. Ishihira, M. Hirai, T. Nakamura, S. Kubono, M. Gai, R. France III, K. Hahn, T. Delbar, P. Lipnik, and C. Michotte. "Experimental determination of the E2 component in the Coulomb dissociation of ^{8}B". *Physics Letters B*, Vol. 391, pp. 261–266, 1997.

[Kik98a] T. Kikuchi, T. Motobayashi, N. Iwasa, Y. Ando, M. Kurukawa, S. Moriya, H. Murakami, T. Nishio, J. Ruan, S. Shirato, S. Shimoura, T. Uchibori, Y. Yanagisawa, T. Kubo, H. Sakurai, T. Teranishi, Y. Watanabe, M. Ishihira, M. Hirai, T. Nakamura, S. Kubono, M. Gai, R. France III, K. Hahn, T. Delbar, P. Lipnik, and C. Michotte. "Further measurements of the ^{7}Be(p, γ)^{8}B cross section at low energies with the Coulomb dissociation of ^{8}B". *European Physical Journal A*, Vol. 3, pp. 213–215, 1998.

[Kik98b] T. Kikuchi *et al.* "private communication". 1998.

[Kim87] K. Kim, M. Park, and B. Kim. "Radiative Capture Reaction ^{7}Be(p, γ)^{8}B at Low Energies". *Physical Review C*, Vol. 35, pp. 363–366, 1987.

[Kox87] S. Kox, A. Gamp, C. Perrin, J. Arvieux, R. Bertholet, J. Bruandet, M. Buenerd, R. Cherkaoui, A. Cole, Y. El-Masri, N. Longequeue, J. Menet, F. Merchez, and J. Viano. "Trends of total reaction cross section for heavy ion collisions in the intermediate energy range". *Physical Review C*, Vol. 35, pp. 1678–1691, 1987.

[Kra93] H. Krauss, K. Grün, T. Rauscher, and H. Oberhummer. "The astrophysical S-factor of the reaction ^{7}Be(p, γ)^{8}B in the direct capture model". *Annalen der Physik*, Vol. 2, pp. 258–266, 1993.

[Lan75] L. Landau and E. Lifshitz. *The Classical Theory of Fields.* Pergamon Press, Oxford, 1975.

[Lan76] L. Landau and E. Lifshitz. *Mechanics.* Pergamon Press, Oxford, 1976.

[Las95] K. Lassila-Perini and L. Urbán. "Energy loss in thin layers in GEANT". *Nuclear Physics A*, Vol. 362, pp. 416–422, 1995.

[Lin95] L. Lindemann and G. Zech. "Unfolding by weighting Monte Carlo events". *Nuclear Instruments and Methods in Physics Research A*, Vol. 354, pp. 516–521, 1995.

[Liu96] W. Liu, X. Bai, S. Zhou, Z. Ma, Z. Li, Y. Wang, A. Li, Z. Ma, B. Chen, X. Tang, Y. Han, and Q. Shen. "Angular Distribution for the $^7\mathrm{Be}(\mathrm{d,n})^8\mathrm{B}$ Reaction at $\mathrm{E_{c.m.}} =$ 5.8 MeV and the $\mathrm{S_{17}}(0)$ Factor for the $^7\mathrm{Be}(\mathrm{p},\gamma)^8\mathrm{B}$ Reaction". *Physical Review Letters*, Vol. 77, pp. 611–614, 1996.

[McG67] R. McGrath, J. Cerny, and E. Norbeck. "UNBOUND NUCLIDE $^7\mathrm{B}$". *Physical Review Letters*, Vol. 19, pp. 1442–1444, 1967.

[Men98] A. Mengoni, T. Motobayashi, and T. Otsuka. "Reaction rates from Coulomb dissociation: Core excitation effects". Proceedings of 'Nuclei in the Cosmos', Volos, Grece, 1998.

[Mik85] S. Mikheyev and Y. Smirnov. *Y.Fiz.Soviet Journal*, Vol. 42, p. 1441, 1985.

[Mot94] T. Motobayashi, N. Iwasa, Y. Ando, M. Kurukawa, H. Murakami, J. Ruan, S. Shimoura, S. Shirato, N. Inabe, M. Ishihara, T. Kubo, Y. Watanabe, M. Gai, R. France III, K. Hahn, Z. Zhao, T. Nakamura, T. Teranishi, Y. Futami, K. Furutaka, and T. Delbar. "Coulomb Dissociation of $^8\mathrm{B}$ and the $^7\mathrm{Be}(\mathrm{p},\gamma)^8\mathrm{B}$ Reaction at Low Energies". *Physical Review Letters*, Vol. 73, pp. 2680–2683, 1994.

[Muk95] A. Mukhamedzhanov, R. Tribble, and N. Timofeyuk. "Possibility to determine the astrophysical S factor for the $^7\mathrm{Be}(\mathrm{p},\gamma)^8\mathrm{B}$ radiative capture from analysis of the $^7\mathrm{Be}(^3\mathrm{He,d})^8\mathrm{B}$ reaction". *Physical Review C*, Vol. 51, pp. 3472–3478, 1995.

[Neg96] F. Negoita, C. Borcea, F. Carstoiu, M. Lewitowicz, M. Saint-Laurent, R. Anne, D. Bazin, J. Corre, P. Roussel-Chomaz, V. Borrel, D. Guillemaud-Mueller, H. Keller, A. Mueller, F. Pougheon, O. Sorlin, S. Lukyanov, Y. Penionzhkevich, A. Fomichev, N. Skobolev, O. Tarasov, Z. Dlouhy, and A. Kordyasz. "$^8\mathrm{B}$ proton halo via reaction and breakup cross section measurements". *Physical Review C*, Vol. 54, pp. 1787–1797, 1996.

[Nun97] F. Nunes, R. Crespo, and I. Thomson. "Uncertainties in the ground state structure of $^8\mathrm{B}$ and implications for the $\mathrm{S_{17}}$ astrophysical S-factor". *Nuclear Physics A*, Vol. 615, pp. 69–81, 1997.

[Nun98] F. Nunes and I. Thompson. "Nuclear interference effects in $^8\mathrm{B}$ sub-Coulomb breakup". *Physical Review C*, Vol. 57, pp. R2818–R2820, 1998.

[Ols83] D. Olson, B. Berman, D. Greiner, H. Heckman, P. Lindstrom, and H. Crawford. "Factorization of fragment-production cross sections in relativistic heavy-ion collisions". *Physical Review C*, Vol. 28, pp. 1602–1613, 1983.

[Par66] P. Parker. "$^7\mathrm{Be}(\mathrm{p},\gamma)^8\mathrm{B}$ Reaction". *Physical Review*, Vol. 150, pp. 851–856, 1966.

[Rol88] C. Rolfs and W. Rodney. *Cauldrons in the Cosmos.* The University of Chicago Press, Chicago and London, 1988.

[Sac90] Sackmann, Boothroyd, and Fowle. *The Astrophysical Journal*, Vol. 360, p. 727, 1990.

[Sam92] M. Samek. *APE – Analysis in PAW Environment.* CERN Computer Newsletter **208**, p.14, 1992.

[San95] J. Santiard. "Private communication". 1995.

[Sar91] A. Sartorius. *Aufbau und Test einer Vieldrahtproportionalkammer zum Teilchennachweis am Kaonenspektrometer.* Master's thesis, Technische Hochschule Darmstadt (D), 1991.

[Sch68] L. Schiff. *Quantum Mechanics.* McGraw Hill, New York, 3rd Ed., 1968.

[Sch96] J. Schwarzenberg, J. Kolata, D. Peterson, P. Santi, M. Belbot, and J. Hinnefeld. "Sub-Coulomb dissociation of ^{8}B". *Physical Review C*, Vol. 53, pp. 2598–2601, 1996.

[Sen93] P. Senger, W. Ahner, P. Baltes, P. Beckerle, C. Bormann, D. Brill, M. Cieślak, E. Grosse, W. Henning, P. Koczoń, B. Kohlmeyer, W. Konrad, D. Miśkowiec, C. Müntz, H. Oeschler, H. Pöppl, W. Prokopowicz, F. Pühlhofer, S. Sartorius, R. Schicker, B. Schlei, E. Schwab, Y. Shin, J. Speer, J. Stein, K. Stiebing, R. Stock, H. Ströbele, C. Sturm, K. Völkel, A. Wagner, and W. Waluś. "The Kaon Spectrometer at SIS (GSI)". *Nuclear Instruments and Methods in Physics Research A*, Vol. 327, pp. 393–411, 1993.

[Shy96] R. Shyam, I. Thompson, and A. Dutt-Mazumder. "Astrophysical S-factor of the ^{7}Be(p, γ)^{8}B reaction from Coulomb dissociation of ^{8}B". *Nuclear Physics B*, Vol. 371, pp. 1–6, 1996.

[Shy97] R. Shyam and I. Thomson. "E2 component in subcoulomb breakup of ^{8}B". *Physics Letters B*, Vol. 415, pp. 315–320, 1997.

[Shy99] R. Shyam and I. Thomson. "Coulomb and nuclear breakup of ^{8}B". e-Print Archive: nucl-th/9808069, 1999.

[Sie90] R. Sienkiewicz, J. Bahcall, and B. Paczynski. *The Astrophysical Journal*, Vol. 349, 1990.

[Sme99] M. Smedberg, T. Baumann, T. Aumann, L. Axelsson, U. Bergmann, M. Borge, D. Cortina-Gil, L. Fraile, H. Geissel, L. Grigorenko, M. Hellström, M. Ivanov, N. Iwasa, R. Janik, B. Jonson, H. Lenske, K. Markenroth, G. Münzenberg, T. Nilsson, A. Richter, K. Riisager, C. Scheidenberger, G. Schrieder, W. Schwab, H. Simon, B. Sitar, P. Strmen, K. Sümmerer, M. Winkler, and M. Zhukov. "New results on the halo structure of ^{8}B". *Physics Letters B*, Vol. 452, pp. 1–7, 1999.

[Smi99] A. Smirnov. "On Vacuum Oscillations Solution of the Solar Neutrino Problem". *Nuclear Physics B (Proc. Suppl.)*, Vol. 70, pp. 324–328, 1999.

[Str96] F. Strieder, L. Gialanella, U. Greife, C. Rolfs, S. Schmidt, W. Schulte, H. Trautvetter, D. Zahnow, F. Terrasi, L. Campajola, A. D'Onofrio, V. Roca, M. Romano, and M. Romoli. "The d(^{7}Li, p)^{8}Li cross section near $E_{cm} = 0.61$ MeV". *Zeitschrift für Physik A*, Vol. 355, pp. 209–218, 1996.

[Str98] F. Strieder, F. Schümann, L. Gialanella, D. Greife, U. Rogalla, C. Rolfs, H. Trautvetter, Z. Fülöp, G. Gyürky, E. Somorjai, R. Kavanagh, L. Campajola, A. D'Onofrio, A. Ordine, V. Roca, M. Romano, F. Terrasi, C. Arpesella, A. D'Alessandro, C. Gustavino, M. Junker, O. Straniero, P. Corvisiero, M. Dessalvi, P. Prati, S. Zavatarelli, C. Broggini, G. Gervino, A. Fubini, E. Bellotti, R. Bonetti, and A. Guglielmetti. "Loss of ^{8}Li recoil nuclei in ^{7}Li(d, p)^{8}Li and implications on the ^{7}Be(p, γ)^{8}B cross section near $E_{cm} = 0.61$ MeV". *European Physical Journal A*, Vol. 3, pp. 1–3, 1998.

[Sum94] K. Sümmerer *et al.* "Coulomb dissociation of ^{8}B into ^{7}Be + p". Proposal submitted to the GSI-EA, 05-Dec-1994.

[Sum98] K. Sümmerer *et al.* "Astrophysical Reaction Rates Studied by Coulomb Dissociation of Radioactive Beams". Proposal submitted to the GSI-EA, 05-Dec-1998.

[Sur95] G. Surówka. "C.A.E.N V550 and V551 Control Program". GSI draft, 1995.

[Sur98] G. Surowka. "A Simple Study of Deconvolution with Monte Carlo events". DRAFT, 1998.

[Tot96] Y. Totsuka. "Kamiokande and Super-Kamiokande". *Nuclear Physics B (Proc. Suppl.)*, Vol. 48, pp. 547–556, 1996.

[Tur88] S. Turck-Chièze *et al.* *The Astrophysical Journal*, Vol. 335, p. 415, 1988.

[Tur93] S. Turck-Chièze and I. Lopes. *The Astrophysical Journal*, Vol. 408, p. 367, 1993.

[Tur96] S. Turck-Chièze. "The Sun as a laboratory: a classical or a non classical Sun?". *Nuclear Physics B (Proc. Suppl.)*, Vol. 48, pp. 350–356, 1996.

[Typ97] S. Typel, H. Wolter, and G. Baur. "Higher-order effects in the Coulomb dissociation of ^{8}B into $^{7}\mathrm{Be} + \mathrm{p}$". *Nuclear Physics A*, Vol. 613, pp. 147–164, 1997.

[Uhl98] F. Uhlig. *Zwei Vieldrahtproportionalkammern zur Bestimmung des totalen Wirkungsquerschnittes der Reaktion $^{8}B(\gamma,p)^{7}Be$.* Master's thesis, Technische Universität Darmstadt (D), 1998.

[Vau70] F. Vaughn, R. Chalmers, D. Kohler, and L. Chase Jr. "Cross Sections for the $^{7}\mathrm{Be}(\mathrm{p},\gamma)^{8}\mathrm{B}$ Reaction". *Physical Review C*, Vol. 2, pp. 1657–1665, 1970.

[Wei98] L. Weissman, C. Broude, G. Goldring, R. Hadar, M. Hass, F. Schwamm, and T. Shannan. "A new measurement of the $^{7}\mathrm{Li}(\mathrm{d},\mathrm{p})^{8}\mathrm{Li}$ cross section and consequences for $^{7}\mathrm{Be}(\mathrm{p},\gamma)^{8}\mathrm{Be}$". *Nuclear Physics A*, Vol. 630, pp. 678–688, 1998.

[Wie77] C. Wiezorek, H. Kräwinkel, R. Santo, and L. Wallek. "Study of the $^{7}\mathrm{Be}(\mathrm{p},\gamma)$-Reaction". *Zeitschrift für Physik A*, Vol. 282, pp. 121–123, 1977.

[Wil81] R. Williams and S. Koonin. "Direct capture cross sections at low energy". *Physical Review C*, Vol. 23, pp. 2773–2774, 1981.

[Win79] A. Winther and K. Alder. "Relativistic Coulomb Excitation". *Nuclear Physics A*, Vol. 319, pp. 518–532, 1979.

[Wol78] L. Wolfenstein. "Neutrino oscillations in matter". *Physical Review D*, Vol. 17, pp. 2369–2374, 1978.

[Xu94] H. Xu, C. Gagliardi, R. Tribble, A. Mukhamedzhanov, and N. Tomofeyuk. "Overall Normalization of the Astrophysical S Factor and the Nuclear Vertex Constant for $^{7}\mathrm{Be}(\mathrm{p},\gamma)^{8}\mathrm{B}$ Reactions". *Physical Review Letters*, Vol. 73, pp. 2027–2030, 1994.